Summer 8-2022

Quantification of Wave Attentuation of a Marsh Sill Living Shoreline and Application of Numerical Modeling for Design Optimization and Adaptation

Maura K. Boswell
Old Dominion University, maura.boswell@gmail.com

QUANTIFICATION OF WAVE ATTENTUATION OF A MARSH SILL LIVING SHORELINE AND APPLICATION OF NUMERICAL MODELING FOR DESIGN OPTIMIZATION AND ADAPTATION

by

Maura K. Boswell

B.S. July 2002, Florida Institute of Technology
M.S. May 2004, University of Florida

A Dissertation Submitted to the Faculty of
Old Dominion University in Partial Fulfillment of the
Requirements for the Degree of

DOCTOR OF PHILOSOPHY

CIVIL & ENVIRONMENTAL ENGINEERING

OLD DOMINION UNIVERSITY
August 2022

Approved by:

Gangfeng Ma (Director)

Thomas Allen (Member)

Donna M. Bilkovic (Member)

Mudje Erten-Unal (Member)

Bret Webb (Member)

ABSTRACT

QUANTIFICATION OF WAVE ATTENTUATION OF A MARSH SILL LIVING SHORELINE AND APPLICATION OF NUMERICAL MODELING FOR DESIGN OPTIMIZATION AND ADAPTATION

Maura K. Boswell
Old Dominion University, 2022
Director: Gangfeng Ma

Living shorelines integrate structural and natural features to stabilize the shoreline, through reduction of erosion from the wave climate, while keeping the connectivity between land and aquatic ecosystems. With increasing sea levels, living shorelines have the potential to adapt to changing conditions when compared to armored shorelines due to maintaining a level of interconnectivity between land and water. However, to reduce the ecological tradeoffs associated with any type of shoreline erosion protection project that alters the natural state, the design should seek to minimize structural components to those necessary to provide the protection needed for upland habitat to survive erosive forces for the project design life. For this study, field data were collected at the Captain Sinclair Recreational Area marsh sill living shoreline project in southeastern Virginia. Wave data were collected along two profiles, one across a sill structure and one across a gap between two sills to analyze the wave attenuation properties of the structure and vegetation components of the living shoreline project. Following quantification of the wave attenuation services of this project, the data were used to calibrate a Non-hydrostatic WAVE model, NHWAVE, for additional numerical analysis regarding structure crest elevation and sea level rise. The study showed that the structure profile of the marsh sill design was quite effective at attenuating wave energy across the spectrum, with some frequencies better attenuated than other frequencies. The results of the numerical portion of the study revealed that NHWAVE was able to calibrate well with the landward and marsh gauges from the field study and show that the

vegetation portion of the living shoreline design has a greater impact on wave energy attenuation than the crest height of the structure when the latter is reduced in elevation. The numerical modeling assessment also showed the capacity of the living shoreline to adapt to potential sea level rise scenarios for the next 30 years and still provide considerable wave attenuation services.

This thesis is dedicated to the village it took to assist me on this journey, without whose love and support it would not have been possible. To my husband Patrick who supported me financially, emotionally, and physically as a field assistant to collect the data for this research. To my parents and my friend Mae who watched my son so that I could do field work and attend conferences. To my sister and countless friends who offered support and encouragement along the way. Most especially this is dedicated to my children, Duncan and Isla, who were born into this adventure.

ACKNOWLEDGMENTS

I would like to thank my committee members for their patience and for providing feedback to improve my research and to Virginia Sea Grant for providing funding in support of this project. I owe a special debt of gratitude to my advisors, Dr. Gangfeng Ma and Dr. Bret Webb, without whose mentoring, advice, and troubleshooting assistance this dissertation and research would not have been accomplished.

NOMENCLATURE

b_v	Stem size
C_D	Drag coefficient
D_{50}	Nominal diameter
g	Gravity
h	Water depth
H	Wave height
H_s	Significant wave height
κ	von Karman constant
KC	Keulegan-Carpenter number
η	Water surface elevation
n	Porosity
N	Number of stems per unit area
$NAVD$	North American Vertical Datum
p	Pressure
T	Wave period
T_p	Peak wave period
v	Viscosity
ω	Vertical velocity

TABLE OF CONTENTS

Page

LIST OF TABLES

Table Page

LIST OF FIGURES

Figure Page

Figure Page

Figure Page

CHAPTER

1 INTRODUCTION

Climate change is increasing the frequency and intensity of storms (IPCC, 2021) which is adversely affecting coastal shorelines and exacerbating shoreline erosion (Klotzbach et al., 2018). As increased wave environments create conditions of erosion along marsh shorelines, coastal wetlands have been shown to reduce upland property damage from storm events (Costanza et al., 2008; Sun & Carson, 2020) and provide key ecosystem services (Barbier et al., 2011; Blair et al., 2018). Encouraging shoreline erosion protection measures that incorporate maintenance of ecological function of the shoreline with erosion control designs is imperative to preserving the natural environment in the face of climate change (Bilkovic et al., 2016) and can provide a more sustainable solution to coastal erosion in suitable locations (Temmerman et al., 2013). While terminology for what constitutes a living shoreline is not always clear (Smith et al., 2020), for this study the term includes the hybrid features including a structural component (rock sill) and vegetation (marsh planting) in the design.

Living shorelines integrate structural and natural features to stabilize the shoreline, through reduction of erosion from the wave climate, while keeping the connectivity between land and aquatic ecosystems. With increasing sea levels, living shorelines have the potential to adapt to changing conditions when compared to armored shorelines due to maintaining a level of interconnectivity between land and water. However, to reduce the ecological tradeoffs associated with any type of shoreline erosion protection project that alters the natural state, the design should seek to minimize structural components to those necessary to provide the protection needed for upland habitat to survive erosive forces for the project design life. While living shorelines have been designed for decades in one capacity or another, monitoring and

quantification of wave energy attenuation services is sparse. Data quantifying the effectiveness of living shoreline designs is necessary to improve upon the design guidance.

The ability of marsh vegetation to adapt to changes in sea level, with the presence of adequate room for landward migration, offers an adaptive component for a living shoreline system during the life of the project that is not present with a fully armored shoreline. Incorporating the wave energy attenuation benefits of the marsh vegetation into a living shoreline design allows for opportunity to minimize the structure portion of the design by sharing the attenuation services across the system and not merely the structural component. Additionally, living shoreline designs have the potential capacity to adapt to sea level rise and continue to offer wave attenuation services from vegetation components even as the attenuation effectiveness of the crest height decreases.

1.1 Research Objectives

The following research objectives will be explored and answered in this study:

1. How quantitatively effective is a marsh sill living shoreline at attenuating wave energy?

2. How does reducing the crest height to decrease the structure footprint and increase land and water connectivity affect the overall wave attenuation properties of the living shoreline system?

3. How do the overall attenuation properties of a living shoreline change as sea level rise increases and what is the potential adaptation capacity for the design life of the project?

1.2 Summary of Research Design

This study examines the efficacy of the Captain Sinclair Recreational Area marsh-sill living shoreline project in the Severn River sub-estuary of Virginia. The project was constructed in 2016 and consists of four rock sills, sand fill, and vegetation adjacent to an eroding marsh.

Gaps between the sills allow for land-water connectivity and the overall design is representative of typical projects throughout the lower Chesapeake Bay region. Field data were collected at the project along two profiles, one across a sill structure and one across a gap between two sills. The field data are examined to determine the wave energy attenuation benefits of the structure and the marsh at varying waters levels. These data are used to calibrate and validate the three-dimensional Non-Hydrostatic WAVE model, NHWAVE, to investigate wave attenuation services of the living shoreline system, both structural and vegetation components, areas for optimizing structure crest height design to decrease ecological tradeoffs, and potential for the design to adapt to sea level rise.

1.3 Key Terms and Definitions

Coastal armoring – a manmade structure designed to either prevent erosion of the upland property or protect eligible structures from the effects of coastal wave and current action.

Living shoreline – a protected and stabilized shoreline that is made of natural materials such as plants, sand, or rock.

Natural and Nature-Based Features (NNBF) – landscape features that are used to provide engineering functions relevant to flood risk management, while producing additional economic, environmental, and/or social benefits

Numerical models – mathematical models that use a numerical time-stepping procedure to obtain the models behavior over time

Sea level rise – an increase in the ocean's surface height relative to the land in a particular location

Sill – a small offshore, shore-parallel structure, usually made of rock

Wave attenuation – a reduction in the energy of a traveling wave as it propagates through a medium

1.4 Dissertation Organization

This dissertation is comprised of five chapters: Chapter 1 is an introduction; Chapter 2 is the literature background on living shorelines and design guidance; Chapter 3 presents the data collection method and results of the field assessment; Chapter 4 presents the calibration and validation of the numerical modeling, as well as the results of the modeled alternatives; and Chapter 5 is a discussion and conclusions chapter. Appendices with data post-processing codes and numerical model inputs are also included. A summary of each chapter is as follows:

Chapter 1 introduces the research and design of the data collection and analyses as well as the questions intended to be answered.

Chapter 2 provides background on the subject of natural and nature-based features (NNBF), living shoreline design, existing available field studies of living shorelines, and numerical modeling studies related to these designs.

Chapter 3 details the field data collection at Captain Sinclair Recreational Area (Captain Sinclair) living shoreline project. The chapter includes the description of instrumentation used to collect data, site conditions, overall characteristics of the deployment, and analyses of the effectiveness of wave attenuation across the living shoreline project.

Chapter 4 describes the numerical model NHWAVE and the background for using numerical modeling to assess engineering design approaches. This chapter shows the calibration and validation of the model using data collected during the deployment at Captain Sinclair that is described in Chapter 3. The chapter also includes the alternatives analyses looking at the

interaction of the structure crest height with respect to wave attenuation and discusses these changes within the context of future sea level rise.

Chapter 5 is a discussion of the findings of this research, conclusions as to the contributions of these findings to the field of coastal science and engineering, and identification of additional research needed.

Appendix A includes the MATLAB codes used to process the raw data collected at Captain Sinclair and the analyses performed to determine the effectiveness of the living shoreline at attenuating wave energy.

Appendix B includes the input parameters for the numerical model calibration, validation, and alternatives analyses.

CHAPTER 2 BACKGROUND

Climate change is altering not just the landscape, but our approach to living with and adapting to the changing coastal environment. As the benefits of coastal wetland response to sea level rise and storm events continues to be understood, and quantified, these natural features are becoming a focus for restoration and creation as part of adaptation and risk reduction planning (Narayan et al., 2017).

Natural and Nature-based features (NNBF) are moving into the mainstream focus for shoreline erosion protection design in part due to increased regulatory practices and policies implicitly making them the preferred shoreline protection method. This shift has been noticeable in the recent changes by states, Virginia Living Shoreline Act (Wetlands Protection; Living Shorelines, 2020), Delaware Shoreline Stabilization SAA (Delaware Department of Natural Resources and Environmental Control, 2015) Maryland Living Shorelines Protection Act of 2008 (Living Shoreline Protection Act of 2008, 2008), and the proposed federal government Living Shorelines Act of 2019 (Living Shorelines Act of 2019, 2019) to make these designs easier to implement from a regulatory aspect. Nevertheless, the quantified effectiveness of these types of design is lacking, thereby inhibiting application (Reguero et al., 2018).

Living shorelines have been designed for decades, with associated guidance documents developed over the years, under the guise of shoreline erosion protection or habitat restoration, with more recent publications using the moniker living shorelines (Bridges et al., 2015; Broome et al., 1992; Currin et al., 2018; Hardaway Jr., C.S. et al., 2017; Walker et al., 2011). While some of the earlier publications focused on either the restoration of habitat or shoreline erosion protection, more recent guidance focuses on the system as a whole and not merely one

measurement of success (Bridges et al., 2015; Miller et al., 2016). However, it is often still challenging to implement these type of shoreline erosion protection projects due to a lack of specific design guidance for these designs as compared to a hardened shoreline design, e.g. seawalls, revetments, etc. (Morris et al., 2020; Narayan et al., 2016). One reason for this shortage of design guidance is a paucity of study of existing living shoreline design projects (Smith et al., 2020). Monitoring of living shoreline projects once constructed is scarce, leading to a deficiency of data on the effectiveness and true success of these projects (Bouma et al., 2014; Morris et al., 2018; Narayan et al., 2016). This dearth of knowledge increases the difficulty in successfully siting and designing an appropriate living shoreline for specific project sites (Borsje et al., 2011). Increased study of existing projects and quantification of their benefits will help designers improve living shoreline design for better shoreline management practices and increase their use more broadly (Morris et al., 2018; Reguero et al., 2018).

Another reason for the paucity of design guidance is due to the multidisciplinary aspect of living shoreline design. Appropriately designing these types of projects incorporates the challenge of working with a diverse group of stakeholders, holding differing concerns as to the nature of project success, e.g. structural, ecological, societal, etc., with an increased understanding for the need to implement sustainable projects that incorporate a multitude of stakeholders (Nesshöver et al., 2017). While the initial need for a living shoreline project is existing erosion of a shoreline, the additional ecosystem services that can be provided through a living shoreline project, as opposed to an armored shoreline, need be no less important when considering shoreline erosion protection design (Isdell et al., 2021; Seddon et al., 2020). Any anthropogenic impact to the natural wetland environment will compromise the existing habitat; however, if shoreline erosion protection designs consider the health of the adjacent habitat, then

desired ecological functions can be better maintained (Bilkovic et al., 2016; Isdell et al., 2021). These types of projects bring professionals with varying backgrounds to the project design team to design and implement an appropriate project for the greatest opportunity of success (Nesshöver et al., 2017). The multidisciplinary facets of a natural or nature-based feature inspired shoreline erosion mitigation project will provide the best opportunity for success if the variety of partners, including coastal engineers, ecologists, biologists, coastal mangers, and site users, are all engaged early in the design process to provide the appropriate input to achieve the multifaceted definitions of success.

Although recent contributions to living shoreline design guidance have increased (Bridges et al., 2015; Hardaway Jr., C.S. et al., 2017; Miller et al., 2016) from a designer standpoint, the guidance for designing a living shoreline erosion protection project remains deficient when attempting to compare these systems to a hardened shoreline erosion protection system. This makes it difficult to demonstrate that these green-gray designs are a better choice for shoreline erosion protection (Morris et al., 2018; Narayan et al., 2016). Sufficient research demonstrating the effectiveness and the comparative success, or increased success, of a living shoreline erosion protection design as opposed to a traditional, hardened shoreline erosion protection structure is necessary to move these types of designs into the mainstream (Morris et al., 2018; Smith et al., 2020).

Living shorelines have the ability to adapt to changing water level conditions, such as sea level rise, with marsh habitats increasing in elevation as sediment is slowly deposited with increasing sea levels (Kirwan et al., 2016; Mitchell et al., 2017). Marsh vegetation has been shown to be effective at attenuating wave energy (Broome et al., 1992; Jadhav et al., 2013; Möller, 2006; Wu et al., 2016; Yang et al., 2012). Marsh edge erosion is largely impacted by

frequent wave energy as opposed to the extreme storm events (Leonardi et al., 2016) with a correlation between wave energy and marsh edge erosion shown by (Marani et al., 2011) and (Schwimmer, 2001). On an erosive marsh shoreline, effectively utilizing the structure portion of a living shoreline design to reduce erosive wave energy on the marsh fringe can permit marsh recovery (Walker et al., 2011) and encourage sufficient coastal protection of the system in the future (Morris et al., 2018). At the same time, structure overtopping of a living shoreline design can potentially mitigate some of the ecological tradeoffs that arise when a structure is placed along a marsh shoreline (Bilkovic et al., 2016). To increase success of both the erosion protection aspect of the structure for the marsh and the land-water connectivity for marsh ecosystem survival, a living shoreline designer must optimally design the crest elevation of the structure for these somewhat opposing but important aspects of overall design success. Several studies have shown that numerical models are successful in determining the extent to which wave energy is attenuated through vegetation under storm and future sea level rise scenarios (Nepf & Vivoni, 2000; Sheng et al., 2012). Numerical modeling has not been extensively used to quantify the interactions of structures and vegetation in the context of living shoreline design. A better understanding of the hydrodynamic processes occurring around these designs will enable practitioners to design and implement more successful projects.

With a lack of existing study and monitoring on previously constructed living shoreline projects, effective numerical modeling validation and calibration can lead to the ability to better assess future designs and optimize the overall living shoreline erosion mitigation project for effective success across the multi-disciplinary aspects of the design.

CHAPTER 3 FIELD DATA COLLECTION AND ANALYSIS

Living shoreline erosion protection designs have been implemented in some form or another for several decades to varying levels of success (Hardaway Jr., C.S. et al., 2017; Walker et al., 2011). While examples of these types of shoreline erosion protection projects can be found in a variety of locations in the United States, there is a dearth of knowledge regarding the quantified performance of these structures due to a lack of formal monitoring programs (Smith et al., 2020). Regrettably, this lack of monitoring misses an opportunity to learn from the various designs that have been implemented and potentially improve upon design guidance. To this end, this study seeks to quantify the effectiveness of a marsh sill living shoreline at the Captain Sinclair Recreational Area (Captain Sinclair) to provide more quantitative data regarding the effectiveness of a marsh sill living shoreline at attenuating wave energy. This assessment will focus on the entire living shoreline system, to include both the sill structure and vegetation components of the design, as often these types of projects are defined simply by the success of only one facet of the design (Smith et al., 2020), e.g., structure or vegetation. Traditionally, these types of shoreline erosion control projects are implemented in low- to moderate-energy wave environments and the Captain Sinclair living shoreline project is representative of typical living shoreline projects in the lower Chesapeake Bay. Therefore, inferences may be drawn from the results regarding similar living shoreline designs.

3.1 Study Area

Captain Sinclair is located in Gloucester County, Virginia on the Severn River (Figure 1). The Severn River is a meandering east-west 11-km river with its mouth at the Mobjack Bay and approximately 6 meters deep in the center of the channel offshore of the project site (NOAA,

2018). The living shoreline project is on the north side of the river facing south with a shallow, gradually sloping bottom and the fetch at the site is approximately 3.2 km from the southwest, 1.6 km from the south, and 2.4 km from the southeast as shown in Figure 2. The predominant wind direction is from the southwest and the mean tide range at the site is 0.7 m (Milligan et al., 2016). Water levels recorded during the deployment period were higher than predicted as shown in Figure 3, but within the range of water levels for the year as shown in Figure 4.

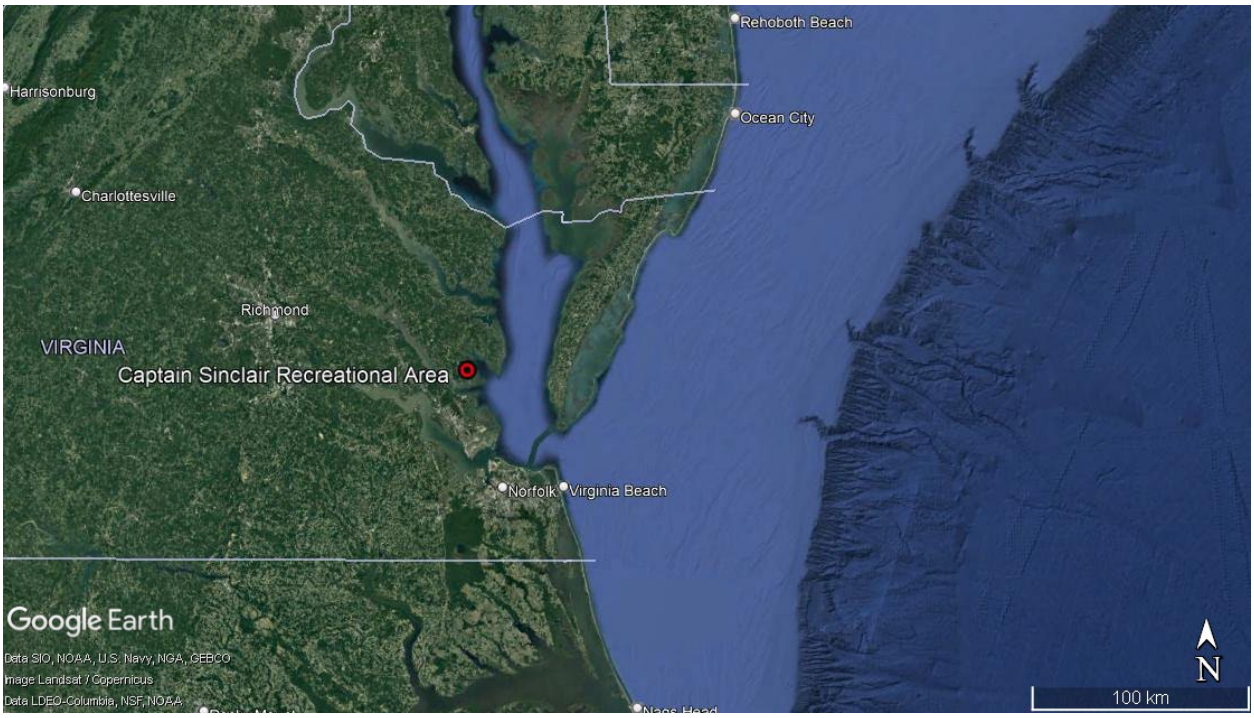

Figure 1: Captain Sinclair location map

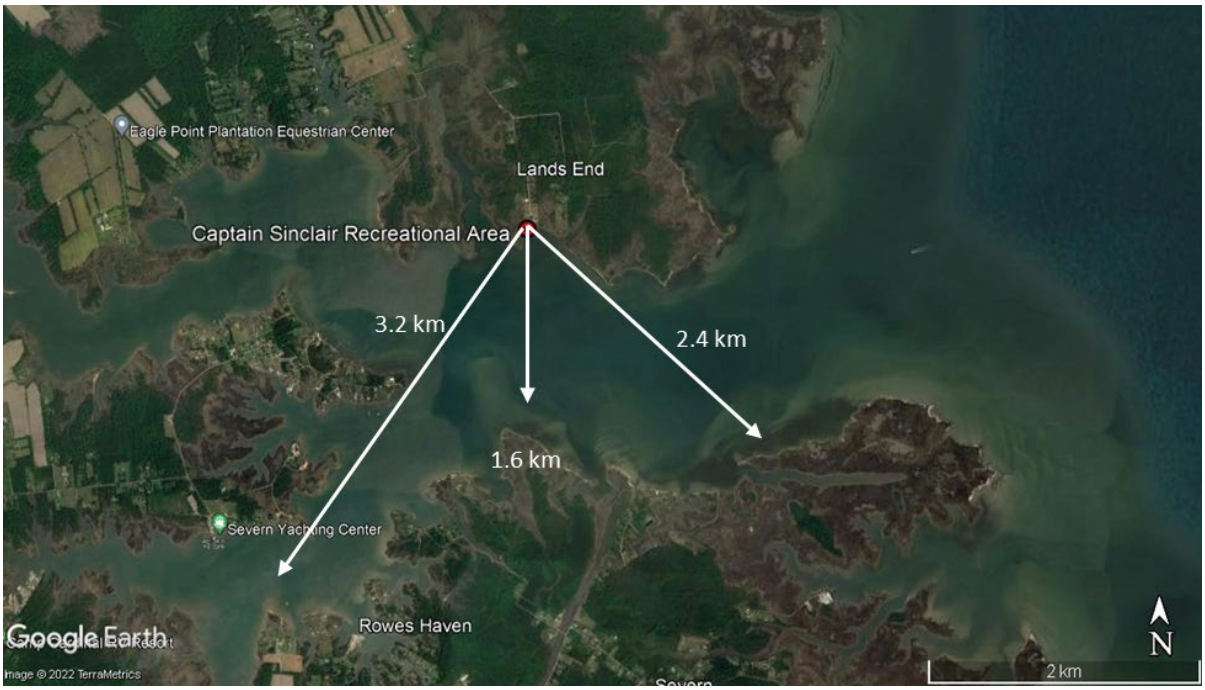

Figure 2: Captain Sinclair fetch distances

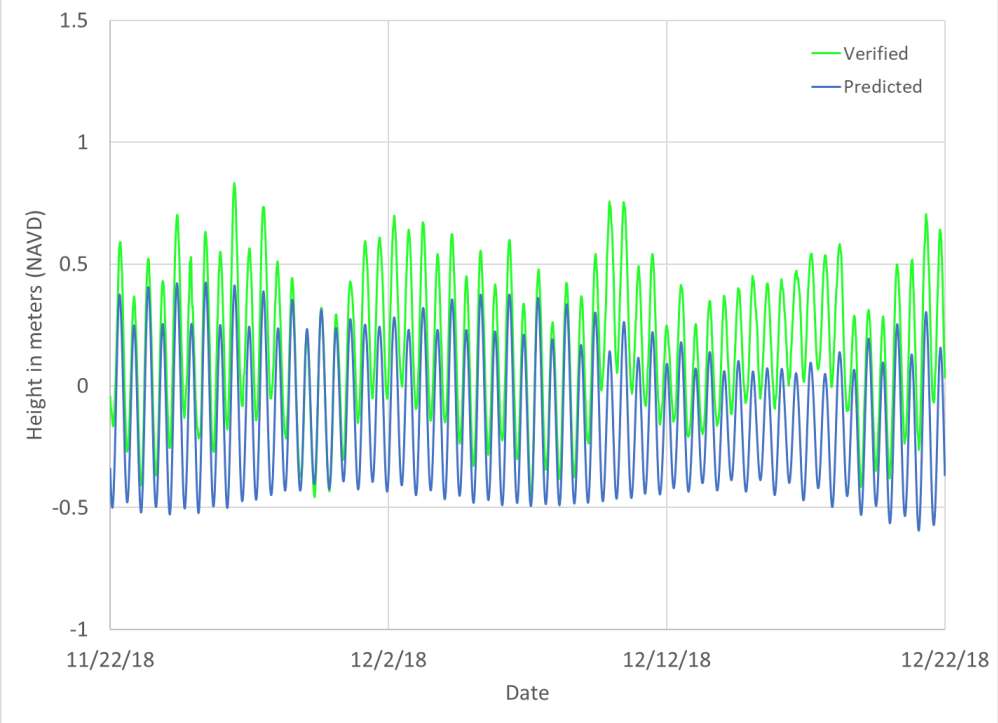

Figure 3: Predicted and verified water levels for the deployment period

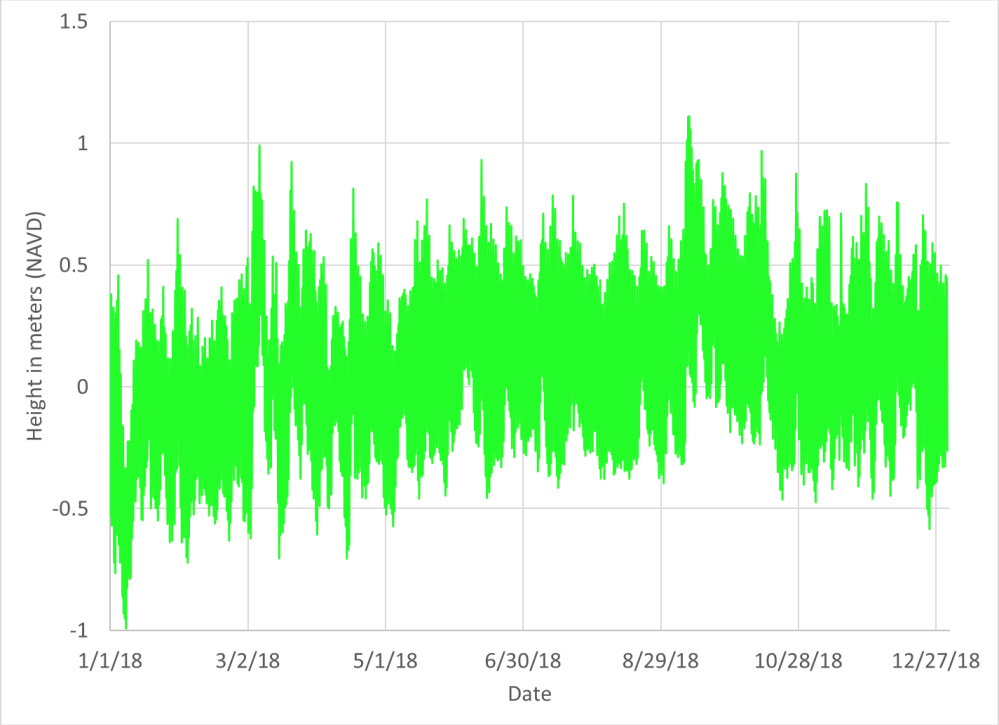

Figure 4: Verified water levels for 2018

As outlined in the Captain Sinclair's Shoreline Management Plan, this was an area of eroding shoreline, as can be seen in Figure 5. The marsh sill living shoreline was constructed in early 2016 to protect the marsh and upland and includes four rock sills separated by gaps, sand fill, and vegetation planting as shown in Figure 6 (Milligan et al., 2016). The focus area for this project is around the two western sills with dimensions of 23 meters and 32 meters in length, respectively, with 0.9-meter-wide crests at an elevation of 0.2 meters above mean high water, which was the top of the eroding peat scarp. The sills were constructed using VA Class II riprap armor stones (D_{50} = 0.5 m), backfilled with sand, and the low marsh was planted with *Spartina alterniflora* and the high marsh with *Spartina patens* as shown in Figure 7. Post-construction

photographs immediately following construction, prior to the vegetation planting season, are shown in Figure 8.

Figure 5: Pre-construction photos of the Captain Sinclair shoreline from April 2015 (Milligan et al., 2016)

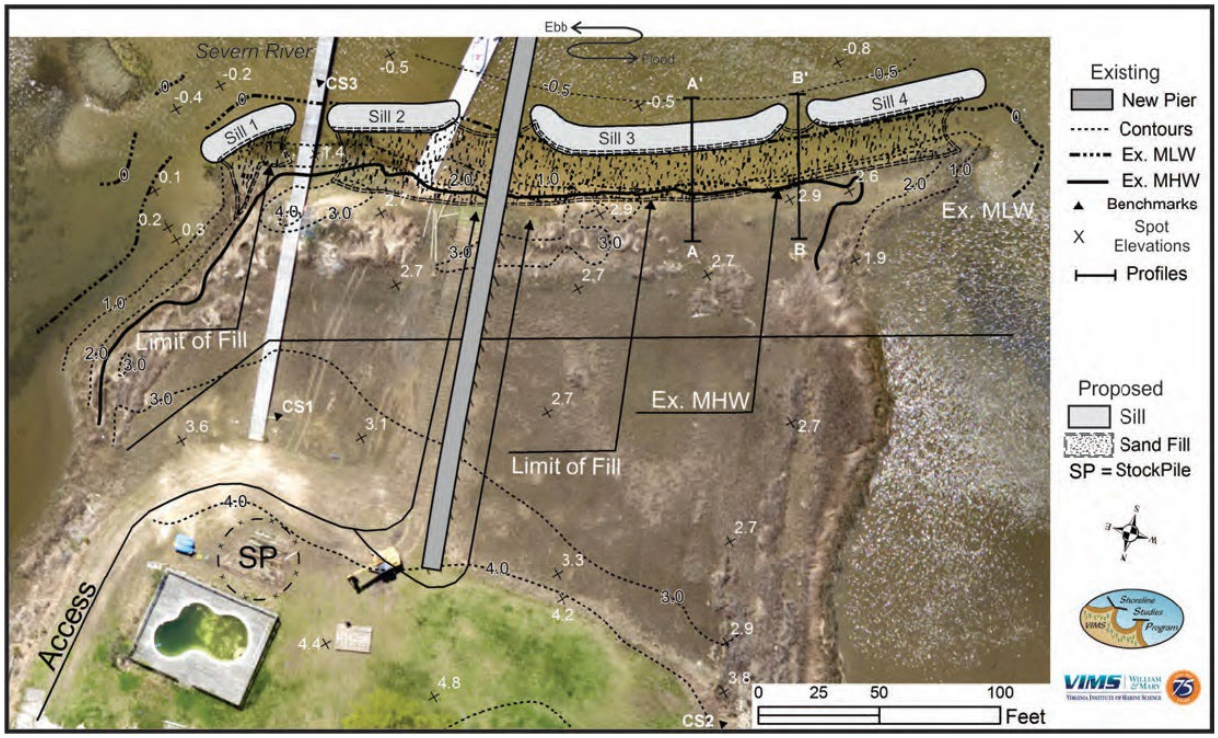

Figure 6: Living shoreline design site plan layout (Milligan et al., 2016)

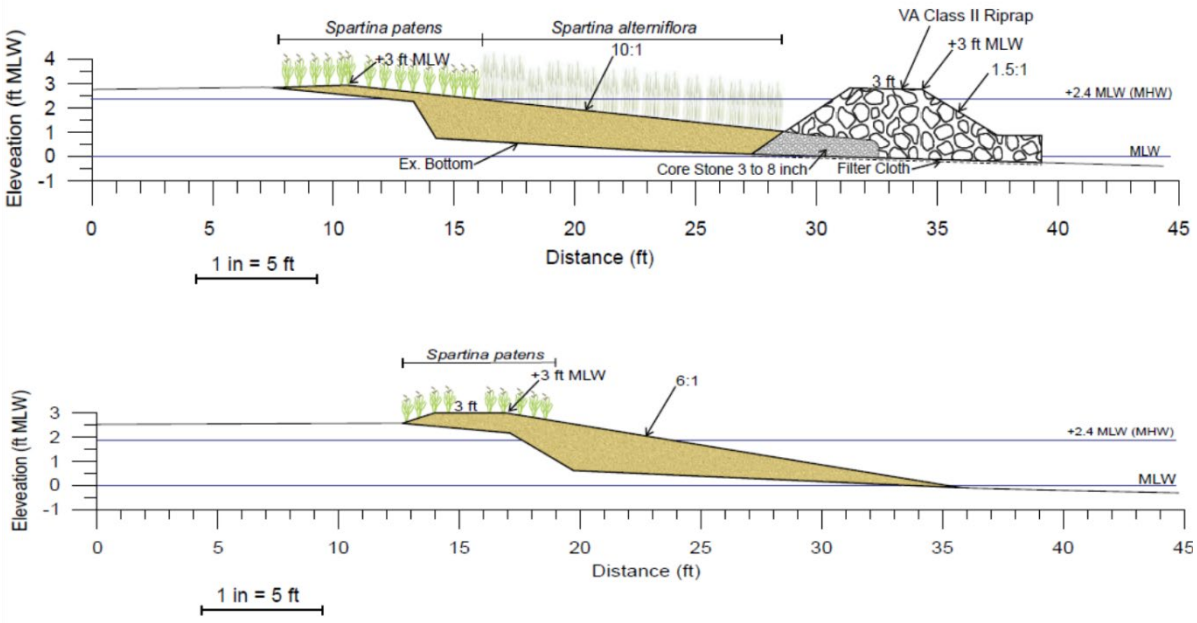

Figure 7: Project cross-sections (Milligan et al., 2016)

Figure 8: Post-construction photographs from February 2016 (Milligan et al., 2016)

Qualitatively, the project has been successful at mitigating the previous ongoing shoreline erosion, as shown in post-construction photographs from site visits conducted during and following the deployment for this study (Figure 9). While the photographs clearly show that the

project has been successful from an engineering perspective of decreasing erosion along the shoreline, it is necessary to quantify the results to better understand the changes to the wave environment due to the living shoreline project.

Figure 9: Photographs from deployment site visits; top October 2016, bottom left November 2018, bottom right June 2021

3.2 Data Collection

Sufficient field data are necessary to accurately depict the wave environment. A cost effective and relatively easy manner in which to collect these data are to deploy pressure transducers and subsequently convert the pressure readings into water surface readings and analyze these data for wave heights. For this study, RBR wave loggers (*solo*D wave and virtuoso; hereafter referred to as gauges) were employed to collect data at the project site and were analyzed for local wave characteristics. Gauges were set along two profiles at the site as shown in Figure 10. One profile crosses the structure and the second profile crosses through the gap between the two sill structures. The gauges were anchored parallel to the bottom on stainless steel plates. The gauges were located to capture wave energy changes due to the sill structure, the effects of the gap between structures on wave characteristics, and the impacts of vegetation on wave energy. The changes in spectral wave energy across the structure is used to assess wave attenuation by structures for different water levels, while the changes in spectral wave energy across the marsh are used to assess the wave attenuation features of the marsh vegetation.

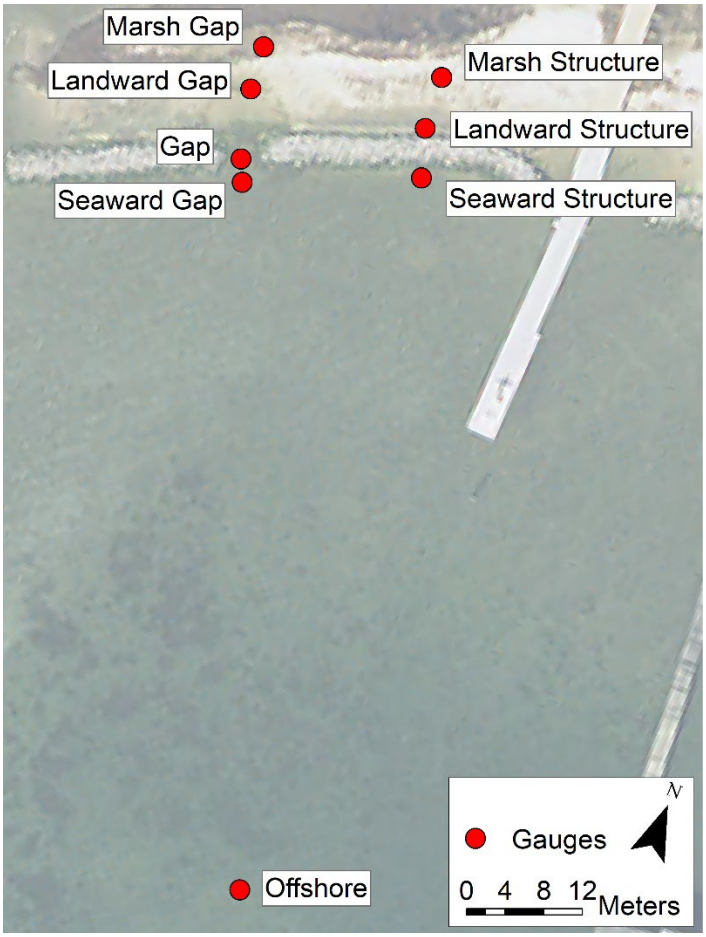

Figure 10: Gauge deployment locations

Topographic and bathymetric survey data were collected at the site at the time of gauge deployment. The landward gauge along the gap profile was placed at the same elevation as the landward gauge along the structure profile to capture data at the same elevation, which does not correlate to the same distance landward of the structure line. Due to additional erosion that occurs at the gap between structures, the landward gap gauge is farther landward of the structure gauge relative to the location of the sill structures.

Meteorological data for the deployment are obtained from the NOAA station at Yorktown USCG Training Center, VA (tidesandcurrents.noaa.gov; station 8637689) located 12

km southwest of the project site as shown in Figure 11. This was the closest publicly available, scientifically verified meteorological and water level gauge to the project site. The typical predominant wind direction, as shown in Figure 12, is from the southwest with a secondary easterly direction. During the deployment the predominant wind direction is from the south; however, there is a fairly wide spread of wind from southwest to northeast, as shown in Figure 13, with the strongest winds predominantly coming from the northeast. Water level data collected at this same station revealed that water levels during the deployment were mostly higher than originally predicted, as previously mentioned.

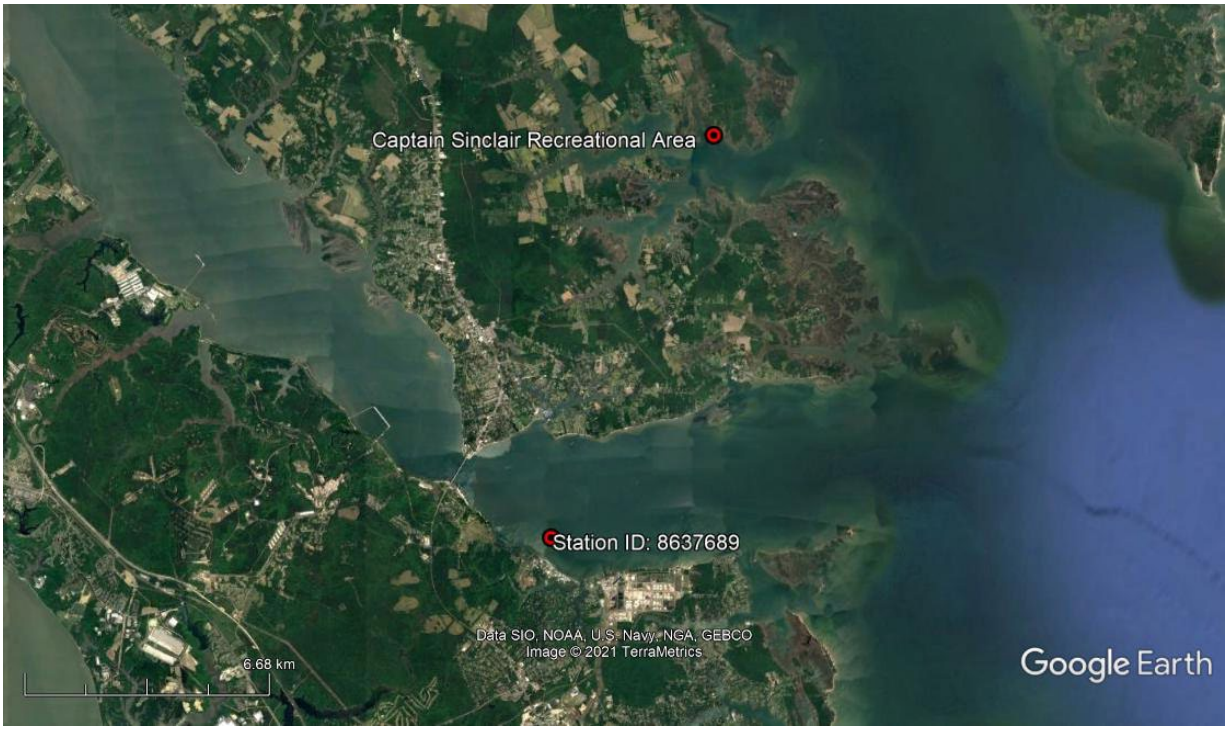

Figure 11: Location of meteorological station in relation to study site (image source: Google Earth)

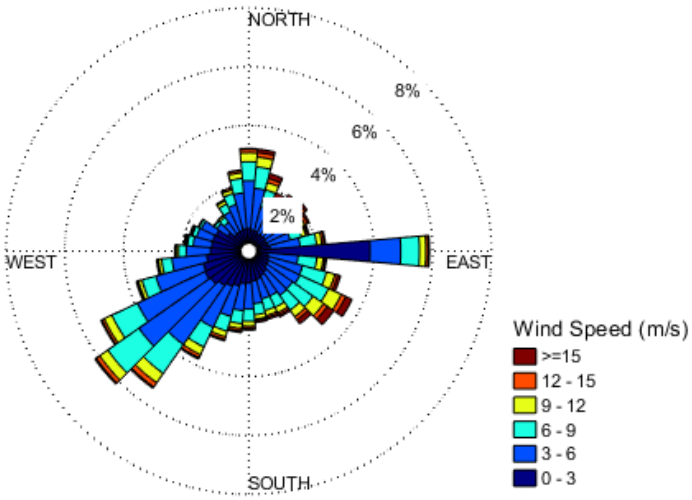

Figure 12: Wind characteristics from 2017-2021

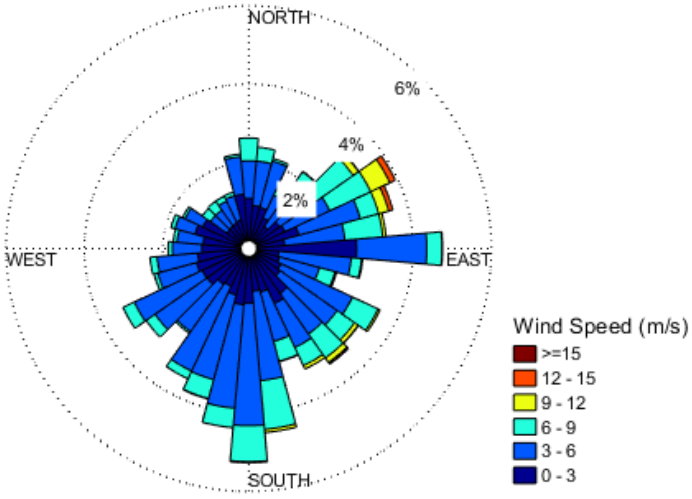

Figure 13: Wind characteristics during the deployment period

RBR *solo*D wave gauges can measure data at rates of 1, 2, 4, 8, or 16 Hz and the *virtuoso* gauges can measure data at rates of 1, 2, 3, 4, 5, 6, and 12 Hz set in continuous mode. The gauges were set to measure data at 8 Hz for the RBR *solo*D wave and 6 Hz for the *virtuoso*. The wave periods at this site are on the order of 1.5-4 seconds, so these sampling rates allow for a sufficient number of data points to be collected per wave period, while maximizing the battery life of the instrument.

The raw data points are used in analyses wherever possible; however, for some of the analyses it is necessary to resample the *virtuoso* gauge data collected at 6 Hz to an 8 Hz rate, as shown in Figure 14, to make comparisons between the offshore gauge and gauges located along the structure profile (*solo*D wave style) and the gap profile (*virtuoso* style).

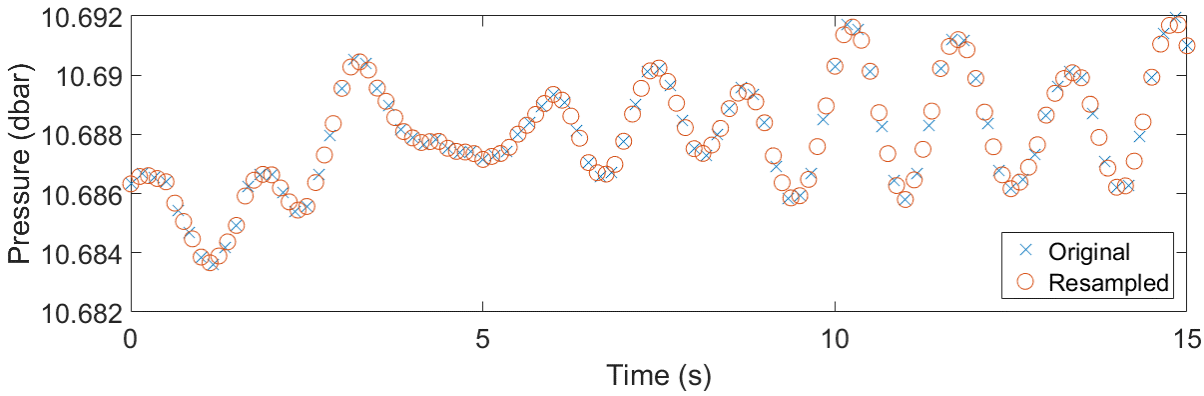

Figure 14: Original versus resampled raw data at the Gap gauge

The gauges were installed at the site on November 21, 2018 and the nearshore gauges were retrieved on December 27, 2018, while the offshore gauge was not able to be retrieved until February 17, 2019 due to inaccessibility caused by high water. The deployment period for

analysis for this study was set as November 22, 2018 to December 21, 2018 to analyze data from a full 30 day set of data collection.

3.3 Data Post-Processing

The data collected from the gauges are processed using a modified MATLAB code based on recent work by others (Temple et al., 2020) to convert the pressure readings into a sea surface. These calculations take into account the atmospheric pressure readings obtained from the nearby NOAA meteorological station. The pressure signal is separated into high and low components using a Butterworth filter, as shown in Figure 15, for further analyses to estimate standard wave properties from the high frequency wave component of the signal.

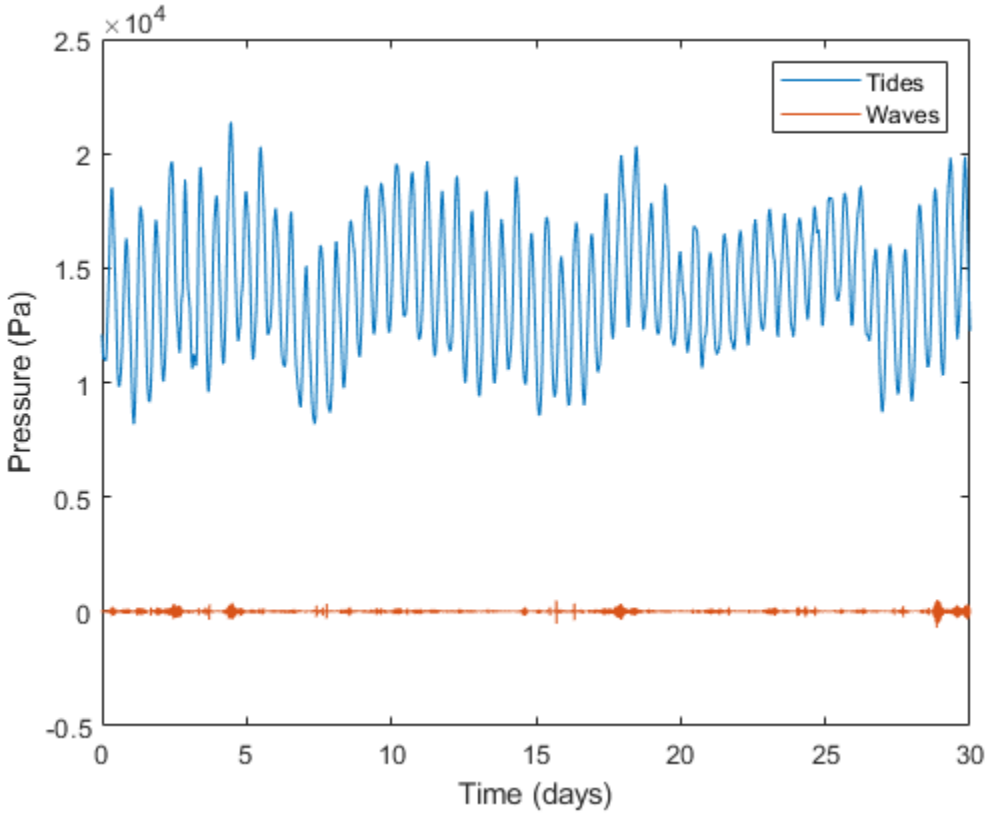

Figure 15: Separation of pressure components at Offshore gauge

The wave pressure component of the signal is converted into free surface elevations and individual wave heights using the zero-crossing method. For this study, waves below the threshold of 0.01 m are not considered to be within an acceptable range for sensitivity of analyses and not counted as recorded waves. Figure 16 shows the wave heights and periods calculated at the eight gauges for the study deployment period.

MATLAB codes for the data post-processing described in this section, and the specific analyses described in the next section, are included in Appendix A.

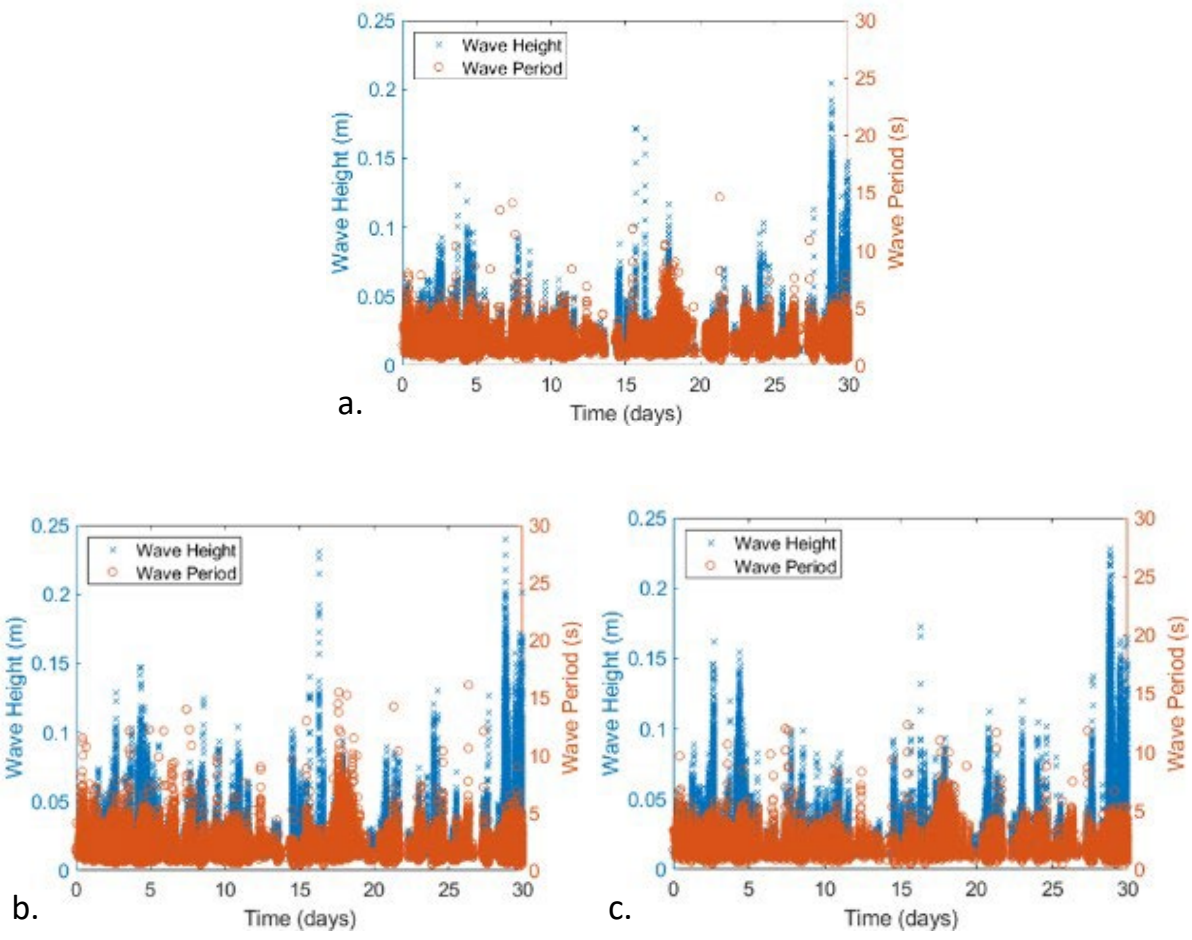

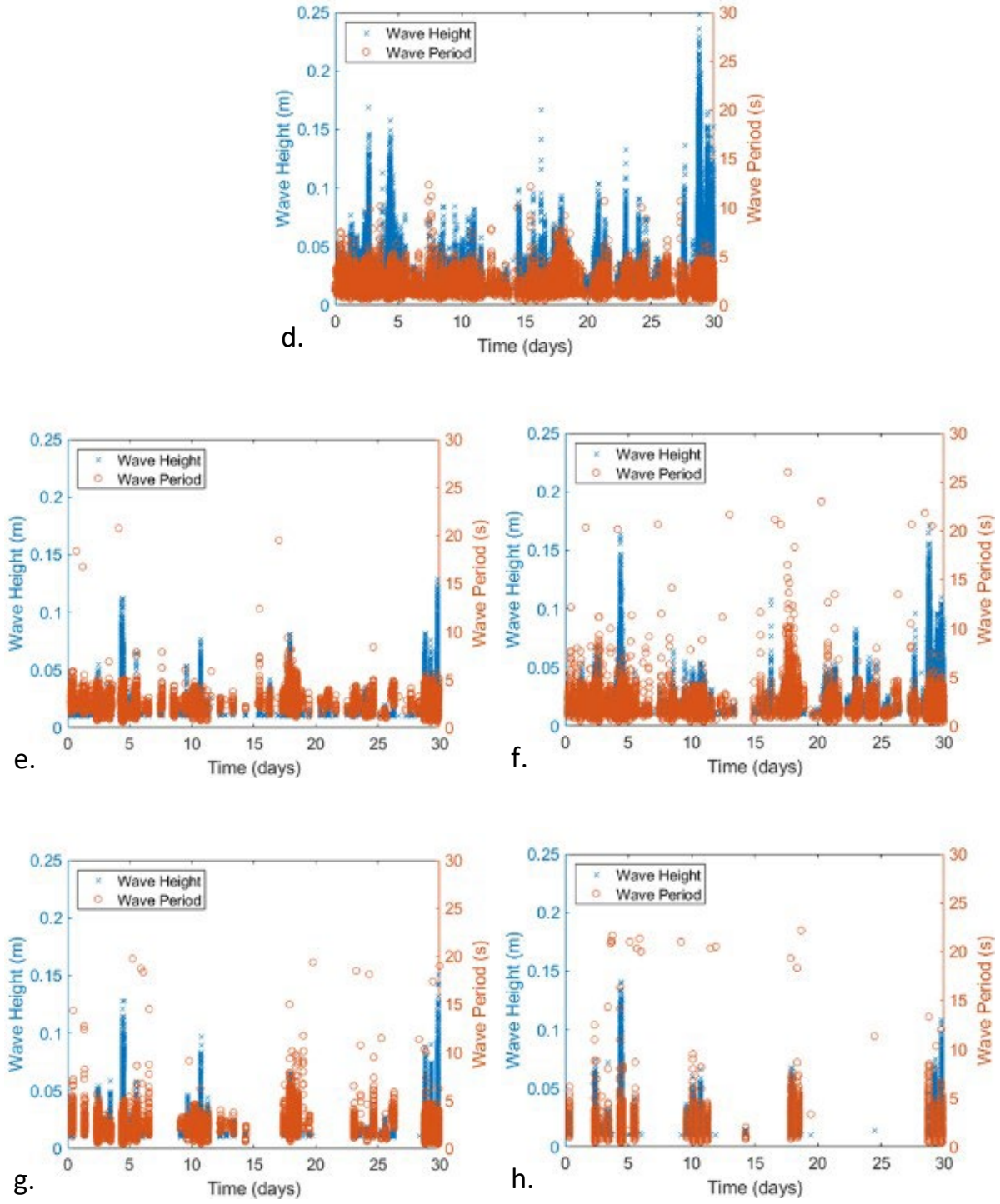

Figure 16: Deployment wave height and period at study gauges (a. offshore gauge; b. structure profile seaward gauge; c. gap profile seaward gauge; d. gap profile gap gauge; e. structure profile landward gauge; f. gap profile landward gauge; g. structure profile marsh gauge; h. gap profile marsh gauge)

3.4 Results

The results of the field data analyses are separated into two sections: overall deployment characteristics and analyses of specific threshold events. Observing a long deployment period allows data to be captured during both active and quiescent times at the project site. The characteristics of the overall deployment will first be discussed and then further analyses of a more specific subset of data will be discussed.

3.4.1 Overall Deployment Characteristics

A bird's-eye view analysis of the full deployment, with comparisons between the structure gauge profile and the gap gauge profile, is first introduced to give an overall assessment of the similarities and differences between the wave characteristics across the two profiles.

3.4.1.1 Wave Characteristics

Due to the quiescent nature of much of the deployment period the overall wave characteristics capture very small waves and periods, as shown in Table 1.

Table 1: Wave Characteristics for the Full Deployment Period

Gauge	Depth Range (m)	Hs (m)	Tp (s)	Depth Range (m)	Hs (m)	Tp (s)
Offshore	0.83-2.18	0.02	3.8			
	Structure Profile			Gap Profile		
Seaward	0.04-1.40	0.02	1.7	0.06-1.42	0.02	1.5
Gap				0-1.35	0.02	1.7
Landward	0-0.91	0.01	3.9	0-0.97	0.01	1.7
Marsh	0-0.43	<0.01	3.8	0-0.31	<0.01	3.7

While the overall deployment characteristics are small, the impact of the structure is apparent in the reduction of wave height and increase in peak wave period between the structure profile seaward and landward gauges. There is continued further reduction of wave height, albeit a small amount, between the structure profile landward and marsh gauges, which will be further analyzed in sections below.

The gap profile does show some reduction in wave heights from the seaward gauge to the landward gauge, likely owing to diffraction occurring as waves move through the gap between the two rock sills. There is a noticeable amount of wave height reduction between the gap profile landward gauge and marsh gauge. This can be attributed to both wave breaking and the influence of vegetation on wave attenuation provided by the marsh vegetation.

As shown in Figure 16, there are periods of the deployment where some of the gauges are dry and no waves are available for analysis. Due to these gaps in the data, it is not possible to conduct a wave-to-wave comparison across the data set. However, the overall difference between the structure profile and gap profile wave heights can be observed when comparing the significant wave heights between the seaward and landward gauges of each profile. From Figure 17 there is a marked difference between the wave heights at the landward gauges of each profile.

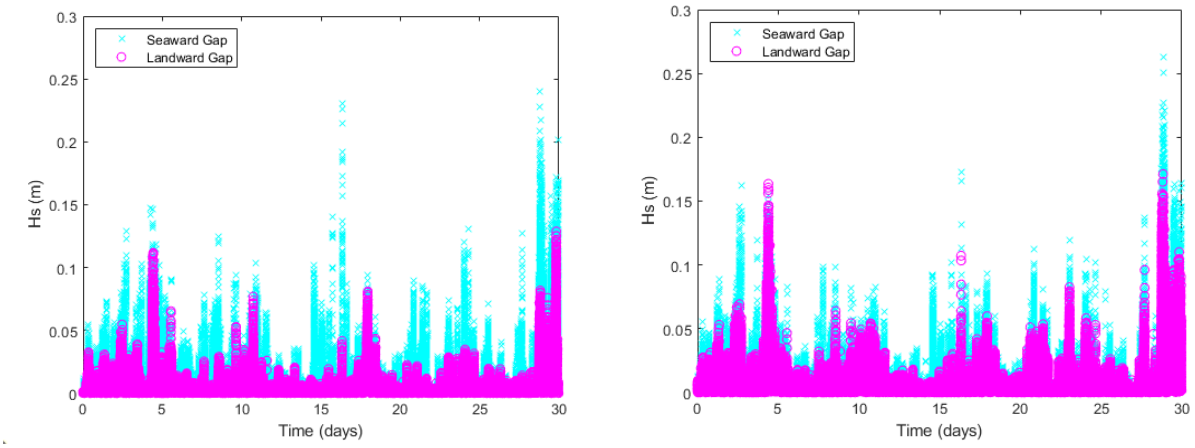

Figure 17: Significant wave heights at the seaward and landward gauges for the structure profile (left) and gap profile (right)

3.4.1.2 Spectral Analysis

An additional way to analyze the data set is to observe the full spectral density of the gauges for the entirety of the deployment and compare changes between the two profiles. These results reveal the significant influence of the structure on wave energy transmission. Figure 18 shows the side-by-side comparison of spectral wave energy across the structure profile and across the gap profile with the offshore gauge included in both figures to show the changes that occur at each profile from the offshore wave energy as it propagates across the two profiles.

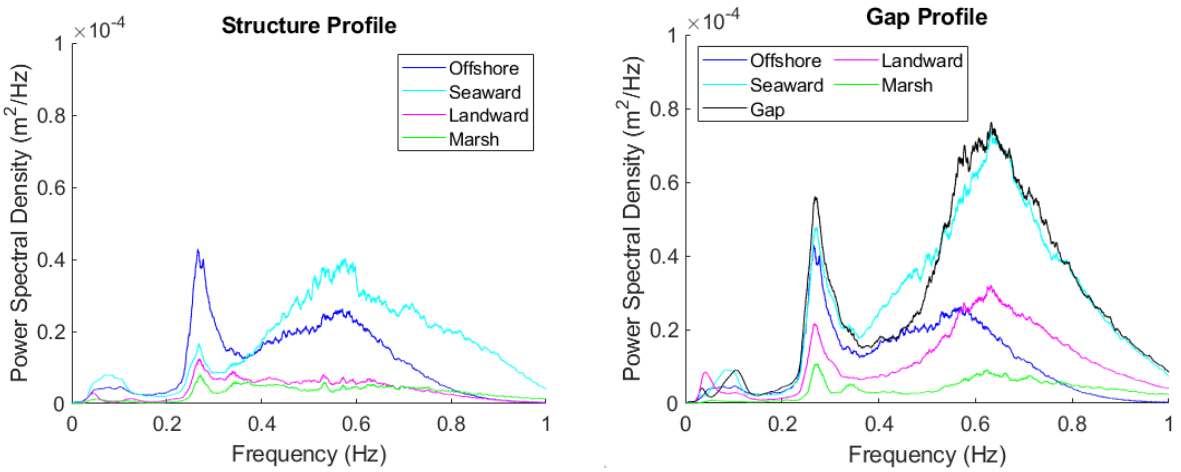

Figure 18: Power spectral density for structure and gap profiles for the full deployment period

The spectra show two frequency peaks with the narrow peak around 8 seconds likely due to boat wake waves. The wide peak spanning from 1-5 seconds is attributed to the locally generated sea waves and is the focus of assessment for this study. Shorter period waves become the more predominant peak in the gap profile and are indicative of diffraction occurring due to the sill structures. As evidenced in these figures, long wave periods are ineffective at transmitting into the marsh. There is very minimal energy in the 0 to 0.2 Hz range of the profiles so, for the next section of figures, the frequency scale will focus into the range from 0.2 to 1 Hz.

Comparisons Between Gauge Locations

The increased wave energy that occurs between the offshore gauge and the two seaward gauges and gap gauge is due to shoaling since shoaling increases wave heights to higher energy. The seaward structure gauge is located within one meter of the toe of the rock sill and the smaller increase in wave energy from the offshore gauge to the seaward structure gauge as compared to the seaward gap gauge is the result of wave reflection off the rock sill attenuating the incoming waves at the structure. To quantify the spectral change between two gauges, a standard percent

difference is calculated between the two gauges at each frequency data point. As shown in Figure 19, wave reflection from the sill structure attenuates wave energy from 9% to 73% depending on the frequency.

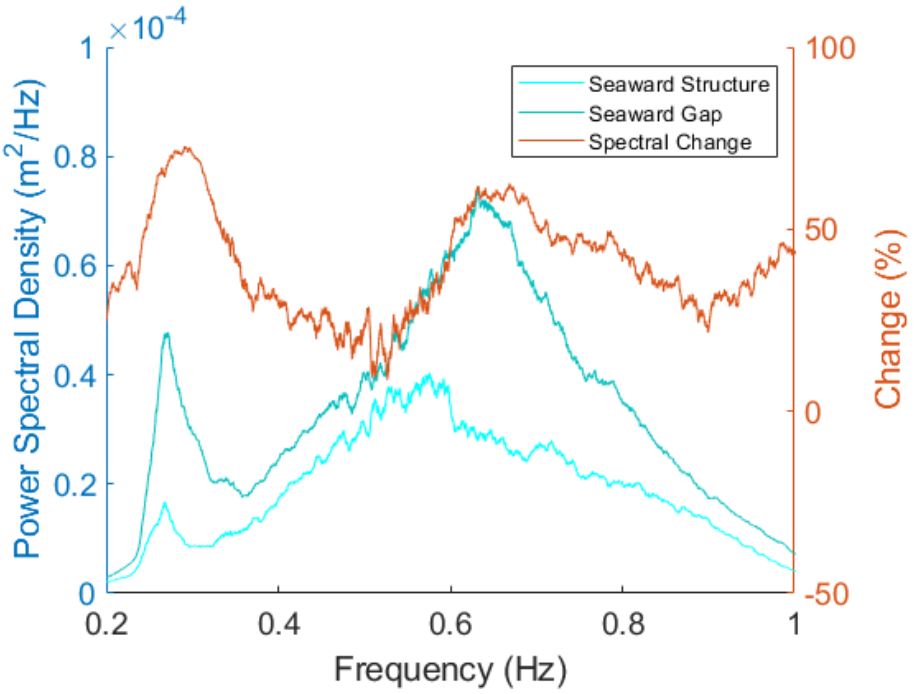

Figure 19: Power spectral density comparison of seaward gauges and attenuation due to reflection at the sill structure

Landward of the structure, the structure profile landward gauge has much lower wave energy than the gap profile landward gauge due to the structure reducing the incoming wave energy. The wave energy spectra is reduced to close to zero at the shortest wave periods with significant reductions in wave energy in the sea wave band of frequencies as shown in Figure 20.

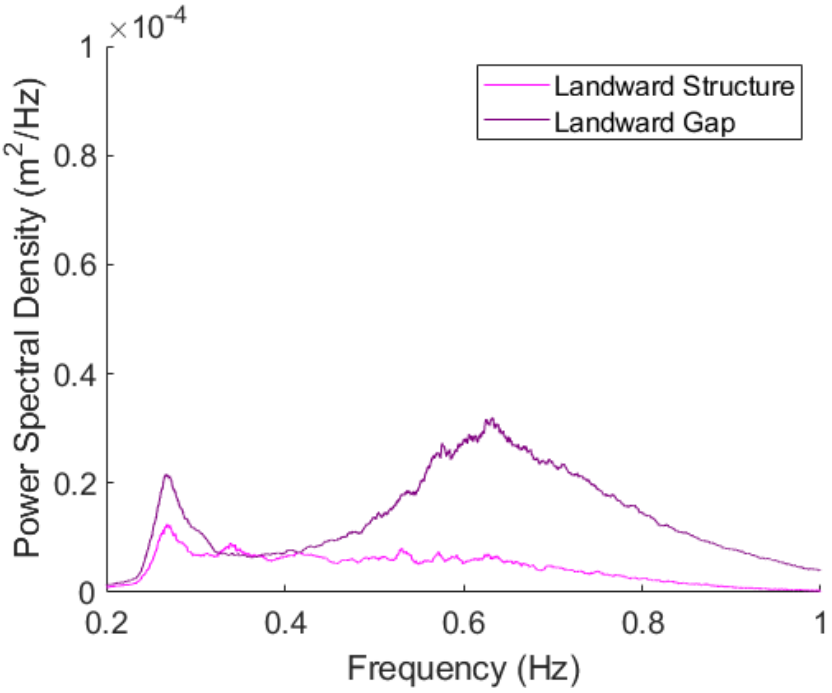

Figure 20: Power spectral density comparison of landward gauges

The comparison of marsh gauges between the two profiles in Figure 21 shows very little difference in wave energy spectra between the structure profile and the gap profile. At these locations, the vegetation has attenuated the wave energy to relatively equivalent levels.

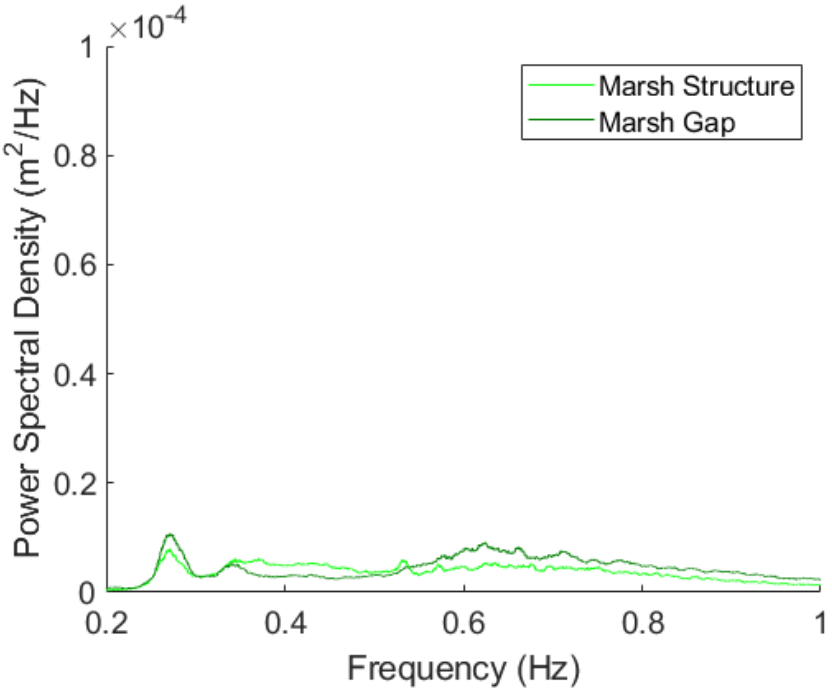

Figure 21: Power spectral density comparison of marsh gauges

Comparisons Along Each Profile

Wave shoaling occurs as water depths decrease causing an increase in wave height and energy until breaking or friction lead to dissipation. This is evident in Figure 22 with the changes in wave energy from the offshore gauge to the seaward gauges of the two profiles.

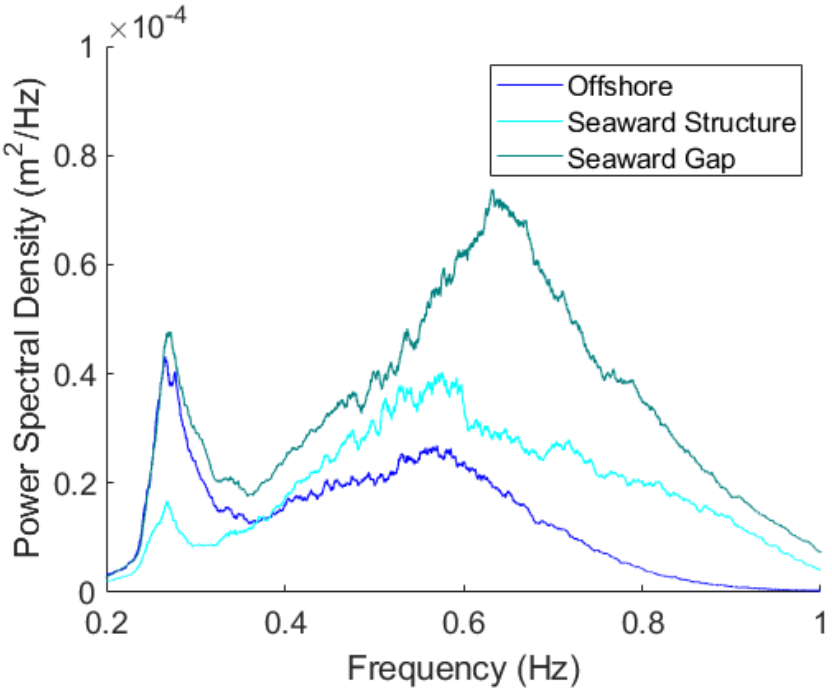

Figure 22: Increase in spectral energy from the offshore gauge to the seaward gauges

The effect of shoaling at the seaward gauges is assumed to be the same at both the gap and structure profiles since both gauges are located in approximately the same water depth and distance from the structure line. Since the seaward structure gauge captures the influence of wave reflection off the rock sill structure in addition to shoaling from the offshore gauge, one way to assess the overall wave attenuation capabilities of the structure is to compare the wave energy changes from the gap profile seaward gauge to the structure profile landward gauge as shown in Figure 23.

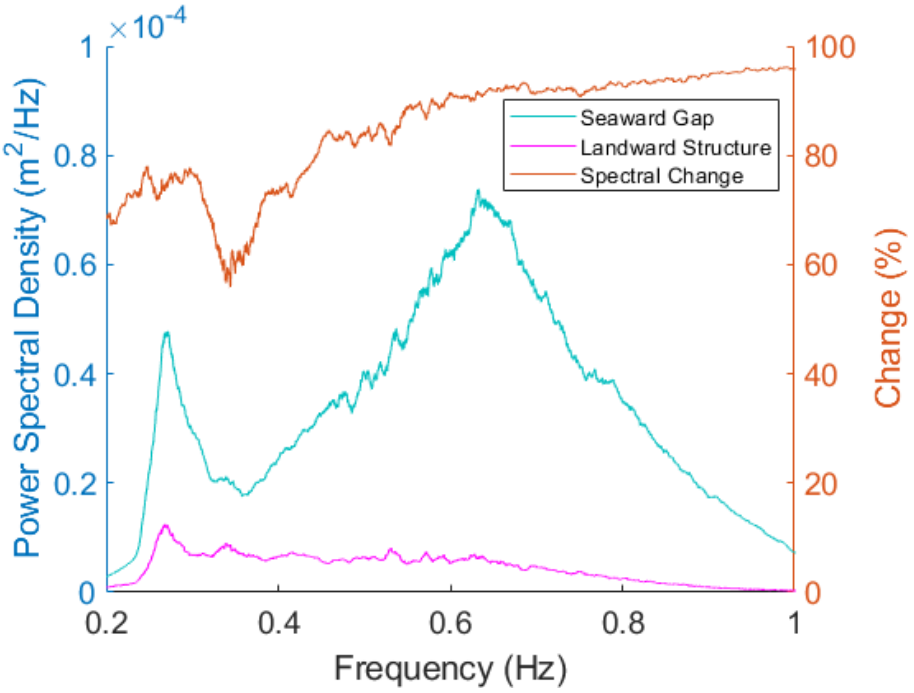

Figure 23: Spectral change between the gap profile seaward gauge and the structure profile landward gauge

Observing the spectral band from 0.2 Hz to 1 Hz, the attenuation of wave energy due to the structure ranges from 56% to 96% depending on the frequency. With the higher frequencies being more effectively attenuated by the structure than the lower frequencies. The structure has a significant effect on attenuating wave energy from transmitting past the structure and into the marsh vegetation. As shown in Figure 24, the wave energy has been attenuated so significantly by the structure that there is not much change in wave energy between the landward gauge and the marsh gauge. In fact, there is an increase in the short period wave energy between the landward gauge and marsh gauge. This may be attributed to the marsh gauge picking up wave interactions with vegetation stems.

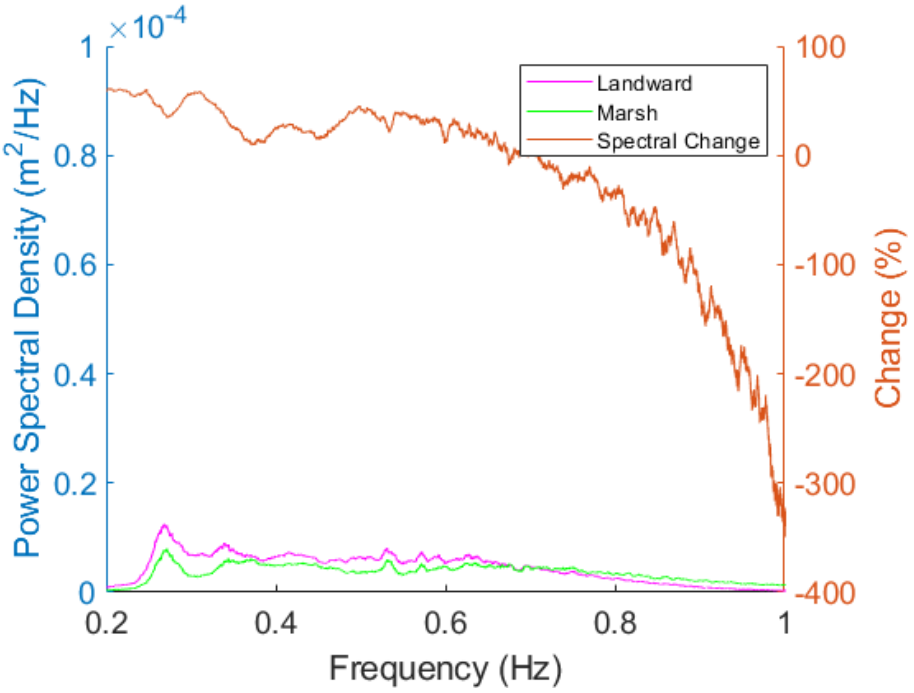

Figure 24: Spectral attenuation between the landward and marsh gauges of the structure profile

As mentioned above and shown in Figure 25, there is attenuation along the gap profile between the seaward and landward gauges. This attenuation ranges from 66% to 73% depending on the frequency and is attributed to diffraction, wave breaking as the water depth decreases, and the influence of the two sill structures on attenuating wave energy as the water moves through the gap between the structures.

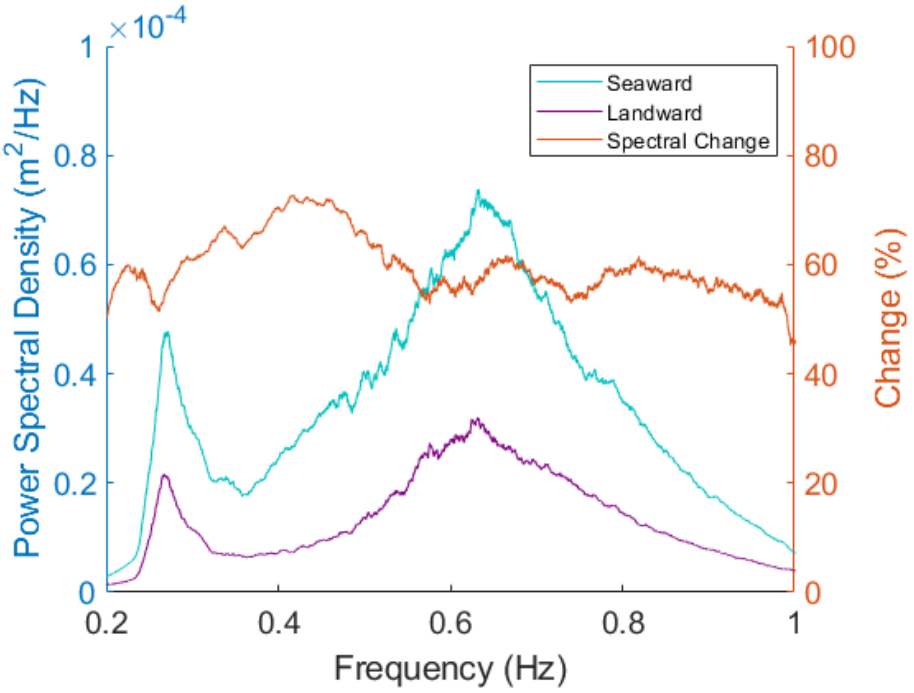

Figure 25: Attenuation between the seaward and landward gauges of the gap profile

There is still an observable amount of wave energy at the landward gap gauge, as shown in Figure 26, and the wave energy continues to attenuate, ranging from 25% to 80%, between the landward gauge and the marsh gauge, with the highest levels of attenuation occurring in the locally generated sea wave band.

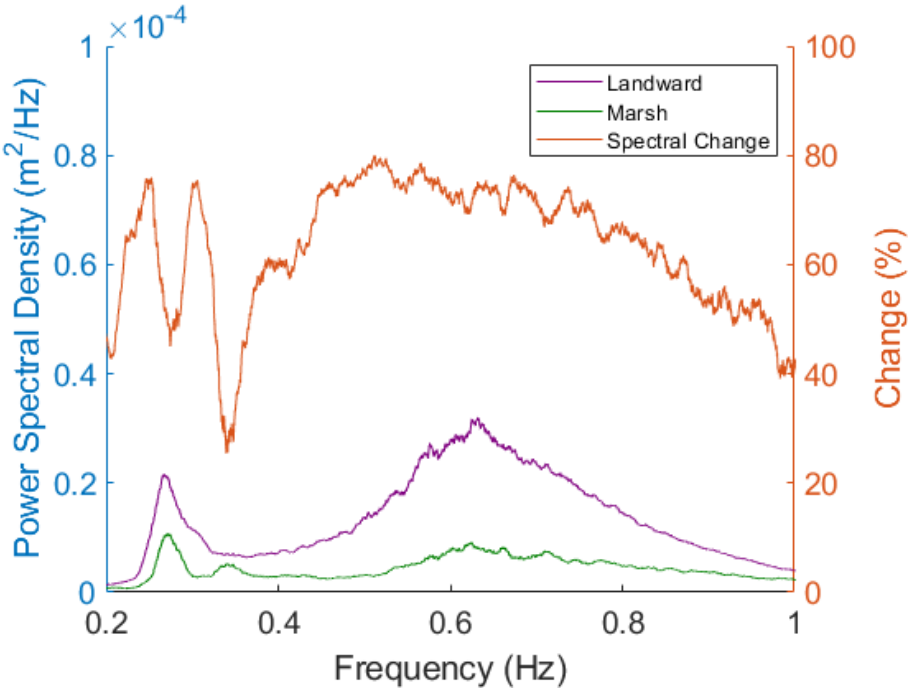

Figure 26: Spectral attenuation between the landward and marsh gauges of the gap profile

The results of the above analyses describe the site attenuation characteristics from an overall trend perspective. As previously mentioned, the overall deployment period was quiescent and captured smaller wave characteristics. To really explore the impact of the living shoreline system on attenuating wave energy and combating erosion along the shoreline, periods where there are increased water levels and wave energy are explored in the next section to fully capture the influence of the structure and vegetation on attenuating wave energy during the most impactful times.

3.4.2 Detailed Analyses

Detailed analyses of the deployment are conducted on multiple subsets of the deployment period. The focus of the field research in this study is the attenuation of wave energy attributed to the structure and vegetation. As previously mentioned, the overall deployment wave

characteristics tend towards predominantly small waves. For the purposes of this study, it is necessary to delve further into the time of wave activity where the effects of the sill structure and vegetation on wave attenuation for erosion protection can be best analyzed.

3.4.2.1 Vegetation Analysis

To this point, analyses are conducted when water depths at the marsh gauges can support wave heights above 0.01 meters, since smaller wave heights than those do not produce wave energy of any significance. As shown in Figure 27, 45% of the deployment period had water depths able to support waves of at least 0.01 meters at the gap profile marsh gauge.

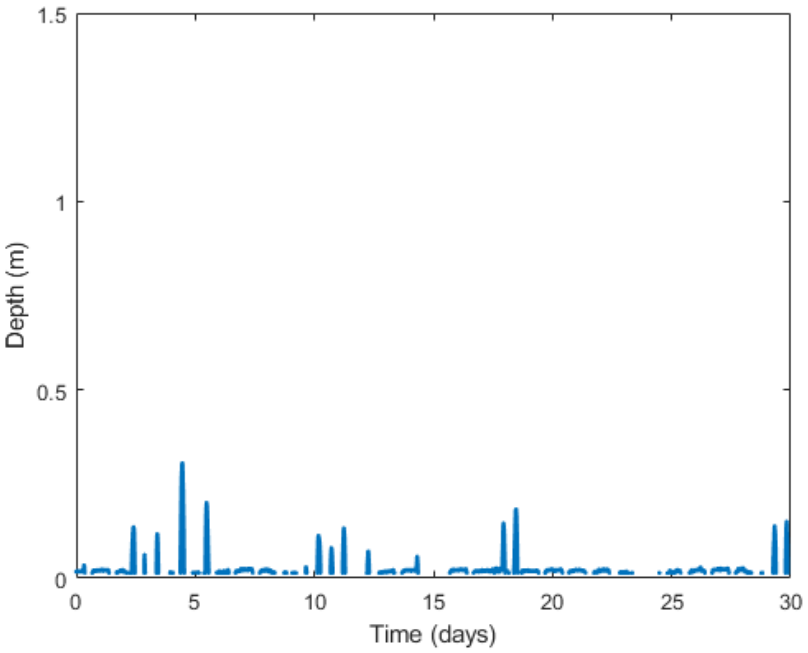

Figure 27: Water levels above 0.014 m during the deployment as measured at the gap profile marsh gauge

Spectral analysis is used to assess the changes between the gauges during the time identified for assessment. Figure 28 shows the differences across the gap profile and structure profile from the landward to the marsh gauges, while Figure 29 compares the landward and marsh gauges between the gap and structure profiles. These gauges show the influence of the vegetation portion of the living shoreline system on wave energy.

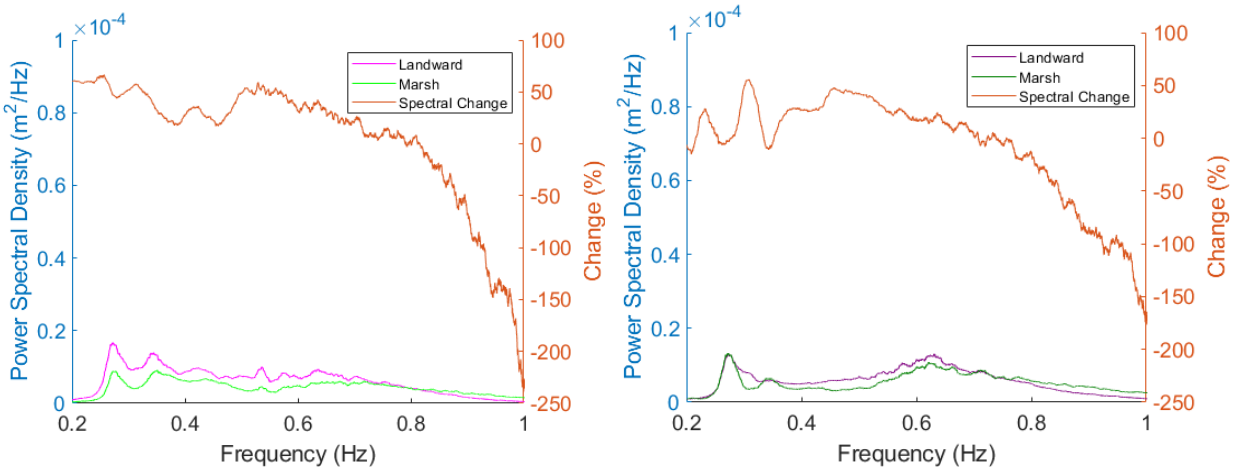

Figure 28: Change in wave energy between the landward and marsh gauges, structure profile on left, gap profile on right

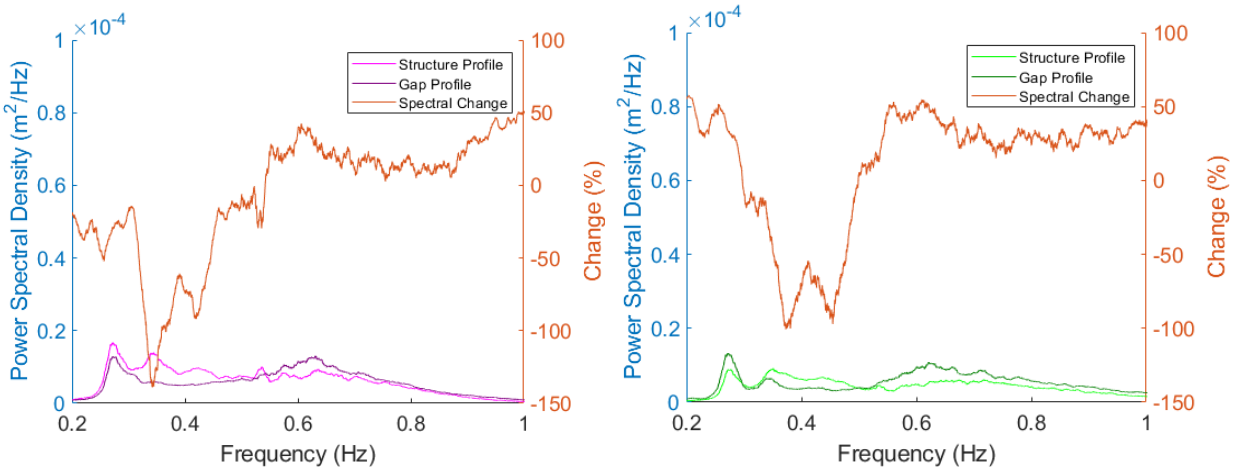

Figure 29: Wave spectra at the landward gauges, left, and the marsh gauges, right, when the water levels measured at the marsh gap profile gauge were at least 0.014 m

The structure profile has a decrease in wave energy from 0% to 67% between the landward and marsh gauges from the 0.2 to 0.8 Hz frequencies. The gap profile has similar wave energy spectra between the landward and marsh gauges, with some slight decreases between 0.35 and 0.7 Hz frequencies. The first peak, attributed to boat wake waves, at the lower end of frequencies is still apparent in both the structure and gap profiles. The sea wave band peak has been dissipated along the structure profile, but it is still apparent in the gap profile indicating wave energy at these frequencies is not being attenuated through the gap to the degree that the structure is attenuating this wave energy.

Attenuation is greater along the lower frequencies of the structure profile as compared to the gap profile; however, there is higher wave energy in the sea wave frequency band along the gap profile and minimal change from the landward gap profile gauge to the marsh gap profile gauge. An interesting item to note is that the landward structure profile gauge has higher wave energy in the lower frequencies than the landward gap profile gauge. This differs from the results

from the full deployment, indicating potential setup landward of the structure as the water levels increase.

3.4.2.2 Structure Analysis

This section of analysis focuses first on when the water depth at the landward gauge is able to support wave heights at or above 0.01 meters, similar to the vegetation analysis of the previous section, to observe any influence the structure has on wave energy attenuation. The second section of the structure analysis further limits the dataset to the period when the crest of the structure is submerged.

Landward Gap Gauge Limit Assessment

The water levels at the gap profile landward gauge were able to support a 0.01 meter wave the majority (74%) of the deployment period as shown in Figure 30.

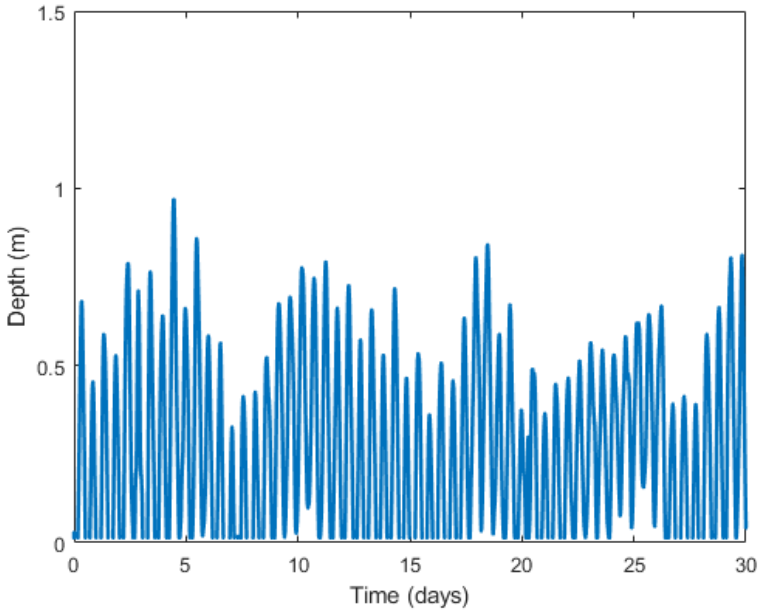

Figure 30: Water levels above 0.014 m during the deployment as measured at the gap profile landward gauge

Figure 31 shows the differences between the gap profile and structure profile seaward and landward gauges. These gauges show the influence of the structure portion of the living shoreline system on wave energy. As with the overall deployment assessment above, the gap profile seaward gauge is used to determine wave energy attenuation due to the structure to remove the influence of wave reflection off the structure in the analysis.

The attenuation attributed to the structure from calculating change at the landward structure profile gauge reveals that the structure attenuates wave energy between 28% and 86%. Observing the same gauge positions across the gap profile, the wave energy still shows attenuation in the range of 10% to 71%; however, the sea wave frequency band peak is still observable along the gap profile, whereas the structure has completely attenuated this peak landward of the structure.

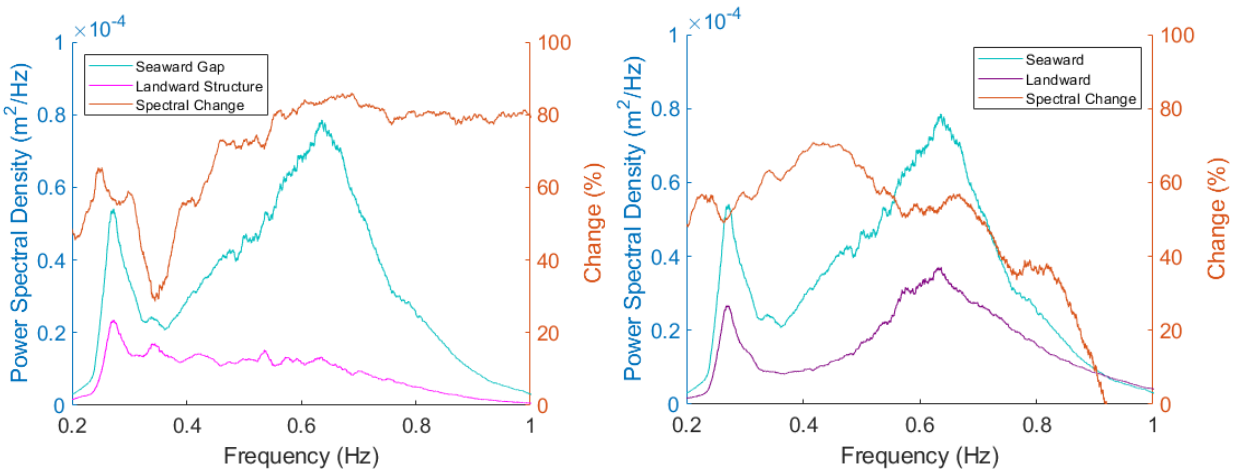

Figure 31: Change in wave energy between the landward and marsh gauges, structure profile on left, gap profile on right

While the seaward gap gauge was used to determine attenuation attributed solely to transmission across the structure and not include wave reflection off the structure, it is interesting to note that the seaward structure gauge did not have as much wave reflection during this period as compared to the full deployment assessment as shown in Figure 32.

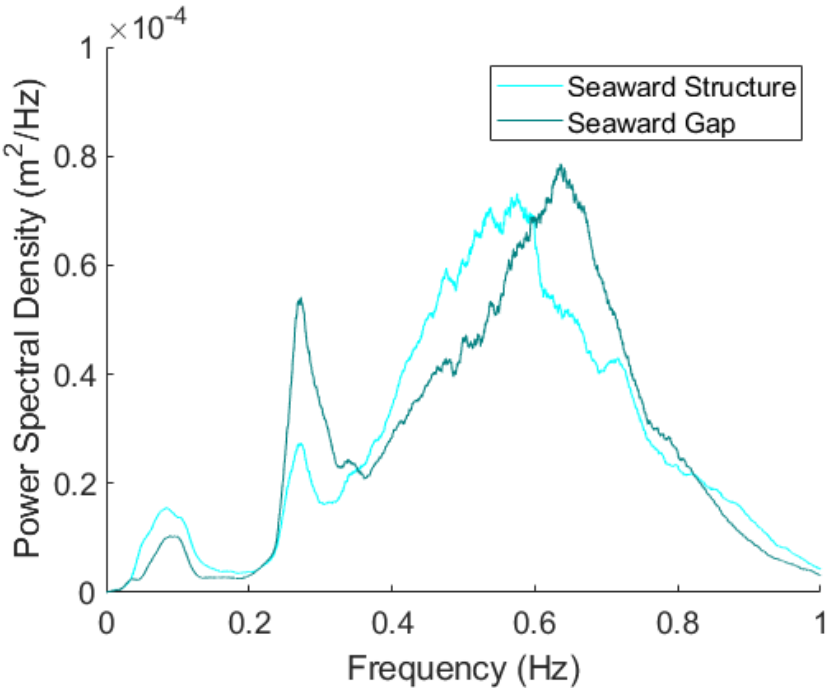

Figure 32: Wave spectra at the seaward gauges when the water levels measured at the landward gap profile gauge were at least 0.014 m

Submerged Crest Assessment

As mentioned above in Section 3.1, the water levels during the deployment are higher than predicted for the majority of the deployment period. This provides additional periods during which the structure crest is submerged than would have been anticipated in the design of the

structure. That being said, the structure is only submerged 6% of the deployment period as measured by water levels at the structure profile seaward gauge and shown in Figure 33.

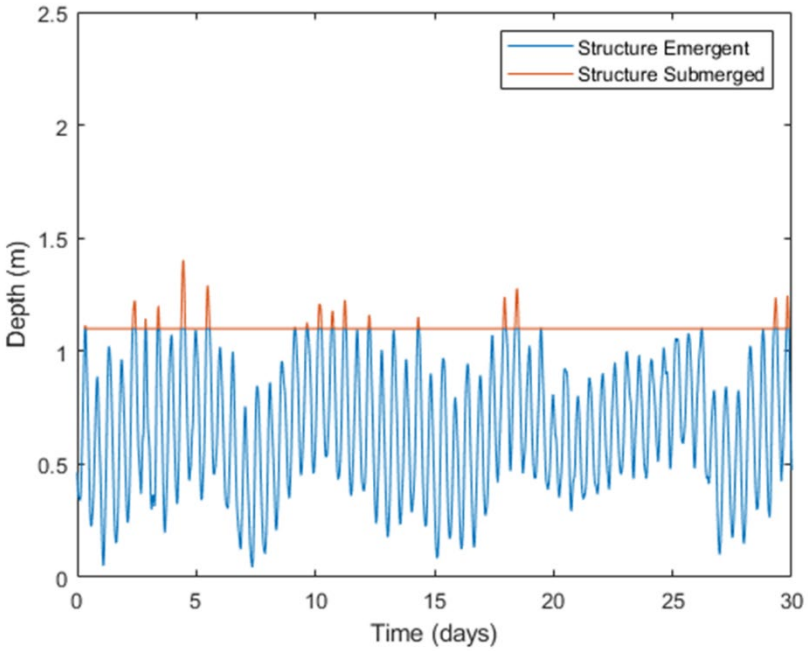

Figure 33: Structure crest emergence versus submergence during the deployment

Figure 34 shows the differences between the gap profile and structure profile seaward and landward gauges when the structure crest is submerged. These gauges show the influence of the structure portion of the living shoreline system on wave energy as water levels and structure freeboard increase.

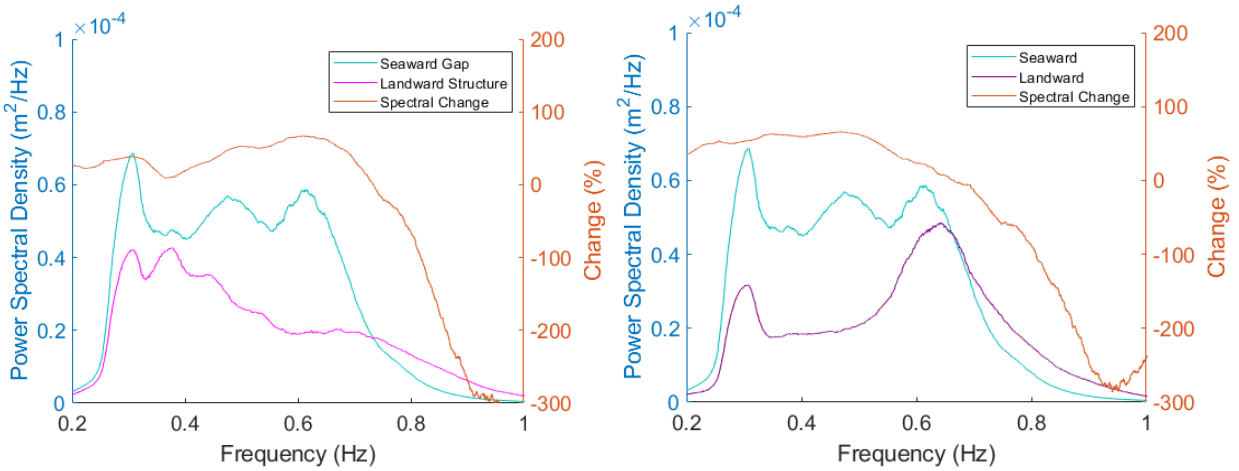

Figure 34: Change in wave energy between the landward and marsh gauges when the crest is submerged, structure profile on left, gap profile on right

As with the previous assessment of the structure, the sea wave band peak is significantly reduced along the structure profile between the seaward and landward gauges indicating the influence of the structure on attenuating wave energy. Interestingly, the wave energy at the lower end of the frequencies is not attenuated as much landward of the structure as it is at the gap profile landward structure. The structure profile attenuates wave energy across the structure in the range of 0% to 67% and switches to a slight increase of wave energy at the higher frequencies of 0.75 Hz and greater. The gap profile shows a similar increase in wave energy at the higher frequencies with the switch from reduction to increase occurring at 0.65 Hz and higher. Prior to that point, the gap profile shows attenuation between the seaward and landward gauges of 0% to 66% with the greatest attenuation occurring between the two frequency peaks.

Statistical Windowing

The next chapter of this study will discuss using these field data to calibrate and validate a numerical model. To do this, periods of field data must be selected from which the model can

be calibrated and validated. While a large portion of the analysis above looks at the wave energy attenuation due to frequency, specific wave characteristics are required for input into the numerical model described in the next chapter. Another method of analysis to observe overall wave trends that would be suitable for calibrating and validating the numerical model is looking at changing wave characteristics temporally through statistical windowing. To this end, the wave height and period data are windowed at hourly duration with a 50% overlap, as shown in Figure 35 for the offshore gauge.

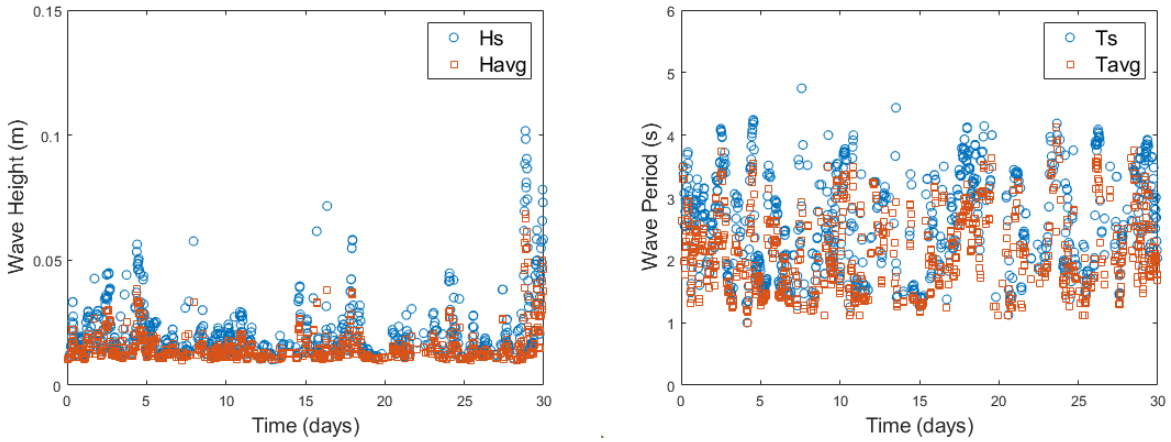

Figure 35: Windowed wave statistics at the offshore gauge

Since the study seeks to observe wave attenuation due to the structure and vegetation, the data where water levels are able to support waves at the marsh gauge are compared to the windowed significant wave heights that occur at the offshore gauge, as shown in Figure 36. In order to observe measurable changes in attenuation across the structure and gap profiles when

looking at wave heights, it was determined to narrow the events to periods when the time windowed wave heights reached a minimum of 0.05 m as shown in Figure 37.

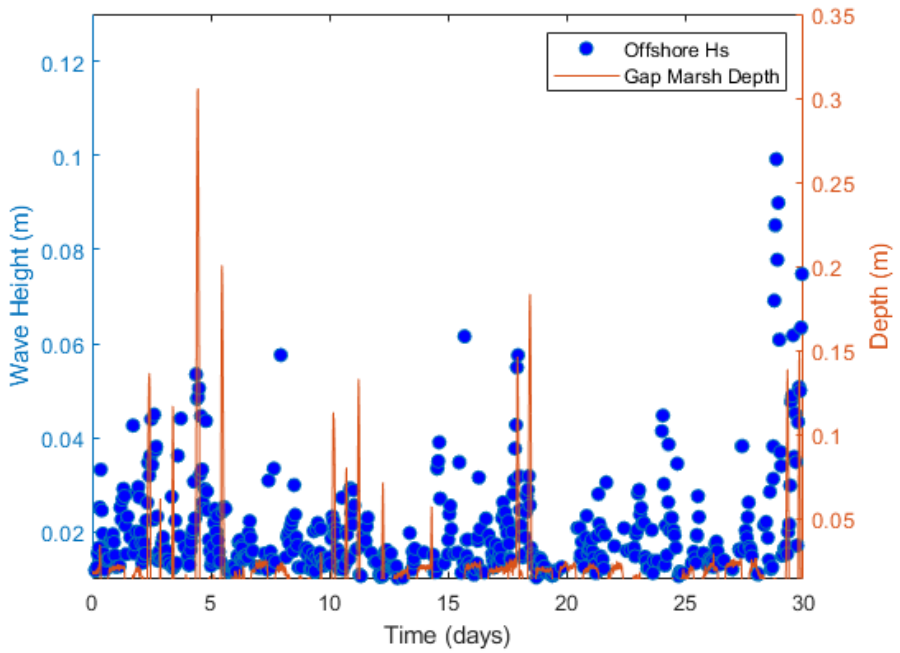

Figure 36: Water depths at the marsh gap gauge versus windowed significant wave heights at the offshore gauge

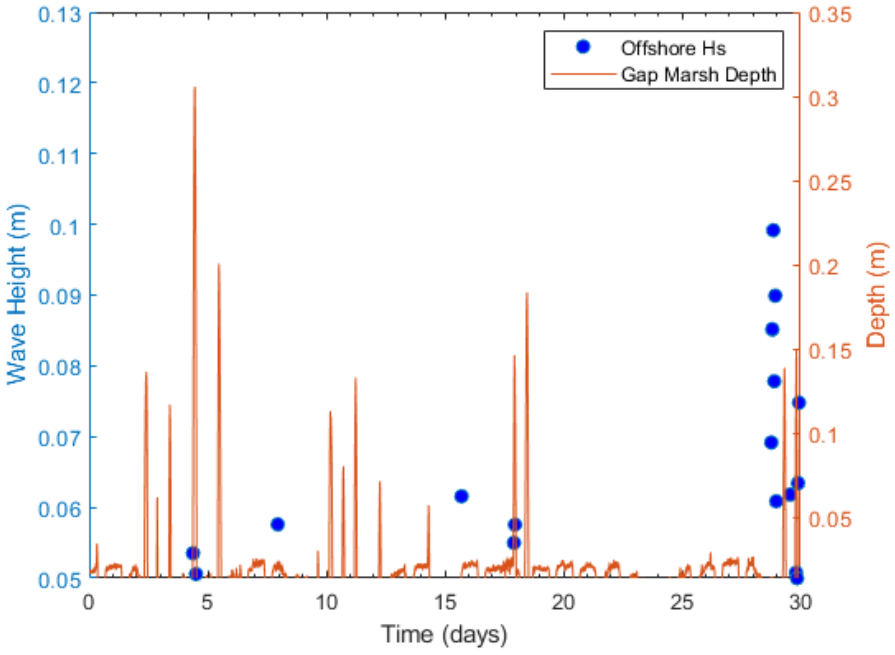

Figure 37: Significant wave heights at the offshore gauge exceeding 0.05 m versus water depth at the gap marsh gauge

Two of the events, day 7 and day 15, that meet the initial criteria for analysis in this section are during times of very low water at the marsh gauge and, as shown in Figure 38, occur during periods of the lowest tides of the deployment when observing the water levels at the offshore gauge. Observing the potential noise in the depth signal and analyzing the data for a wave spectrum at the marsh gauge, as shown in Figure 39, reveal that these two events do not produce data that can provide meaningful results. These two events were not considered for further analysis in this section.

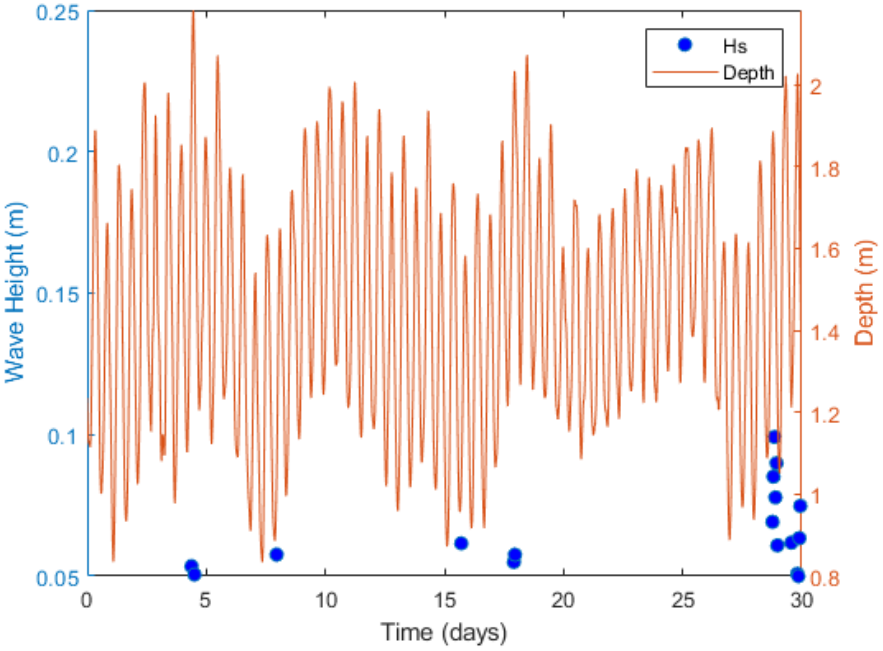

Figure 38: Significant wave heights exceeding 0.05 m versus water depth at the offshore gauge

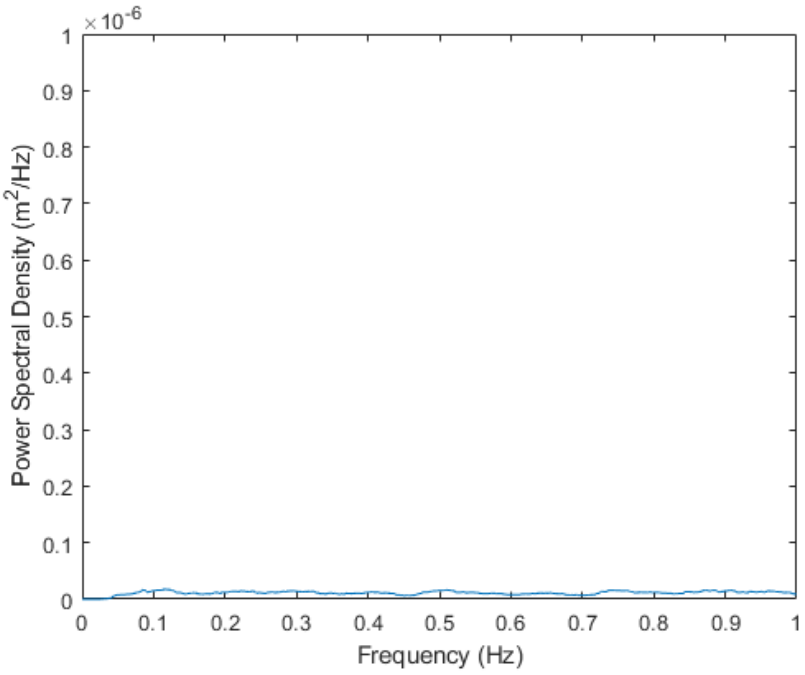

Figure 39: Wave spectrum analysis result at the marsh gauge for the event on day 7

The three remaining events during the deployment, days 4, 17, and 28, are further analyzed for use in the numerical model described in the next chapter. A brief summary of the wave characteristics of these events in described here. The wave characteristics for the three events are shown in Table 2 and the wave energy spectra are shown in Figure 40 to Figure 42.

Table 2: Wave Characteristics for Three Events

	Hs (m)	Tp (s)	Depth (m)
Event 1	0.05	3.8	1.94-2.18
Event 2	0.06	3.0	1.96-2.03
Event 3	0.06	1.8	1.05-2.03

Event 1

Event 1 occurred on the fourth day of the deployment, November 26, 2018, and lasted 3.1 hours.

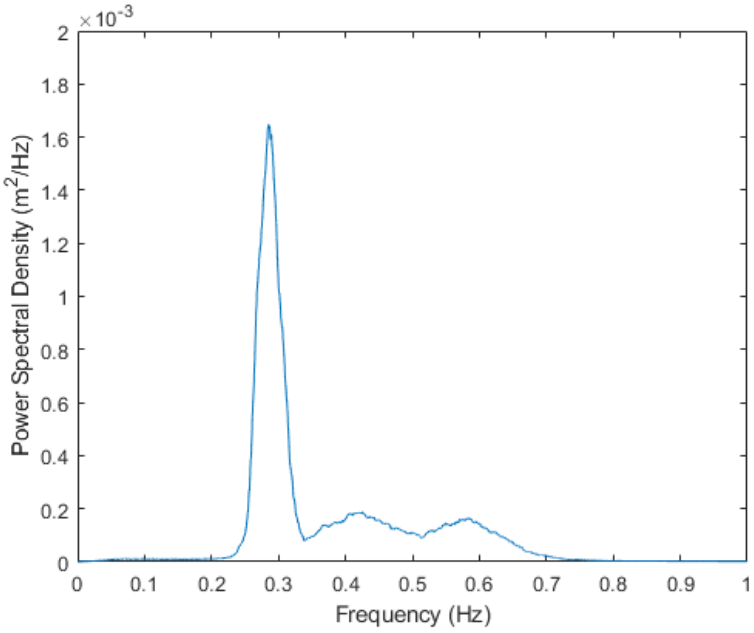

Figure 40: Wave energy spectrum for Event 1

This spectrum shows a strong peak in the lower frequency of the spectrum around 0.3 with additional peaks in the sea wave band from 0.35 to 0.7 that are much lower. Previous analysis of the full deployment spectrum reveals two peaks; however, this period of data is predominantly peaked at the lower frequency peak. This lower frequency peak is in the range of boat wakes, and the project site has dock access and occasional boat traffic, so there may have been boat traffic that occurred during this period to influence the strong lower frequency peak.

Event 2

Event 2 was a 1.2-hour event that occurred on the 17th day of the deployment, December 8, 2018, and has a clearly defined single peak spectrum in the sea wave band.

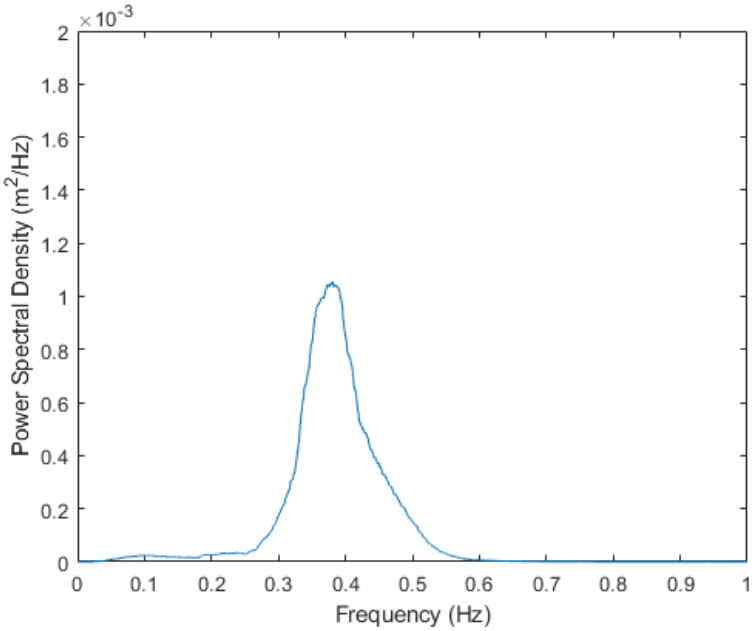

Figure 41: Wave energy spectrum for Event 2

Event 3

Event 3 occurred at the end of the deployment from day 28 to 30, December 19-21, 2018. This is the longest lasting event at 32.4 hours and has the highest waves of the deployment.

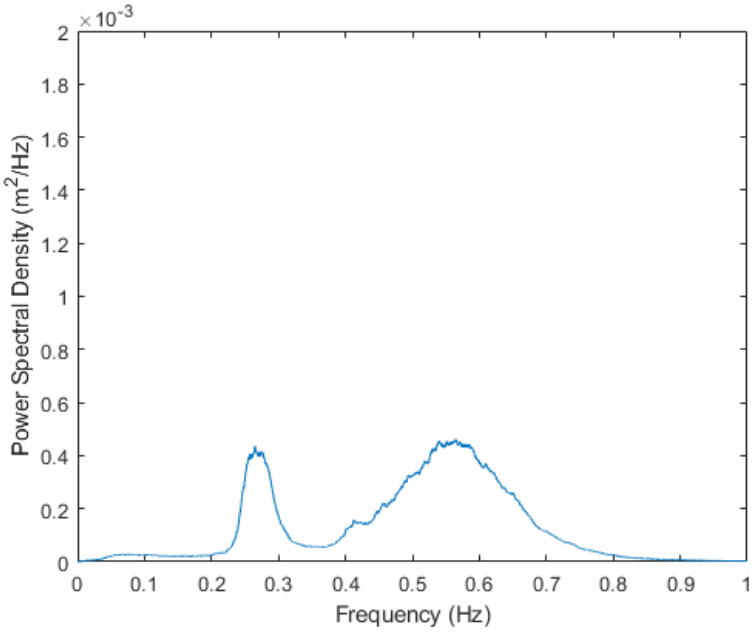

Figure 42: Wave energy spectrum for Event 3

This event has the two peaks apparent in the overall deployment which are of similar magnitudes. Further analysis and discussion of these events is provided in the next chapter as they pertain to the numerical modeling analysis.

3.5 Discussion

The results of the field data analysis reveal that the structure has a significant impact on the reduction of wave energy across the sill structure. Each section of deployment data assessed reveals a difference in wave energy at the landward gauges from the full deployment period to the subsets looking only at the structure influence. From an engineering assessment standpoint it is clear that the structure portion of the living shoreline design performs as expected. It is also interesting to note that prior to transmission past the structure wave energy is already being attenuated by wave reflection off of the structure. Wave reflection off of the structure is

significant in the overall deployment analysis, but its influence decreases as water levels increase as shown in Figure 32. The sea wave band of 0.4 to 1 Hz is significantly attenuated both by the structure and the vegetation.

In the overall deployment assessment, there is not a significant difference between the structure profile marsh gauge wave energy and the gap profile marsh gauge wave energy. This is indicative of the effect of marsh vegetation on wave energy attenuation and indicates that the marsh sill living shoreline as a system has reduced the wave energy to near zero at this distance, approximately 5 meters, into the vegetation. While the sill structure is able to significantly reduce the wave energy, the gap profile gauge shows that a few meters into the marsh similar amounts of wave energy attenuation have been achieved by the vegetation when comparing the gap profile to the structure profile. At the location of these gauges, approximately five meters into the marsh vegetation, the effect of the structure is no longer apparent on the wave energy attenuation and the attenuation observed here is the result of the marsh vegetation. The attenuation effect of marsh vegetation has been noted in previous research and has highlighted the need for protecting and preserving fringing marshes as part of erosion control design (Shepard et al., 2011).

Prior to the construction of the living shoreline system at this site, there was marsh edge erosion. While the overall deployment does not show much difference in wave energy between the structure profile marsh gauge and the gap profile marsh gauge, there are some differences when analyzing the time periods of increased water levels at these gauges. In the vegetation section of analysis that looks at a smaller subsection of the deployment, the structure has attenuated wave energy and reduced the sea wave peak at the landward gauge which is further attenuated at the marsh gauge. Conversely, there is still a slight peak at the landward gap profile

gauge that has not been attenuated and there is not much effect on this wave energy by the vegetation at the marsh gauge. This shows that while the marsh vegetation is effective at attenuating wave energy there is still a greater amount of wave energy attenuation that can be attributed to the structure influence into the marsh. While this study is comparing gauges between the structure profile and the gap profile, the overall living shoreline system is still providing wave energy attenuation benefits to the sections of marsh in the gap greater than what was provided prior to the construction of the living shoreline system.

Although water levels at the site were higher than predicted, the crest of the sill structure was only submerged for 6% of the deployment period. The vegetation was shown to attenuate wave energy so, the question becomes, could the structure crest elevation be reduced and still provide effective wave attenuation to prevent the majority of the marsh edge erosion that was occurring prior to the installation of the project? The assessment of the structure reveals that when the crest height is submerged, the structure was able to attenuate wave energy on the order of 0% to 67%, with the greatest attenuation occurring in the sea wave frequency band. While not the focus of this study, it should be noted that there were periods of boat wake waves that occurred during the deployment and neither the structure profile nor the gap profile appears to be effective at significantly attenuating wave energy at these lower frequencies of 0.2 to 0.3 Hz. At this site, these waves do not constitute the majority of the wave energy that is eroding the shoreline, so the crest height attenuating naturally generated sea waves is the greater concern. However, this could be a greater concern at sites where boat wakes are a significant contributor to marsh edge erosion. While there will be a point at which structure freeboard will exceed any influence the structure has on wave energy attenuation, the design life of the shoreline erosion protection project will be able to accommodate an amount of increased water level (e.g., sea

level rise) and still attenuate wave energy through a combination of structure and vegetation influence.

3.6 Conclusions

The results of this assessment are able to quantify that a structure can help attenuate wave energy enough to prevent marsh edge erosion and then allow the marsh vegetation to do its part in wave energy attenuation as a key part of the overall erosion protection system. The attenuation of wave energy due to the structure on the structure profile ranges from 56% to 96%, depending on the frequency, and the marsh vegetation between the landward and marsh gauges of the structure profile attenuated wave energy from 0% to 67%. The gap profile revealed wave energy attenuation from 66% to 73% between the seaward and landward gauges and 25% to 80% between the landward and marsh gauges, without the attenuation in the sea wave band that is apparent in the structure profile.

The next step to discover how to potentially optimize these structures is to utilize numerical modeling methods to look at alternative scenarios and determine how the living shoreline erosion protection system might perform with lower structure crest heights and if these structures could then provide sufficient protection to the upland while allowing further land water interaction. Additionally, assessing the adaptation potential for this type of shoreline erosion protection is vital to influencing guidance and how best to utilize a living shoreline erosion protection design when assessing armored shoreline and landward retreat options in the face of sea level rise.

CHAPTER 4 NUMERICAL MODELING

Numerical modeling provides a platform upon which complex calculations of the wave environment can be assessed in an efficient manner under a variety of user-defined conditions. These tools allow engineers to determine the effects a shoreline erosion project may have on an existing shoreline with a relative degree of certainty given the available data and the ruggedness and reliability of the model being utilized. Therefore, models must be calibrated and validated under a variety of circumstances to determine their effectiveness, and limitations, at providing reliable assessment outcomes for new designs. Field data collection is important in determining how existing shoreline projects perform on eroding shorelines. This allows designers to obtain the data necessary to continually learn about and improve upon shoreline erosion protection design. In the absence of a plethora of field data, numerical models can be utilized to help assess how a potential shoreline project design may perform in the natural world. Along the same vein, these numerical models must be calibrated and validated to ensure that the results that are obtained are reasonable assessments of design performance to be considered a good tool to use for project design. For this study, the field data collected at the Captain Sinclair Recreational Area living shoreline (Captain Sinclair), described in Chapter 3, is used for calibration and validation of the numerical modeling component of the study. This allows the researcher to analyze how the Captain Sinclair shoreline may potentially perform under a variety of different circumstances related to the structure crest height and water levels.

4.1 NHWAVE

The Non-Hydrostatic WAVE model, NHWAVE, is a numerical model capable of simulating wave refraction, diffraction, shoaling, breaking, landslide tsunami generation, and

longshore current (Ma et al., 2012). An advantage to using NHWAVE, as compared to some previous hydrodynamic numerical models, is the reduced run time that is a result of obtaining acceptable results with relatively few vertical layers (3-5) (Ma et al., 2012). It is selected for this study to determine the effectiveness of its use in assessing living shoreline designs that incorporate both structural and vegetation components. Additions to the original NHWAVE model have occurred since 2012, and the model has the capacity to incorporate both porous media, e.g., breakwater, sills, etc., and vegetation characteristics into the model setup. The addition of these two modules makes it a suitable numerical model to use to assess living shorelines. However, this model has previously not been used to determine the effectiveness of assessing both components simultaneously. Since it has not previously been used to evaluate a marsh sill living shoreline design, this study examines if the model shows the necessary capability to account for the dynamic interactions when the two modules are combined.

The next sections provide an overview of the model formulation and numerical implementation which is available in greater depth in (Ma et al., 2012, 2013, 2014).

4.1.1 Governing Equations

NHWAVE solves the incompressible Navier-Stokes equations. The model was adapted to simulate turbulent flow through vegetation with a two-equation k- ε turbulence model (Ma et al., 2013) and further updated to include the ability to simulate wave interaction with porous media (Ma et al., 2014) by solving the volume-averaged Reynolds-averaged Navier-Stokes equations (VARANS). Equations (1) and (2) show these VARANS equations, with the formulation based on (del Jesus et al., 2012), in Cartesian coordinates (x_1^*, x_2^*, x_3^*), where $x_1^* = x^*, x_2^* = y^*$, and $x_3^* = z^*$ and time t^* are given by

$$\frac{\partial}{\partial x_i^*}\frac{u_i}{n} = 0 \tag{1}$$

$$\frac{\partial}{\partial t^*}\frac{u_i}{n}+\frac{u_j}{n}\frac{\partial}{\partial x_j^*}\frac{u_i}{n}=-\frac{1}{\rho}\frac{\partial p}{\partial x_i^*}+g_i+\frac{\partial}{\partial x_j^*}\left[(\nu+\nu_t)\frac{\partial}{\partial x^*}\frac{u_i}{n}\right]+\boldsymbol{R}\frac{u_i}{n}+f_{Fi}+f_{Vi} \tag{2}$$

where $(i,j)=1,2,3$, u_i is the velocity component in the x_i^* direction, n is porosity, p is total pressure, ρ is water density, $g_i=-g\delta_{i3}$ is the gravitational body force, with ν the laminar kinematic viscosity, and ν_t the turbulent kinematic viscosity. The fourth term is related to the porous media component, given by

$$\boldsymbol{R}=-a_p-b_p\left|\frac{\boldsymbol{u}}{n}\right|-c_p\frac{\partial}{\partial t} \tag{3}$$

where $|\boldsymbol{u}|=\sqrt{\sum_i u_i^2}$ and, as given by (van Gent, 1994) and (Liu et al., 1999),

$$a_p=\alpha\frac{(1-n)^2}{n^2}\frac{\nu}{D_{50}^2} \tag{4}$$

$$b_p=\beta\left(1+\frac{7.5}{KC}\right)\frac{1-n}{n^2}\frac{1}{D_{50}} \tag{5}$$

$$c_p=\gamma\frac{1-n}{n} \tag{6}$$

where α and β are coefficients to be determined, γ is an empirical coefficient usually assumed at 0.34 (Liu et al., 1999), D_{50} is the nominal diameter of the porous material, KC is the Keulegan-Carpenter number defined as $KC=\frac{|\boldsymbol{u}|T}{nD_{50}}$, with T being the typical wave period. The final two terms of Eq. (2) relate to the vegetation component with form, f_{Fi}, and viscous, f_{Vi}, drag modeled as

$$f_{di}=f_{Fi}+f_{Vi}=\frac{1}{2}C_D\lambda u_i|\boldsymbol{u}| \tag{7}$$

where C_D is the drag coefficient, $\lambda=b_vN$ is the vegetation density, b_v is the stem size, and N is the number of stems per unit area.

Bottom and surface geometry are represented by a σ-coordinate developed by (Phillips, 1957),

$$t = t^* \quad x = x^* \quad y = y^* \quad \sigma = \frac{z^* + h}{D} \tag{8}$$

where $D(x, y, t) = h(x, y) + \eta(x, y, t)$, h is water depth, η is surface elevation. The physical domain varying vertical coordinate is transformed by this approach into a uniform space where σ ranges from 0 to 1 (Lin & Li, 2002) and the governing equations become

$$\frac{\partial D}{\partial t} + \frac{\partial}{\partial x}\frac{Du}{n} + \frac{\partial}{\partial y}\frac{Dv}{n} + \frac{\partial}{\partial \sigma}\frac{\omega}{n} = 0 \tag{9}$$

$$\left(1 + c_p\right)\frac{\partial \boldsymbol{U}}{\partial t} + \frac{\partial \boldsymbol{F}}{\partial x} + \frac{\partial \boldsymbol{G}}{\partial y} + \frac{\partial \boldsymbol{H}}{\partial \sigma} = \boldsymbol{S}_h + \boldsymbol{S}_p + \boldsymbol{S}_\tau + \boldsymbol{S}_r + \boldsymbol{S}_v \tag{10}$$

where $\boldsymbol{U} = (\frac{Du}{n}, \frac{Dv}{n}, \frac{Dw}{n})^T$ and the fluxes are:

$$\boldsymbol{F} = \begin{pmatrix} \frac{Duu}{n^2} + \frac{1}{2}g\eta^2 + gh\eta \\ \frac{Duv}{n^2} \\ \frac{Duw}{n^2} \end{pmatrix} \quad \boldsymbol{G} = \begin{pmatrix} \frac{Duv}{n^2} \\ \frac{Dvv}{n^2} + \frac{1}{2}g\eta^2 + gh\eta \\ \frac{Dvw}{n^2} \end{pmatrix} \quad \boldsymbol{H} = \begin{pmatrix} \frac{u\omega}{n^2} \\ \frac{v\omega}{n^2} \\ \frac{w\omega}{n^2} \end{pmatrix}$$

The source terms are defined as

$$\boldsymbol{S}_h = \begin{pmatrix} gD\frac{\partial h}{\partial x} \\ gD\frac{\partial h}{\partial y} \\ 0 \end{pmatrix} \quad \boldsymbol{S}_p = \begin{pmatrix} -\frac{D}{\rho}\left(\frac{\partial p}{\partial x} + \frac{\partial p}{\partial \sigma}\frac{\partial \sigma}{\partial x^*}\right) \\ -\frac{D}{\rho}\left(\frac{\partial p}{\partial y} + \frac{\partial p}{\partial \sigma}\frac{\partial \sigma}{\partial y^*}\right) \\ -\frac{1}{\rho}\frac{\partial p}{\partial \sigma} \end{pmatrix} \quad \boldsymbol{S}_\tau = \begin{pmatrix} DS_{\tau_x} \\ DS_{\tau_y} \\ DS_{\tau_z} \end{pmatrix}$$

$$\boldsymbol{S}_r = \begin{pmatrix} -a_p\frac{Du}{n} - b_p\left|\frac{\boldsymbol{u}}{\boldsymbol{n}}\right|\frac{Du}{n} + c_p\frac{u\partial D}{n\,\partial t} \\ -a_p\frac{Dv}{n} - b_p\left|\frac{\boldsymbol{u}}{\boldsymbol{n}}\right|\frac{Dv}{n} + c_p\frac{v\partial D}{n\,\partial t} \\ -a_p\frac{Dw}{n} - b_p\left|\frac{\boldsymbol{u}}{\boldsymbol{n}}\right|\frac{Dw}{n} + c_p\frac{w\partial D}{n\,\partial t} \end{pmatrix} \quad \boldsymbol{S}_v = \begin{pmatrix} D(f_{dx} + f_{vmx}) \\ D(f_{dy} + f_{vmy}) \\ D(f_{dz} + f_{vmz}) \end{pmatrix}$$

where total pressure is separated into dynamic pressure, p, and hydrostatic pressure, $\rho g(\eta - z)$, $DS_{\tau_x}, DS_{\tau_y}, DS_{\tau_z}$ are turbulent diffusion terms, and ω is the vertical velocity defined as

$$\frac{\omega}{n} = D\left(\frac{\partial \sigma}{\partial t^*} + \frac{u}{n}\frac{\partial \sigma}{\partial x^*} + \frac{v}{n}\frac{\partial \sigma}{\partial y^*} + \frac{w}{n}\frac{\partial \sigma}{\partial z^*}\right) \tag{11}$$

with

$$\begin{gathered} \frac{\partial \sigma}{\partial t^*} = -\frac{\sigma}{D}\frac{\partial D}{\partial t} \\ \frac{\partial \sigma}{\partial x^*} = \frac{1}{D}\frac{\partial h}{\partial x} - \frac{\sigma}{D}\frac{\partial D}{\partial x} \\ \frac{\partial \sigma}{\partial y^*} = \frac{1}{D}\frac{\partial h}{\partial y} - \frac{\sigma}{D}\frac{\partial D}{\partial y} \\ \frac{\partial \sigma}{\partial z^*} = \frac{1}{D} \end{gathered} \tag{12}$$

Using the boundary conditions for ω and integrating Eq.(10) with σ = 0 to 1, the governing equations for free surface movement become

$$\frac{\partial D}{\partial t} + \frac{\partial}{\partial x}\left(D\int_0^1 \frac{u}{n}\partial\sigma\right) + \frac{\partial}{\partial y}\left(D\int_0^1 \frac{v}{n}\partial\sigma\right) = 0 \tag{13}$$

4.1.2 Turbulence Model

The nonlinear k- ε model (Lin & Liu, 1998a, 1998b) is employed in NHWAVE with a volume-averaged approach (Hsu et al., 2002). The eddy viscosity is calculated by

$$\nu_t = C_\mu \frac{k^2}{n\epsilon} \tag{14}$$

The $k - \varepsilon$ equations in conservative form are given as

$$\frac{\partial}{\partial t}\left(\frac{Dk}{n}\right) + \nabla\cdot\left(\frac{D\boldsymbol{u}k}{n^2}\right) = \nabla\cdot\left[D\left(\nu + \frac{\nu_t}{\sigma_k}\right)\nabla\frac{k}{n}\right] + D\left(P_s + C_{fk}P_v - \frac{\epsilon}{n}\right) + D\epsilon_\infty \tag{15}$$

$$\frac{\partial}{\partial t}\left(\frac{D\epsilon}{n}\right) + \nabla\cdot\left(\frac{D\boldsymbol{u}\epsilon}{n^2}\right) = \nabla\cdot\left[D\left(\nu + \frac{\nu_t}{\sigma_\epsilon}\right)\nabla\frac{\epsilon}{n}\right] + \frac{\epsilon}{k}D\left(C_{1\epsilon}(P_s + C_{f\epsilon}P_v) - C_{2\epsilon}\frac{\epsilon}{n}\right) + DC_{2\epsilon}\frac{\epsilon_\infty^2}{k_\infty} \tag{16}$$

ϵ_∞ and k_∞ are closure for porous media flow, given by (Hsu et al., 2002) and (Nakayama & Kuwahara, 1999) as

$$\epsilon_\infty = 39.0\frac{(1-n)^{2.5}}{n}\left(\sum_i u_i^2\right)^{3/2}\frac{1}{D_{50}} \tag{17}$$

$$k_\infty = 3.7\frac{(1-n)}{\sqrt{n}}\sum_i u_i^2 \tag{18}$$

where $\sigma_k, \sigma_\epsilon, C_{1\epsilon}, C_{2\epsilon}$, and C_μ are empirical coefficients (Rodi, 1987).

$$\sigma_k = 1.0, \quad \sigma_\epsilon = 1.3, \quad C_{1\epsilon} = 1.44, \quad C_{2\epsilon} = 1.92, \quad C_\mu = 0.09 \tag{19}$$

P_s is the shear production, calculated as

$$P_s = -\overline{u_i' u_j'}\frac{\partial u_i^*}{\partial x_j^*} \tag{20}$$

where Reynolds stress $\overline{u_i' u_j'}$ is calculated by a nonlinear model proposed by (Lin & Liu, 1998a, 1998b), modified by (Hsu et al., 2002) for porous media flow, and further modified to include porosity inside the derivatives as follows

$$\begin{aligned}\overline{u_i' u_j'} = &-C_d\frac{k^2}{n\epsilon}\left(\frac{\partial u_i^*}{\partial x_j^*}+\frac{\partial u_j^*}{\partial x_i^*}\right)+\frac{2}{3}\frac{k}{n}\delta_{ij}\\ &-C_1\frac{k^3}{n\epsilon^2}\left(\frac{\partial u_i^*}{\partial x_l^*}\frac{\partial u_l^*}{\partial x_j^*}+\frac{\partial u_j^*}{\partial x_l^*}\frac{\partial u_l^*}{\partial x_i^*}-\frac{2}{3}\frac{\partial u_l^*}{\partial x_k^*}\frac{\partial u_k^*}{\partial x_l^*}\delta_{ij}\right)\\ &-C_2\frac{k^3}{n\epsilon^2}\left(\frac{\partial u_i^*}{\partial x_k^*}\frac{\partial u_j^*}{\partial x_k^*}-\frac{1}{3}\frac{\partial u_l^*}{\partial x_k^*}\frac{\partial u_l^*}{\partial x_k^*}\delta_{ij}\right)\\ &-C_3\frac{k^3}{n\epsilon^2}\left(\frac{\partial u_k^*}{\partial x_i^*}\frac{\partial u_k^*}{\partial x_j^*}-\frac{1}{3}\frac{\partial u_l^*}{\partial x_k^*}\frac{\partial u_l^*}{\partial x_k^*}\delta_{ij}\right)\end{aligned} \tag{21}$$

where C_d, C_1, C_2, and C_3 are empirical coefficients given by (Lin & Liu, 1998a, 1998b).

$$C_d = \frac{2}{3}\left(\frac{1}{7.4 + 2S_{max}}\right), \quad C_1 = \frac{1}{185.2 + 3D_{max}^2}$$
$$C_2 = \frac{1}{58.5 + 2D_{max}^2}, \quad C_3 = \frac{1}{370.4 + 3D_{max}^2} \tag{22}$$

with

$$S_{max} = \frac{k}{\epsilon}\max\left\{\left|\frac{\partial u_i^*}{\partial x_i^*}\right| \text{ (indices not summed)}\right\}$$
$$D_{max} = \frac{k}{\epsilon}\max\left\{\left|\frac{\partial u_i^*}{\partial x_j^*}\right|\right\} \tag{23}$$

P_v is the turbulence production due to vegetation, calculated as

$$P_v = u_i f_{vi} = \frac{1}{2} C_D \lambda |\boldsymbol{u}|^3 \tag{24}$$

4.1.3 Numerical Method

The numerical method follows the framework of the original NHWAVE model (Ma et al., 2012) using a combined finite-volume and finite-difference method. The fluxes at cell faces are estimated using a shock-capturing HLL TVD scheme to discretize momentum equations. The convective fluxes in the k- ε equations are determined by the hybrid linear/parabolic approximation (HLPA) scheme (Zhu, 1991), which has second order accuracy in space. The second order temporal accuracy in time stepping is obtained by using the two-stage second-order nonlinear Strong Stability-Preserving (SSP) Runge-Kutta scheme (Gottlieb et al., 2001). Advection and horizontal diffusion terms are treated explicitly, and the vertical diffusion is discretized implicitly. The system is solved using the high performance preconditioner HYPRE software library and the model is fully parallelized using the Message Passing Interface (MPI) with non-blocking communication.

Boundary conditions are required for all physical boundaries to solve the equations. The free surface is given by,

$$\left.\frac{\partial u}{\partial \sigma}\right|_{\sigma=1} = \left.\frac{\partial v}{\partial \sigma}\right|_{\sigma=1} = 0, \qquad \left.\frac{w}{n}\right|_{\sigma=1} = \frac{\partial \eta}{\partial t} + \frac{u}{n}\frac{\partial \eta}{\partial x} + \frac{v}{n}\frac{\partial \eta}{\partial y} \tag{25}$$

Dynamic pressure at the surface is zero. For the $k-\varepsilon$ model, zero gradients of k and ε are imposed.

$$\left.\frac{\partial k}{\partial \sigma}\right|_{\sigma=1} = \left.\frac{\partial \epsilon}{\partial \sigma}\right|_{\sigma=1} = 0 \tag{26}$$

The normal velocity and tangential stress are prescribed at the bottom and the normal velocity is imposed through the kinematic boundary condition.

$$\left.\frac{w}{n}\right|_{\sigma=0} = -\frac{u}{n}\frac{\partial h}{\partial x} - \frac{v}{n}\frac{\partial h}{\partial y} \tag{27}$$

Bottom shear stresses are considered for the horizontal velocities.

$$\nu_t \left.\frac{\partial u}{\partial \sigma}\right|_{\sigma=0} = DC_b|\boldsymbol{u}_b|\boldsymbol{u}_b \tag{28}$$

where C_b is the bed drag coefficient, computed as $C_b = 0.16[\ln(15\Delta z_1/k_s)]^{-2}$, $\Delta z_1 = D\Delta\sigma_1$ is the thickness of the cell above the bed, k_s is the bottom roughness height, and $\boldsymbol{u}_b$ is the velocity at the cell above the bed. Boundary conditions for k and ε become

$$k_b = \frac{u_*^2}{\sqrt{C_\mu}} \qquad \epsilon_b = \frac{u_*^3}{\kappa z} \tag{29}$$

where $u_* = \kappa|\boldsymbol{u}_b|/[\ln(15\Delta z_1/k_s)]$ is the friction velocity and $\kappa = 0.41$ is the von Karman constant.

4.2 Model Setup

The numerical model is calibrated and validated with data collected from the Captain Sinclair living shoreline project during the field data collection discussed in Chapter 3. Topographic and bathymetric data collected from the field study site are used to create the model elevation file as shown in Figure 43. The model boundaries are 920 m in the cross-shore x-

direction and 480 m in the alongshore y-direction with a grid spacing of 0.1 m in the x and y directions.

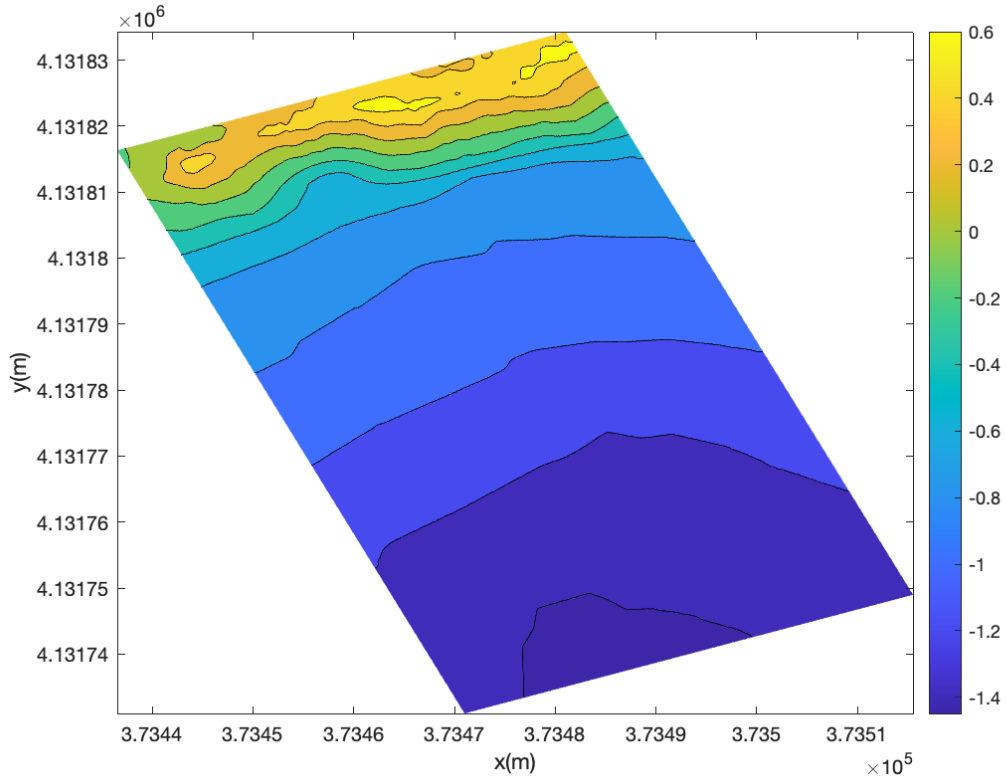

Figure 43: Model elevation map generated from data collected at Captain Sinclair Recreational Area

The offshore gauge spectrum was used for wave forcing in the model. As discussed in the previous chapter, three events were selected for use in calibrating and validating the model. Due to computational expense when running simulations, an event of a few minutes, rather than hours and days, is used in this numerical modeling assessment. The events selected in the previous

chapter ranged from 1.2 hours in duration to 32.4 hours in duration. Since attenuation of wave energy is the focus of this study, a data set of 400 seconds where the largest significant wave heights at the offshore gauge occurred during each event were extracted for the model calibration and validation analysis. These wave heights were all from the sea wave band of waves and not boat wake influenced waves. The location of the gauges is shown in Figure 44, the gauge spectrums used for calibration are shown in Figure 45, and the corresponding wave characteristics are shown in Table 3. Interestingly, the shapes of the spectra from Events 1 and 3 differ when the smaller portion of analysis is extracted than the spectra from the full event. Event 1 had a full event spectrum with a much higher magnitude lower frequency peak, but the 400 second subset with the highest wave heights from this event has a double peak spectrum with similar magnitude for the two peaks. Event 3 had a double peak spectrum with equal magnitude for both peaks and a wide sea wave band, but it is showing a single wide peak for the 400 second subset with the highest wave energy from this event. Event 2 has a similar single peak spectrum for the 400 second subset as compared to the full event, but this smaller period of analysis has a higher magnitude, as would be expected since it is the period of highest wave heights for the event.

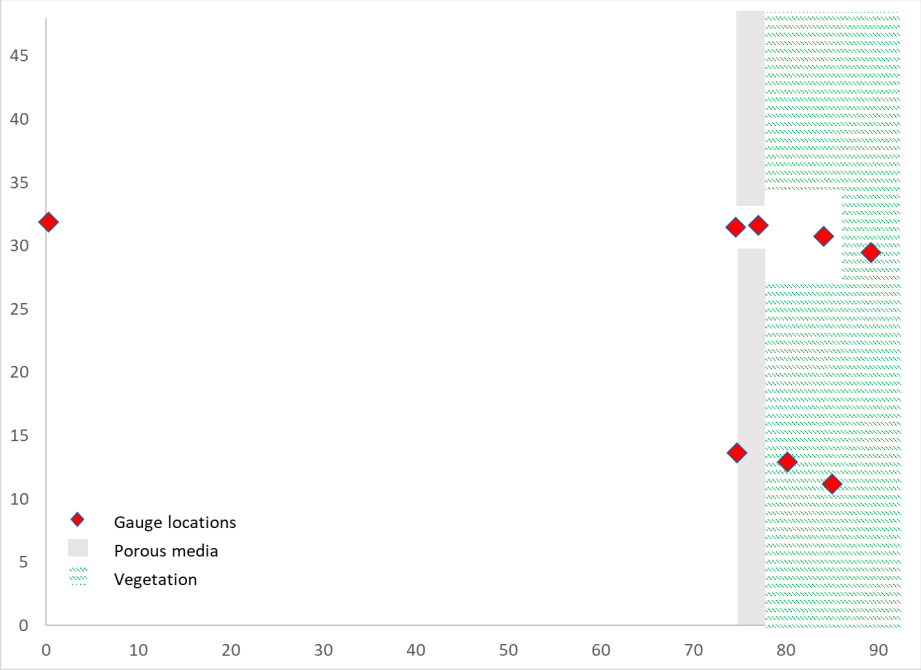

Figure 44: Location of gauges in the model setup

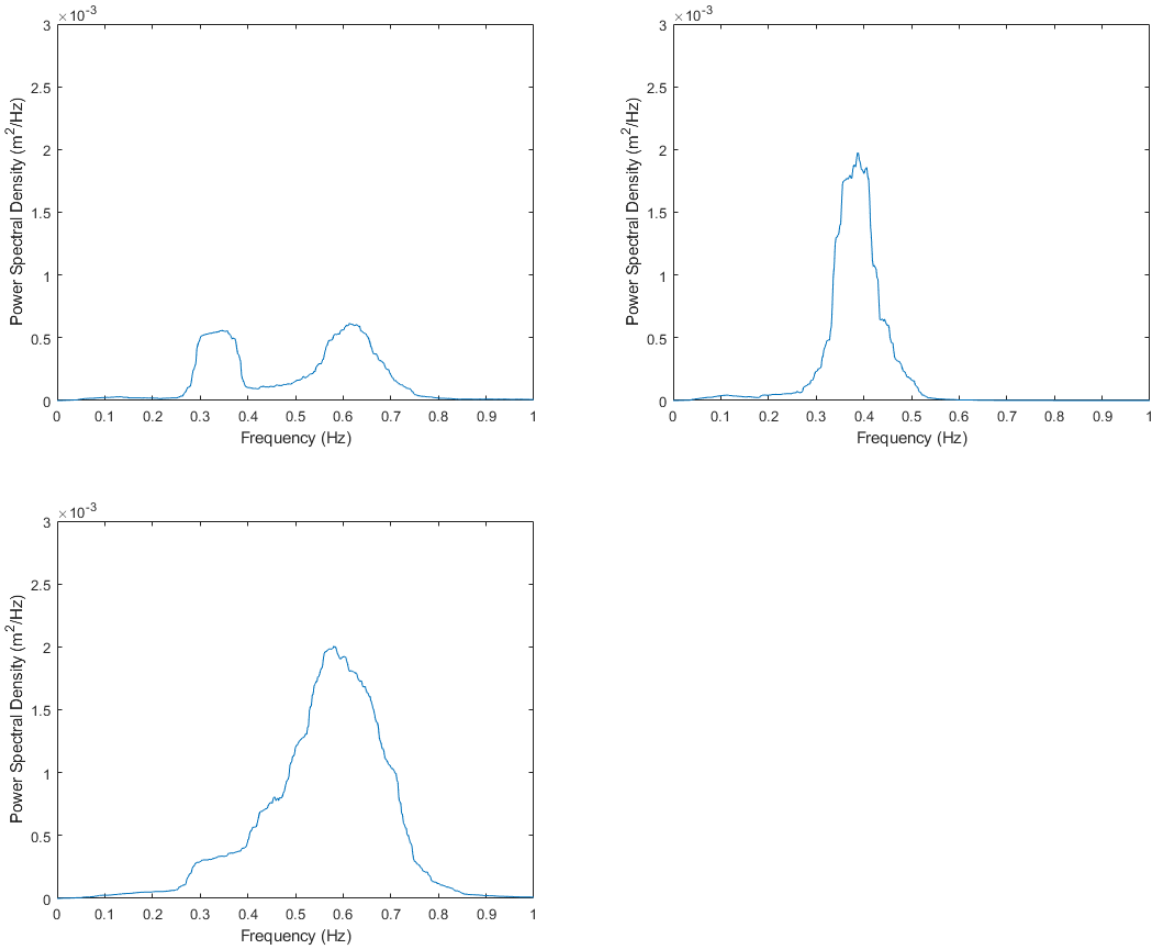

Figure 45: Offshore field gauge data spectrums from the three events, a) Event 1, b) Event 2, c) Event 3

Table 3: Wave Characteristics for the Calibration and Validation Simulations

	Hs (m)	Ts (s)	Hm0 (m)	Tp (s)	Depth (m)
Event 1	0.06	3.6	0.05	3.4	2.0
Event 2	0.07	3.5	0.06	3.0	2.0
Event 3	0.10	2.8	0.09	1.9	1.9

The modified NHWAVE models allow for porous media and vegetation modules to be utilized in assessment of the nearshore environment. In this study, both modules were used to incorporate the rock sills and marsh vegetation at the field study site. A D50 of 0.49 m is used to model the rock sill constructed at Captain Sinclair based on the original design and construction data available (Milligan et al., 2016). The Captain Sinclair shoreline is an active study site for a variety of researchers and vegetation characteristics for the project site were collected in September 2018 (Nunez et al., 2021), three months prior to the December 2018 deployment in this study. The low marsh *Spartina alterniflora*, where the study gauges were located, had an average vegetation height of 141 cm and a density of 125/m2. The model currently allows the use of either no vegetation or rigid vegetation, with the option for flexible vegetation still under development.

The next sections discuss the calibration and validation periods and the results of the alternatives analyses.

4.3 Calibration and Validation Results

It is important to determine the correct parameters for the model simulations prior to conducting alternative analyses to predict the outcome of the shoreline erosion project under other than existing conditions. As such, the field data collected at Captain Sinclair, and discussed in Chapter 3, was used to calibrate the model to the conditions at this specific site. The parameters of the model that are calibrated include the α and β coefficients for the porous media shown in equations 4 and 5, respectively, and the vegetation drag coefficient, C_D, shown in equation 7. The model was calibrated and validated with conditions that represented the highest water levels and wave heights that occurred during the deployment.

The model simulations are run for 500 seconds so that the first 100 seconds of the simulation can be discarded to reduce the noise that occurs while the model builds to fully developed conditions. This length of simulation provides a large enough wave sample at this site, at least 100 waves, for appropriate analysis. The wave energy spectrum is then calculated for the remaining 400 seconds of the simulation and compared to the wave energy spectrum of the 400 seconds extracted from the field data for concurrence.

As mentioned in Chapter 3, the seaward gauge was located within one meter of the structure and the wave energy spectrum calculated from the gauge data show the effect of wave reflection off the structure for the full deployment analysis. As shown in Figure 46, which includes a comparison to both the seaward and offshore gauges, the model had difficulty capturing all of these hydrodynamic actions so close to the structure. The model also had difficulty simulating the double peaked spectrum of Event 1. Since this event had almost negligible wave energy at the marsh gauge, as shown in Figure 47, it was determined that Event 2 and Event 3 would be used to calibrate and validate the model for the alternatives analysis. Despite the difficulty in predicting the behavior of the wave energy adjacent to the structures, the model was able to calibrate reasonably with the field data at the landward and marsh gauge locations as shown in the calibration and validation simulation results in Figure 48 and Figure 49. An item to note is that the marsh gauge wave spectrum shifted the peak lower at Event 3 than the gauge results, but the magnitude of the peak was comparable. The focus of this study is to determine the effect of the structure and the vegetation of a living shoreline system on the wave energy, so the remaining analyses will focus on how wave energy will change at these two locations under different scenarios.

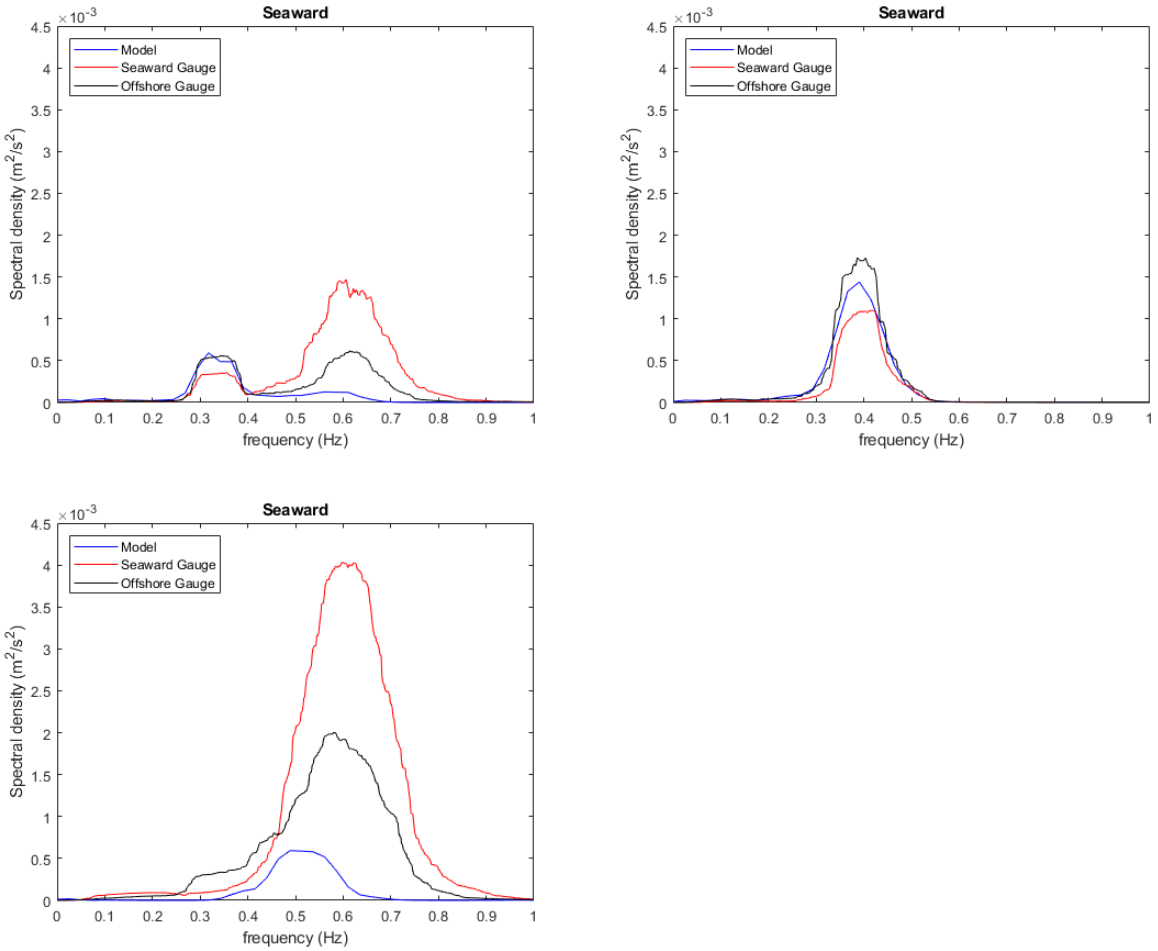

Figure 46: Calibration and validation model results at the seaward gauge location

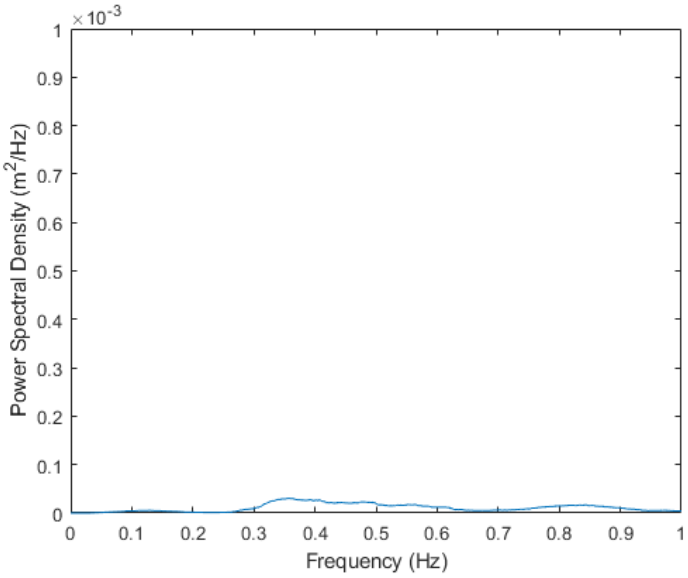

Figure 47: Event 1 wave spectrum at the marsh gauge

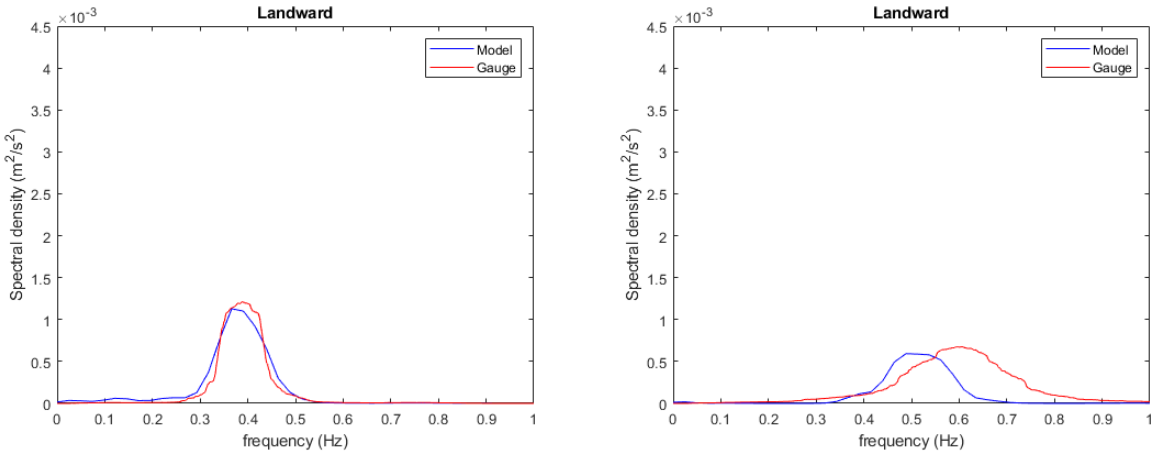

Figure 48: Calibration and validation model results at the landward gauge location

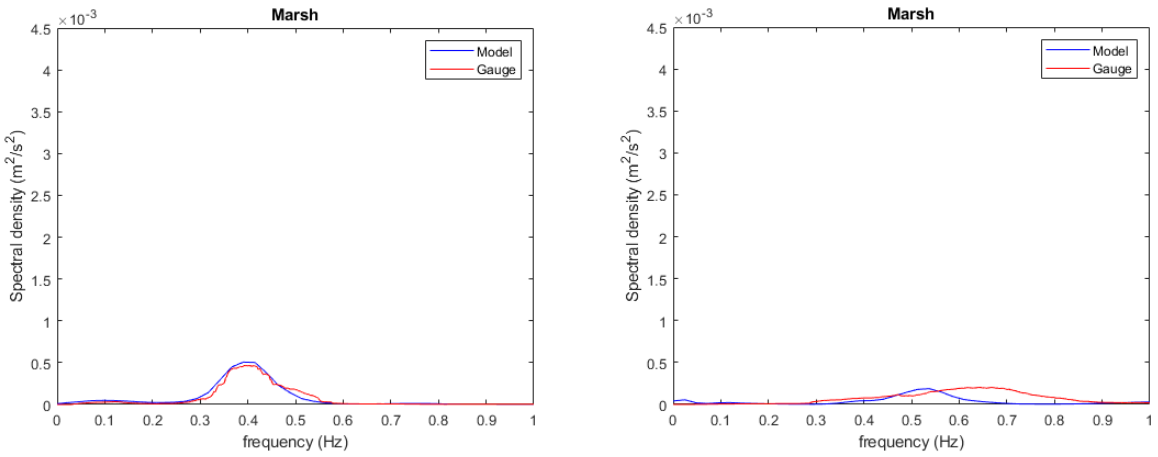

Figure 49: Calibration and validation simulations at the marsh gauge location

The NHWAVE input file for the calibration simulation in this section is provided in Appendix B.

4.4 Alternatives Analyses

The alternative analysis portion of the study looked at two different objectives. The first is observing the functionality of the existing site if the structure crest height were lowered to accommodate more land-water interaction across the crest of the structure. The second is observing how conditions change with increased water levels to mimic potential sea level rise scenarios. These analyses were conducted using the spectrum from Event 2 to force the model and changing the crest height of the structure and water levels at the site as described in the next sections.

4.4.1 Existing Conditions – Lower Crest Elevation

The crest height of the structure has been set at the elevation of the eroding scarp at the marsh prior to project construction. This has been shown to be a beneficial elevation for erosion control structures along marshes (Leonardi et al., 2016; McLoughlin et al., 2015; Wiberg et al.,

2019). However, in seeking ways to optimize the marsh sill design for overall structural and habitat success, this study looks at the effects of lowering the structure crest elevation and determining the ability of the whole system – both structure and vegetation – to attenuate wave energy. Two different crest elevation scenarios were modeled, one with the crest elevation at mean high water (0.92 m) and the second with a 25% reduction in current height above the bed (0.82 m). While the crest height was reduced in the first two alternatives, the vegetation was also removed from the portion of shoreline where it was added in the project construction to simulate the conditions immediately after construction to not yet incorporate established vegetation in that area that serves to attenuate wave energy, as depicted in Figure 50. Since a living shoreline project will not initially have fully developed vegetation to provide attenuation, these simulations, shown in Figure 51, demonstrate how the structure affects wave energy attenuation and what that can mean to establishing the newly planted marsh edge. The next two alternatives in this section, shown in Figure 52, simulate the two decreased crest elevations coupled with the fully established vegetation present at the site. These represent the optimum wave attenuation conditions for the system. Modeling the two decreased crest elevations in this manner allows for the observation of the full range of capability of the living shoreline system.

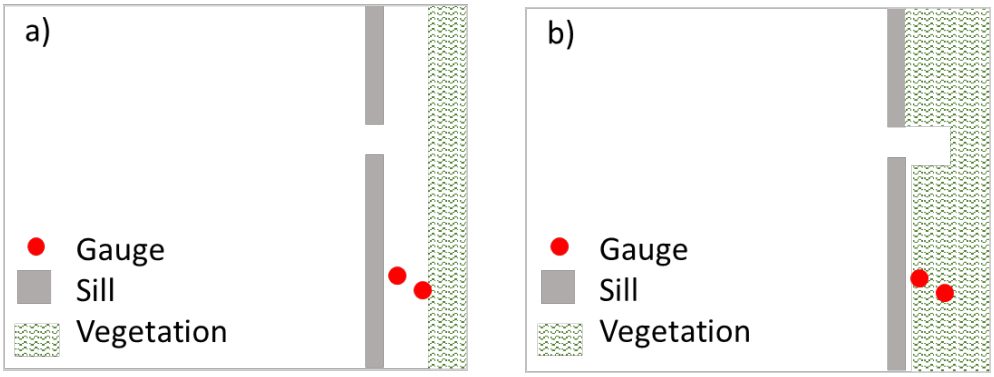

Figure 50: Model setup for Alternatives 1 and 2 (a) and Alternative 3 and 4 (b)

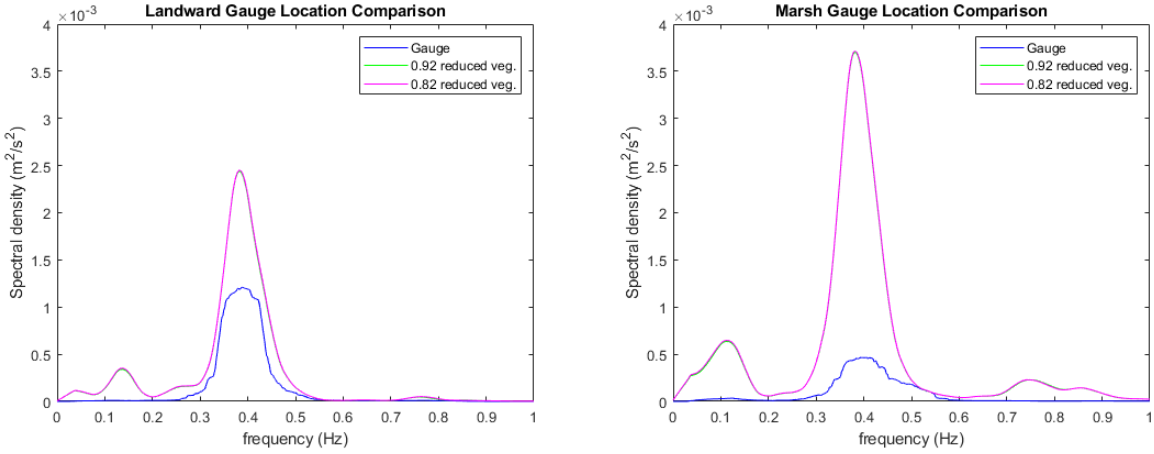

Figure 51: Alternatives 1 and 2 with reduced crest height and reduced vegetation

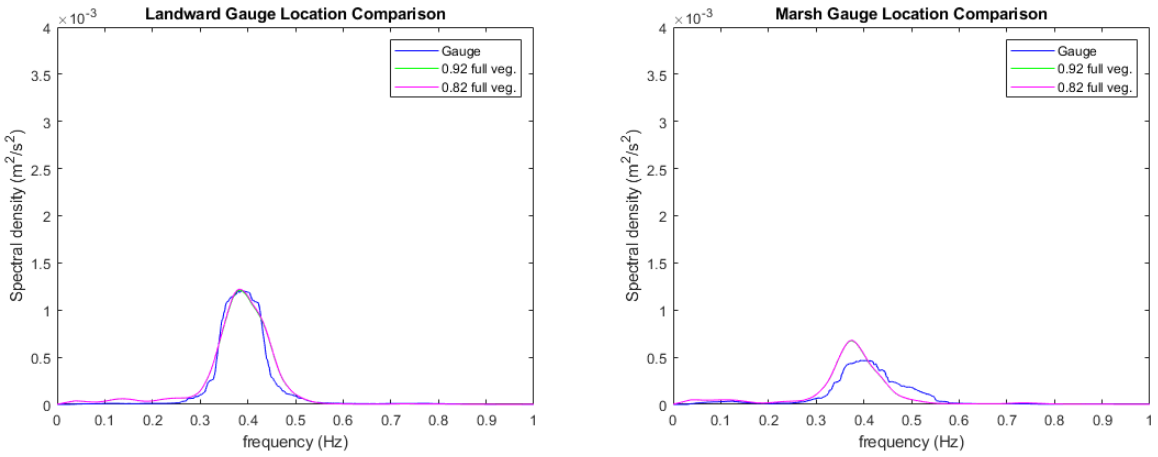

Figure 52: Alternative 3 and 4 with reduced crest elevations and fully developed vegetation

As shown in these figures, there is no discernable difference between the spectra at the two different crest heights. However, there is considerable difference between the simulations with partial vegetation and those with fully developed vegetation. Further analysis of these simulations, as shown in Figure 53 to Figure 56, reveal that the simulations with the reduced vegetation conditions (Alternative 1 and Alternative 2), representing immediate post-construction conditions, have increased wave energy from 22% to 67% at the landward gauge location and 27% to 89% at the marsh gauge location between the main frequency band of 0.3 to 0.5 Hz. The vegetation at Captain Sinclair extends to the structure and appears to be providing considerable wave attenuation services in the approximately one-meter distance from the structure where the landward gauge was located as is seen when comparing the wave spectrum from Alternative 1 to Alternative 3 (Figure 53). Alternative 3 and Alternative 4 have the fully developed vegetation characteristics as were the conditions during the study deployment period. The marsh gauges for Alternatives 3 and 4 do show a slight increase in the wave energy spectra, but there is a noticeable difference in the amount of wave energy attenuation that is provided by

the vegetation when comparing the marsh gauge locations of the partially vegetated conditions to the fully vegetation conditions.

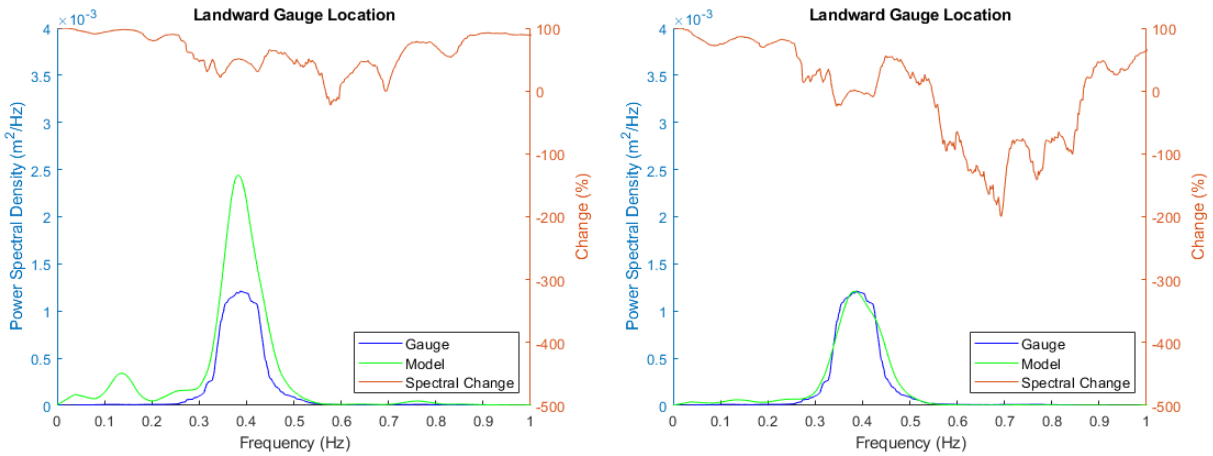

Figure 53: Simulation results at the landward gauge for the structure crest height at 0.92 m, Alternative 1 with reduced vegetation (left) and Alternative 3 with full vegetation (right)

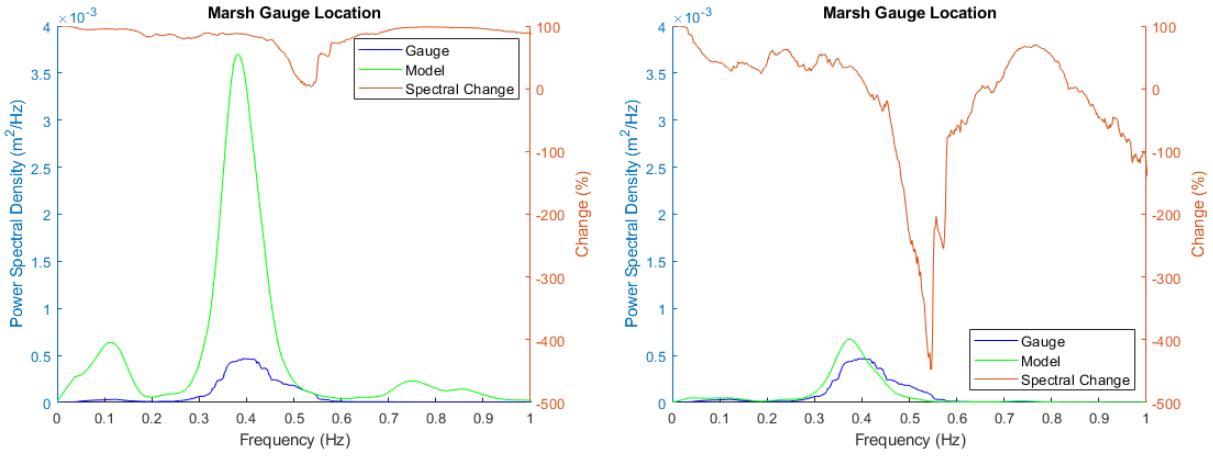

Figure 54: Simulation results at the marsh gauge for the structure crest height at 0.92 m, Alternative 1 with reduced vegetation (left) and Alternative 3 with full vegetation (right)

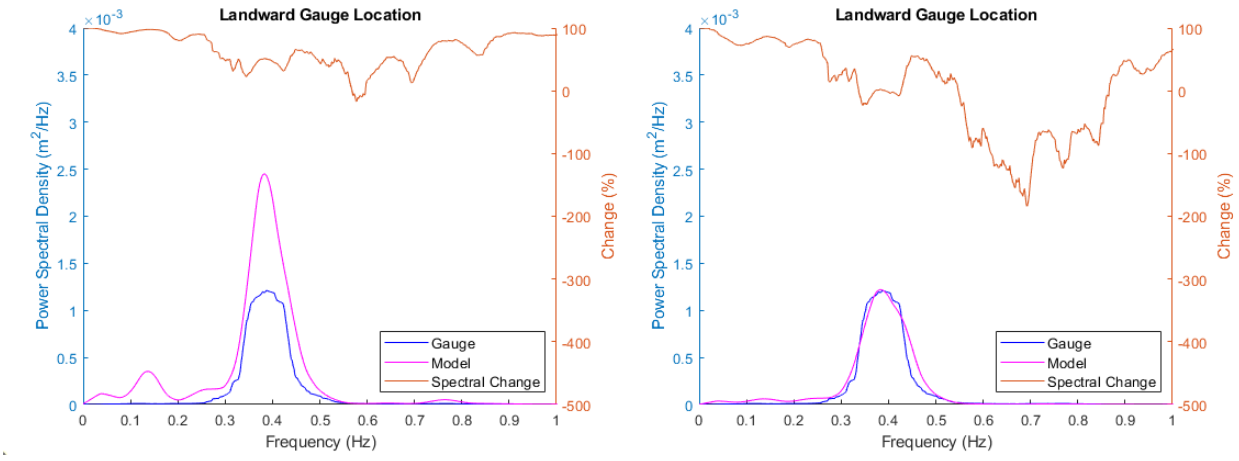

Figure 55: Simulation results at the landward gauge for the structure crest height at 0.82 m, Alternative 2 with reduced vegetation (left) and Alternative 4 with full vegetation (right)

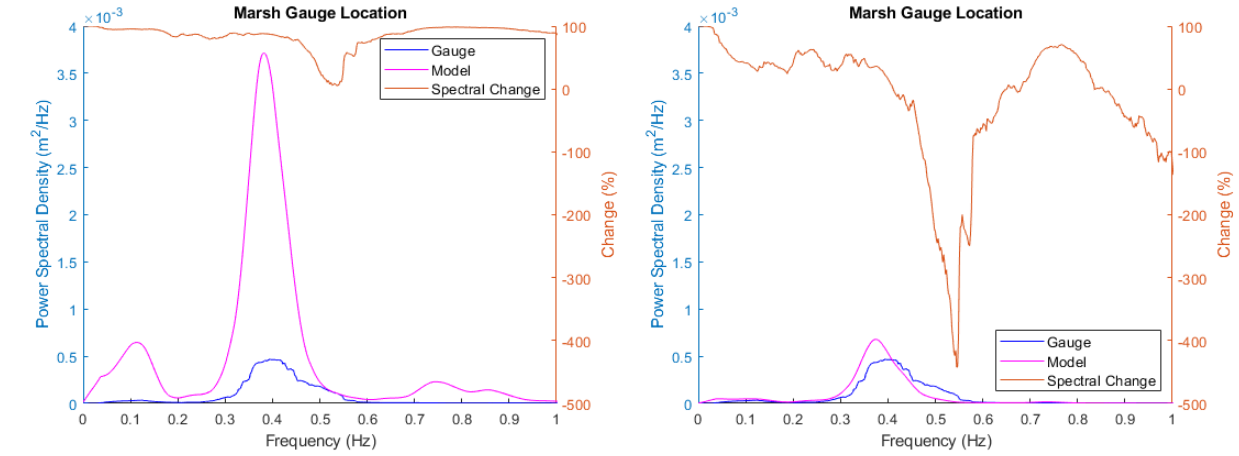

Figure 56: Simulation results at the marsh gauge for the structure crest height at 0.82 m, Alternative 2 with reduced vegetation (left) and Alternative 4 with full vegetation (right)

4.4.2 Future Conditions – Increased water level

While the previous section explored the possibility of optimizing the current design, this section of analysis explores how adaptable a living shoreline design may be to various potential

sea level rise scenarios. Sea level rise (SLR) at the Captain Sinclair site is currently estimated at 4.93 mm/yr (tidesandcurrents.com, Station 8637689, April 2022). Considering the design life of a typical coastal armoring structure, three different potential future scenarios were simulated to increase the existing water level to the 10-, 20-, and 30-year sea level rise conditions. An item to note is that this study is reflective of a linear application of the SLR rate at the 10-,20-, and 30-year levels which may not be the correct time frames if SLR accelerates at this site. Additionally, the assumption is the marsh will be able to adapt to increased water levels and continue to survive. While is it often recognized that increased water levels, specifically due to climate change, will lead to increased wave heights, there is no easy way to predict the exact amount of increase in wave height. In some cases, studies have revealed that wave heights at some locations may decrease as sea levels rise (Melet et al., 2020). Since exploring the change in wave height as sea levels rise is outside the realm of this study, a conservative approach of keeping the same wave spectra and characteristics to force the model from the calibration run was used in this analysis. In this manner the simulations are showing specifically how the change in water level due to sea level rise will affect the capacity of the system to attenuate wave energy and adapt to potential sea level rise scenarios. Figure 57 and Figure 58 show the results of the three sea level rise scenarios compared to the existing conditions at Captain Sinclair while Table 4 shows the percent increase in wave height for each alternative.

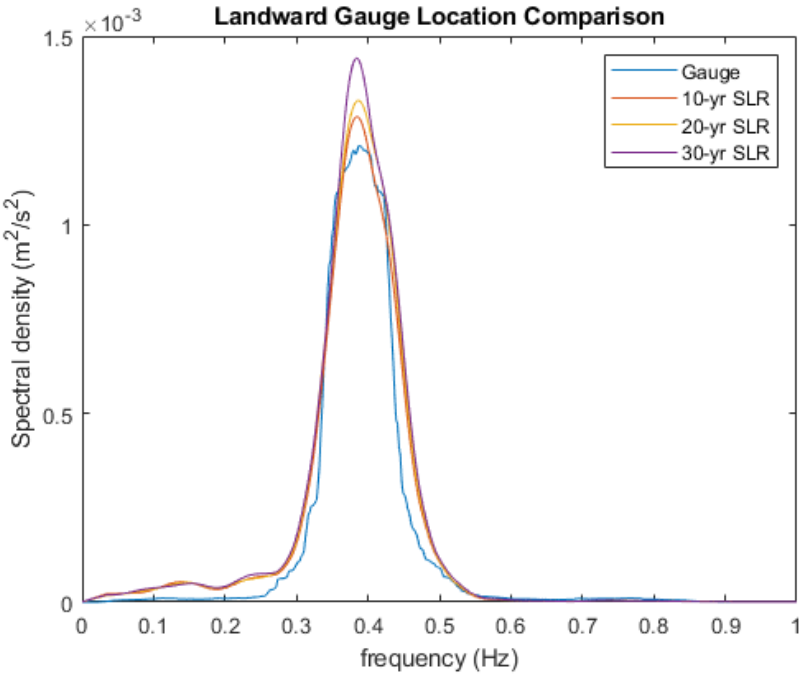

Figure 57: Comparison of deployment conditions and sea level rise scenarios at the landward gauge

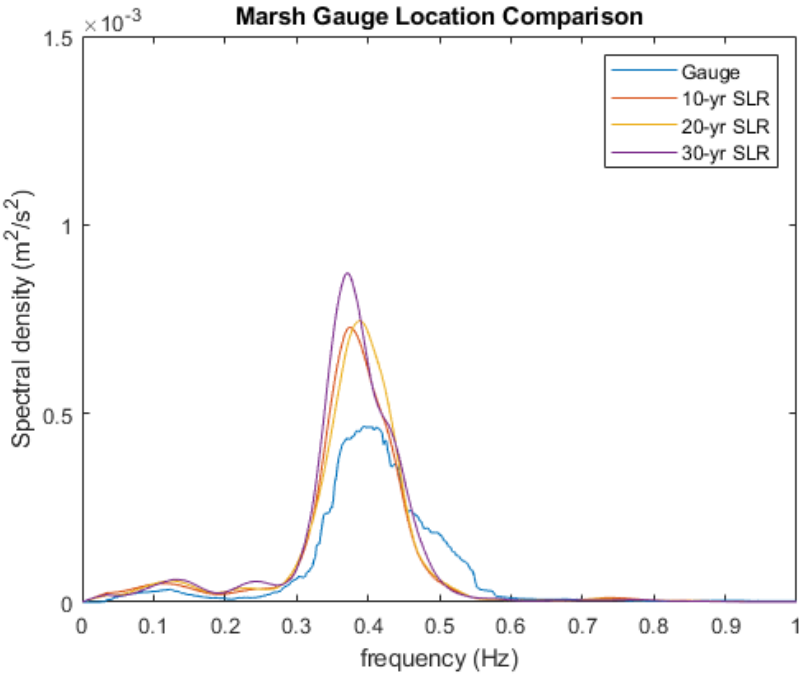

Figure 58: Comparison of deployment conditions and SLR scenarios at the marsh gauge

Table 4: Wave Height Percentage Increase for SLR Scenarios

Increased water level	Landward Gauge Location	Marsh Gauge Location
10-Year SLR	4%	9%
20-Year SLR	6%	11%
30-Year SLR	8%	17%

The next three figures focus more specifically on the percent change in the spectrums at the two gauge locations for each SLR scenario. In Figure 59 it is shown that the wave energy at the landward gauge for the 10-year SLR conditions increases 0% to 57% in the sea band range of 0.3 to 0.5 Hz. For the marsh location the model did not quite capture the spectrum between 0.45

and 0.5 Hz as well as the gauge, so the observations are limited to the 0.3 to 0.45 range and show an increase in wave energy of 0% to 52%. The 20-year SLR scenarios are shown in Figure 60 and reveal that the wave energy at the landward gauge increases 0% to 60% and at the marsh gauge increases 12% to 52%. As expected for the 30-year SLR scenarios shown in Figure 61, the wave energy is increased the most at 0% to 62% for landward gauge and 12% to 60% for the marsh gauge.

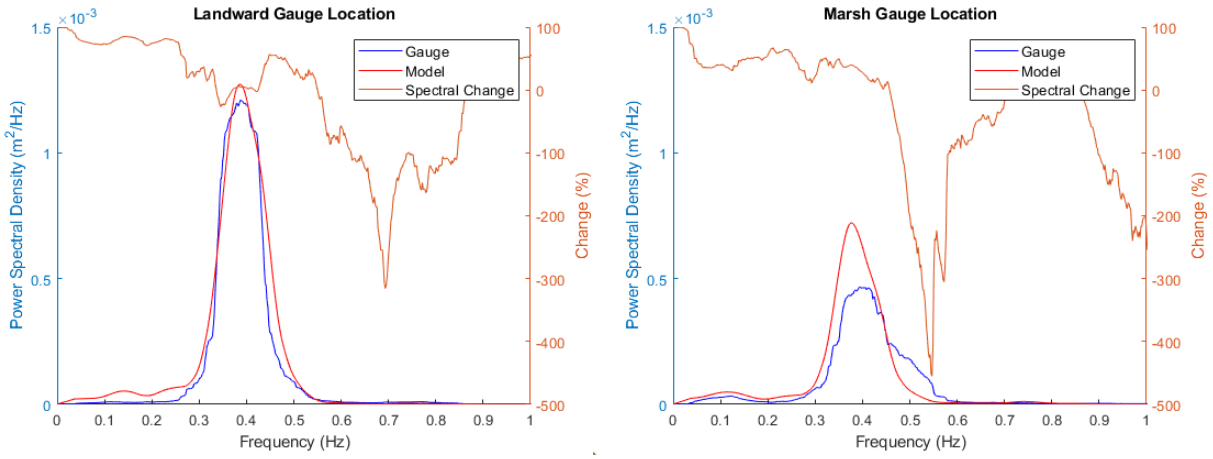

Figure 59: Changes in wave spectrum for the 10-year SLR scenario

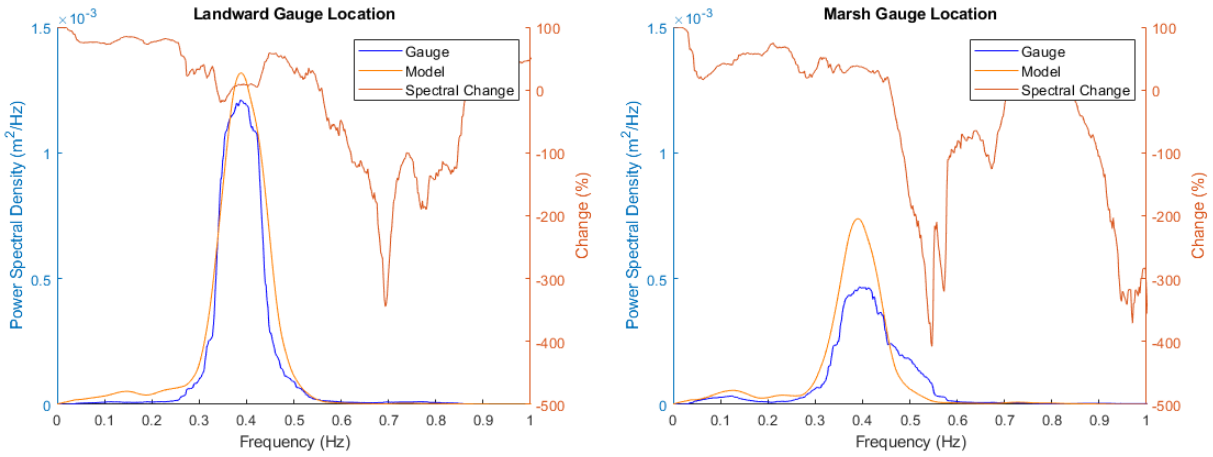

Figure 60: Changes in wave spectrum for the 20-year SLR scenario

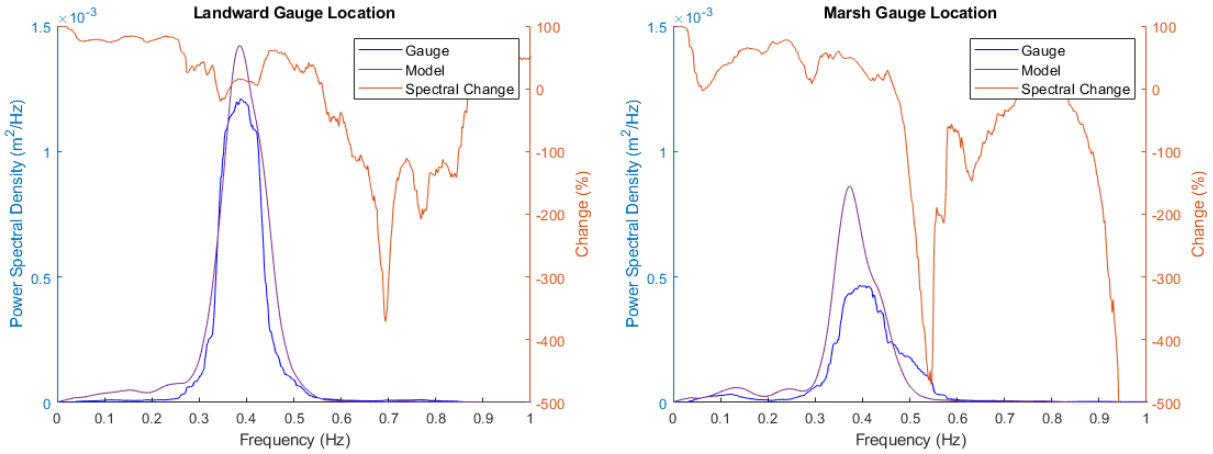

Figure 61: Changes in wave spectrum for the 30-year SLR scenario

4.5 Discussion & Conclusions

The NHWAVE model was calibrated and validated with the field data collected at Captain Sinclair to simulate potential opportunities for reducing the structure footprint and increasing land-water connectivity with the marsh. While the model shows good calibration results at the

landward and marsh gauge locations, the location of the seaward gauge in the field study captured wave reflection off the sill structure and the model is unable to fully capture all aspects of the dynamic wave environment at this location. Further study of the model with multiple sensors between the offshore gauge and the seaward gauge would be interesting to see how well shoaling is incorporated at this site when structure interference (in the form of wave reflection) is not impacting the model simulation results.

Based on the results of the model simulations looking at the reduced crest height scenarios, it is shown that the presence of vegetation has a more significant impact on the ability of the living shoreline system to attenuate wave energy between the landward and marsh gauges than the structure alone. The simulations do not show a noticeable difference in wave attenuation services with the crest elevation reduced by up to 25% at the alternatives with fully vegetated conditions. However, the two alternatives that have reduced vegetation to simulate immediate post-construction conditions have increased wave energy ranging from 22% to 67% at the landward gauge location and 27% to 89% at the marsh gauge. These simulations clearly show the contributions of vegetation on the overall living shoreline system and the room for potentially decreasing the structure height to accommodate more land-water interaction. However, as the much higher wave energy that occurred at the marsh gauge locations in the alternatives with partial vegetation show, the structure needs to be sufficient to attenuate enough wave energy to allow the marsh vegetation to successfully grow to provide these further wave attenuation services.

The second set of alternatives studied observed the other side of the crest elevation question with how adaptable the living shoreline might be to SLR. The results of three SLR scenarios, 10-year, 20-year, and 30-year, conditions at the Captain Sinclair site reveal that the

erosion protection project should continue to provide wave attenuation services over the next 30-year life of the project, considering current well-established vegetation conditions. The most extreme 30-year SLR conditions show an increase of 0% to 62% in wave energy for the landward gauge location and 12% to 60% for the marsh gauge location. The highest of these changes is observed at the peak frequency.

Utilizing the NHWAVE model to simulate potential scenarios at the Captain Sinclair living shoreline provided insight into how this system may react with a reduced crest elevation and the ability of the system to adapt to SLR. Properly calibrating the model with site conditions was necessary to return reliable results to the study questions and reinforces the importance of collecting field data when design living shoreline erosion protection projects. Since this is the first time NHWAVE has been used to evaluate a living shoreline project, it would be interesting to obtain field data from additional living shoreline sites to determine an appropriate range of values for the α, β, and C_D parameters to be able to comfortably utilize this model at a project site that does not have data available for calibration in the future.

CHAPTER

5 CONCLUSIONS

This study examines the efficacy of the Captain Sinclair Recreational Area marsh-sill living shoreline project in Virginia and uses field data collected at the site to examine three questions related to the attenuation properties of a marsh sill living shoreline. The study analyzed field data across two profiles at the project site, one across the structure and the other across the gap between structures, to provide observations regarding the influence of the structure and the influence of the vegetation on the erosion protection system. These data are then utilized for further research using numerical methods. The study showed that the structure profile of the marsh sill design was quite effective at attenuating wave energy across the spectrum, with some frequencies better attenuated than other frequencies. Specifically, there was more attenuation in the sea wave band, which was the focus of this study, and the lower frequency wave energy, likely from boat wakes, was not attenuated as effectively as the sea waves. Interestingly, while not an initial focus of the study, the analysis of field data revealed that the gap profile was able to provide some attenuation services related to the structure, likely due to diffraction. The results of the numerical portion of the study revealed that NHWAVE was able to calibrate well with the landward and marsh gauges from the field study and show that the vegetation portion of the living shoreline design has a greater impact on wave energy attenuation than the crest height of the structure when the latter is reduced in elevation. The numerical modeling assessment also showed the capacity of the living shoreline to adapt to potential sea level rise scenarios for the next 30 years and still provide considerable wave attenuation services. Assessing the adaptation potential for this type of shoreline erosion protection is vital to informing guidance on how best

to utilize a living shoreline erosion protection design when assessing armored shoreline options and landward retreat options in the face of sea level rise.

5.1 Research Objectives Conclusions

The specific questions for the study were addressed as follows:

1. How quantitatively effective is a marsh sill living shoreline at attenuating wave energy?

The results of this assessment are able to quantify that a structure can help attenuate wave energy enough to prevent marsh edge erosion and then allow the marsh vegetation to do its part in wave energy attenuation as a key part of the overall erosion protection system. The attenuation of wave energy due to the structure on the structure profile ranges from 56% to 96%, depending on the frequency, and the marsh vegetation between the landward and marsh gauges of the structure profile attenuated wave energy from 0% to 67%. The gap profile revealed wave energy attenuation from 66% to 73% between the seaward and landward gauges and 25% to 80% between the landward and marsh gauges, without the attenuation in the sea wave band that is apparent in the structure profile.

2. How does reducing the crest height to decrease the structure footprint and increase land and water connectivity affect the overall wave attenuation properties of the living shoreline system?

Based on the results of the model simulations looking at the reduced crest height scenarios, it is shown that the presence of vegetation has a more significant impact on the ability of the living shoreline system to attenuate wave energy between the landward and marsh gauges than the structure alone. The simulations do not show a noticeable difference in wave attenuation services with the crest elevation reduced by up to 25% at the alternatives with fully vegetated conditions. However, the two alternatives that have reduced vegetation to simulate immediate

post-construction conditions have increased wave energy ranging from 22% to 67% at the landward gauge location and 27% to 89% at the marsh gauge. These simulations clearly show the contributions of vegetation on the overall living shoreline system and the room for potentially decreasing the structure height to accommodate more land-water interaction.

3. How do the overall attenuation properties of a living shoreline change as sea level rise increases and what is the potential adaptation capacity for the design life of the project?

The results of three SLR scenarios, 10-year, 20-year, and 30-year, conditions at the Captain Sinclair site reveal that the erosion protection project should continue to provide wave attenuation services over the next 30-year life of the project, considering current well-established vegetation conditions. The most extreme 30-year SLR conditions show an increase of 0% to 62% in wave energy for the landward gauge location and 12% to 60% for the marsh gauge location. The highest of these changes is observed at the peak frequency.

5.2 Contributions and Limitations

The study quantified the attenuation properties of the structure and the vegetation components of a marsh sill living shoreline system and showed the effectiveness of using NHWAVE to examine alternative design options. Through the combination of both of these types of assessments, the study was able to show ways to optimize structure design and the adaptability of these types of shoreline erosion protection designs. As with many research studies undertaken, limitations are revealed during analysis and observations. The numerical model was able to calibrate well with the single peaked wave spectrum events extracted for analysis; however, the double peaked wave spectrum was not well simulated. This can be a limiting factor if predicting the response of a system to two significant wave energy drivers, e.g., wind and boat wakes, is desired. The model was also unable to properly capture all the facets of the dynamic

wave environment that were present at the seaward gauge, with its location within one-meter of the rock sills structure. Having a gauge located farther from the structure, where the influence of wave reflection is not significant, would be interesting to see how well the model simulates the shoaling that occurs at this site and would be a useful study for future research.

REFERENCES

Barbier, E. B., Hacker, S. D., Kennedy, C., Koch, E. W., Stier, A. C., & Silliman, B. R. (2011). The value of estuarine and coastal ecosystem services. *Ecological Monographs*, *81*(2), 169–193. https://doi.org/10.1890/10-1510.1

Bilkovic, D. M., Mitchell, M., Mason, P., & Duhring, K. (2016). The Role of Living Shorelines as Estuarine Habitat Conservation Strategies. *Coastal Management*, *44*(3), 161–174. https://doi.org/10.1080/08920753.2016.1160201

Blair, S., Adams, C., Ankersen, T., McGuire, M., & Kaplan, D. (2018). *Ecosystem Services Valuation for Estuarine and Coastal Restoration in Florida* (TP-204; p. 7). Florida Sea Grant Program, UF/IFAS Extension. https://edis.ifas.ufl.edu/publication/SG134

Borsje, B. W., van Wesenbeeck, B. K., Dekker, F., Paalvast, P., Bouma, T. J., van Katwijk, M. M., & de Vries, M. B. (2011). How ecological engineering can serve in coastal protection. *Ecological Engineering*, *37*(2), 113–122. https://doi.org/10.1016/j.ecoleng.2010.11.027

Bouma, T. J., van Belzen, J., Balke, T., Zhu, Z., Airoldi, L., Blight, A. J., Davies, A. J., Galvan, C., Hawkins, S. J., Hoggart, S. P. G., Lara, J. L., Losada, I. J., Maza, M., Ondiviela, B., Skov, M. W., Strain, E. M., Thompson, R. C., Yang, S., Zanuttigh, B., … Herman, P. M. J. (2014). Identifying knowledge gaps hampering application of intertidal habitats in coastal protection: Opportunities & steps to take. *Coastal Engineering*, *87*, 147–157. https://doi.org/10.1016/j.coastaleng.2013.11.014

Bridges, T. S., Wagner, P. W., Burks-Copes, K. A., Bates, M. E., Collier, Z. A., Fischenich, C. J., Gailani, J. Z., Leuck, L. D., Piercy, C. D., Rosati, J. D., Russo, E. J., Shafer, D. J., Suedel, B. C., Vuxton, E. A., & Wamsley, T. V. (2015). *Use of Natural and Nature-*

Based Features (NNBF) for Coastal Resilience (ERDC SR-15-1). US Army Engineer Research and Development Center, Environmental Laboratory.

Broome, S. W., Rogers, S. M., Seneca, E. D., & Burgess, C. B. (1992). *Shoreline erosion control using marsh vegetation and low-cost structures* (PB-93-142420/XAB; UNC/SG--92/12). North Carolina State Univ., Raleigh, NC (United States). Sea Grant Coll. Program. https://www.osti.gov/biblio/6709335-shoreline-erosion-control-using-marsh-vegetation-low-cost-structures

Costanza, R., Pérez-Maqueo, O., Martinez, M. L., Sutton, P., Anderson, S. J., & Mulder, K. (2008). The Value of Coastal Wetlands for Hurricane Protection. *AMBIO: A Journal of the Human Environment*, *37*(4), 241–248. https://doi.org/10.1579/0044-7447(2008)37[241:TVOCWF]2.0.CO;2

Currin, C., Davis, J., & Malhotra, A. (2018). *Chapter 11 response of Salt Marshes to Wave energy provides Guidance for Successful Living Shoreline Implementation*. https://doi.org/10.1201/9781315151465-14

del Jesus, M., Lara, J. L., & Losada, I. J. (2012). Three-dimensional interaction of waves and porous coastal structures: Part I: Numerical model formulation. *Coastal Engineering*, *64*, 57–72. https://doi.org/10.1016/j.coastaleng.2012.01.008

Delaware Department of Natural Resources and Environmental Control. (2015). *Statewide Activity Approval (SAA) for Shoreline Stabilization Projects in Tidal and Non-tidal Waters of the State of Delaware (2015).* http://www.dnrec.delaware.gov/wr/Documents/Shoreline_Stabilization_SAA.pdf

Living Shoreline Protection Act of 2008, HB 973, 2008 Regular Session, Chapter 304 (2008). https://bpw.maryland.gov/wetlands/Documents/2019/Ch_304_hb0973E.pdf

Gottlieb, S., Shu, C.-W., & Tadmor, E. (2001). Strong Stability-Preserving High-Order Time Discretization Methods. *SIAM Review*, *43*(1), 89–112. https://doi.org/10.1137/S003614450036757X

Hardaway Jr., C.S., Milligan, D. A., Wilcox, C. A., & Duhring, K. (2017). *Living Shoreline Design Guidelines for Shore Protection in Virginia's Estuarine Environments* (p.). Virginia Institute of Marine Science, College of William and Mary. https://doi.org/10.21220/v5cf1n

Hsu, T.-J., Sakakiyama, T., & Liu, P. L.-F. (2002). A numerical model for wave motions and turbulence flows in front of a composite breakwater. *Coastal Engineering*, *46*(1), 25–50. https://doi.org/10.1016/S0378-3839(02)00045-5

IPCC, 2021. (2021). *Climate Change 2021: The Physical Science Basis. Contribution of Working Group I to the Sixth Assessment Report of the Intergovernmental Panel on Climate Change*. Cambridge University Press. https://www.ipcc.ch/report/ar6/wg1/downloads/report/IPCC_AR6_WGI_Full_Report.pdf

Isdell, R. E., Bilkovic, D. M., Guthrie, A. G., Mitchell, M. M., Chambers, R. M., Leu, M., & Hershner, C. (2021). Living shorelines achieve functional equivalence to natural fringe marshes across multiple ecological metrics. *PeerJ*, *9*, e11815. https://doi.org/10.7717/peerj.11815

Jadhav, R. S., Chen, Q., & Smith, J. M. (2013). Spectral distribution of wave energy dissipation by salt marsh vegetation. *Coastal Engineering*, *77*, 99–107. https://doi.org/10.1016/j.coastaleng.2013.02.013

Kirwan, M. L., Walters, D. C., Reay, W. G., & Carr, J. A. (2016). Sea level driven marsh expansion in a coupled model of marsh erosion and migration. *Geophysical Research Letters*, *43*(9), 4366–4373. https://doi.org/10.1002/2016GL068507

Klotzbach, P. J., Bowen, S. G., Pielke, R., & Bell, M. (2018). Continental U.S. Hurricane Landfall Frequency and Associated Damage: Observations and Future Risks. *Bulletin of the American Meteorological Society*, *99*(7), 1359–1376. https://doi.org/10.1175/BAMS-D-17-0184.1

Leonardi, N., Ganju, N. K., & Fagherazzi, S. (2016). A linear relationship between wave power and erosion determines salt-marsh resilience to violent storms and hurricanes. *Proceedings of the National Academy of Sciences*, *113*(1), 64–68. https://doi.org/10.1073/pnas.1510095112

Wetlands protection; living shorelines, SB 776, 2020, 28.2 Code of Virginia (2020). https://lis.virginia.gov/cgi-bin/legp604.exe?201+ful+CHAP0809

Lin, P., & Li, C. W. (2002). A σ-coordinate three-dimensional numerical model for surface wave propagation. *International Journal for Numerical Methods in Fluids*, *38*(11), 1045–1068. https://doi.org/10.1002/fld.258

Lin, P., & Liu, P. L.-F. (1998a). Turbulence transport, vorticity dynamics, and solute mixing under plunging breaking waves in surf zone. *Journal of Geophysical Research: Oceans*, *103*(C8), 15677–15694. https://doi.org/10.1029/98JC01360

Lin, P., & Liu, P. L.-F. (1998b). A numerical study of breaking waves in the surf zone. *Journal of Fluid Mechanics*, *359*, 239–264. https://doi.org/10.1017/S002211209700846X

Liu, P. L.-F., Lin, P., Chang, K.-A., & Sakakiyama, T. (1999). Numerical Modeling of Wave Interaction with Porous Structures. *Journal of Waterway, Port, Coastal, and Ocean*

Engineering, *125*(6), 322–330. https://doi.org/10.1061/(ASCE)0733-950X(1999)125:6(322)

Ma, G., Kirby, J. T., Su, S.-F., Figlus, J., & Shi, F. (2013). Numerical study of turbulence and wave damping induced by vegetation canopies. *Coastal Engineering*, *80*, 68–78. https://doi.org/10.1016/j.coastaleng.2013.05.007

Ma, G., Shi, F., Hsiao, S.-C., & Wu, Y.-T. (2014). Non-hydrostatic modeling of wave interactions with porous structures. *Coastal Engineering*, *91*, 84–98. https://doi.org/10.1016/j.coastaleng.2014.05.004

Ma, G., Shi, F., & Kirby, J. T. (2012). Shock-capturing non-hydrostatic model for fully dispersive surface wave processes. *Ocean Modelling*, *43–44*, 22–35. https://doi.org/10.1016/j.ocemod.2011.12.002

Marani, M., D'Alpaos, A., Lanzoni, S., & Santalucia, M. (2011). Understanding and predicting wave erosion of marsh edges. *Geophysical Research Letters*, *38*(21). https://doi.org/10.1029/2011GL048995

McLoughlin, S. M., Wiberg, P. L., Safak, I., & McGlathery, K. J. (2015). Rates and Forcing of Marsh Edge Erosion in a Shallow Coastal Bay. *Estuaries and Coasts*, *38*(2), 620–638. https://doi.org/10.1007/s12237-014-9841-2

Melet, A., Almar, R., Hemer, M., Le Cozannet, G., Meyssignac, B., & Ruggiero, P. (2020). Contribution of Wave Setup to Projected Coastal Sea Level Changes. *Journal of Geophysical Research: Oceans*, *125*(8), e2020JC016078. https://doi.org/10.1029/2020JC016078

Miller, J. K., Rella, A., Williams, A., & Sproule, E. (2016). *Living Shorelines Engineering Guidelines* (SIT-DL-14-9-2942; p. 102). Stevens Institute of Technology. https://www.nj.gov/dep/cmp/docs/living-shorelines-engineering-guidelines-final.pdf

Milligan, D. A., Hardaway, C. S., & Wilcox, C. A. (2016). *Captain Sinclair's Recreational Area Shoreline Management Plan*. Virginia Institute of Marine Science, College of William and Mary.

Mitchell, M., Herman, J., Bilkovic, D. M., & Hershner, C. (2017). Marsh persistence under sea-level rise is controlled by multiple, geologically variable stressors. *Ecosystem Health and Sustainability*, *3*(10), 1379888. https://doi.org/10.1080/20964129.2017.1396009

Möller, I. (2006). Quantifying saltmarsh vegetation and its effect on wave height dissipation: Results from a UK East coast saltmarsh. *Estuarine, Coastal and Shelf Science*, *69*(3–4), 337–351. https://doi.org/10.1016/j.ecss.2006.05.003

Morris, R. L., Boxshall, A., & Swearer, S. E. (2020). Climate-resilient coasts require diverse defence solutions. *Nature Climate Change*, *10*(6), 485–487. https://doi.org/10.1038/s41558-020-0798-9

Morris, R. L., Konlechner, T. M., Ghisalberti, M., & Swearer, S. E. (2018). From grey to green: Efficacy of eco-engineering solutions for nature-based coastal defence. *Global Change Biology*, 1–16. https://doi.org/10.1111/gcb.14063

Nakayama, A., & Kuwahara, F. (1999). A Macroscopic Turbulence Model for Flow in a Porous Medium. *Journal of Fluids Engineering*, *121*(2), 427–433. https://doi.org/10.1115/1.2822227

Narayan, S., Beck, M. W., Reguero, B. G., Losada, I. J., van Wesenbeeck, B., Pontee, N., Sanchirico, J. N., Ingram, J. C., Lange, G.-M., & Burks-Copes, K. A. (2016). The

Effectiveness, Costs and Coastal Protection Benefits of Natural and Nature-Based Defences. *PLOS ONE*, *11*(5), e0154735. https://doi.org/10.1371/journal.pone.0154735

Narayan, S., Beck, M. W., Wilson, P., Thomas, C. J., Guerrero, A., Shepard, C. C., Reguero, B. G., Franco, G., Ingram, J. C., & Trespalacios, D. (2017). The Value of Coastal Wetlands for Flood Damage Reduction in the Northeastern USA. *Scientific Reports*, *7*(1), 9463. https://doi.org/10.1038/s41598-017-09269-z

Nepf, H. M., & Vivoni, E. R. (2000). Flow structure in depth-limited, vegetated flow. *Journal of Geophysical Research: Oceans*, *105*(C12), 28547–28557. https://doi.org/10.1029/2000JC900145

Nesshöver, C., Assmuth, T., Irvine, K. N., Rusch, G. M., Waylen, K. A., Delbaere, B., Haase, D., Jones-Walters, L., Keune, H., Kovacs, E., Krauze, K., Külvik, M., Rey, F., van Dijk, J., Vistad, O. I., Wilkinson, M. E., & Wittmer, H. (2017). The science, policy and practice of nature-based solutions: An interdisciplinary perspective. *Science of The Total Environment*, *579*, 1215–1227. https://doi.org/10.1016/j.scitotenv.2016.11.106

NOAA. (2018, May 15). *Chart 12238*. NOAA Office of Coast Survey. http://www.charts.noaa.gov/PDFs/12238.pdf

Nunez, K., Zhang, Y. J., Bilkovic, D. M., & Hershner, C. (2021). Coastal setting determines tidal marsh sustainability with accelerating sea-level rise. *Ocean & Coastal Management*, *214*, 105898. https://doi.org/10.1016/j.ocecoaman.2021.105898

Living Shorelines Act of 2019, H.R. 3115, 116th Congress, 1st Session, 16 (2019). https://www.congress.gov/bill/116th-congress/house-bill/3115/text

Phillips, N. A. (1957). A coordinate system having some special advantages for numerical forecasting. *Journal of Meteorological Research*, *14*, 184–185.

Reguero, B. G., Beck, M. W., Bresch, D. N., Calil, J., & Meliane, I. (2018). Comparing the cost effectiveness of nature-based and coastal adaptation: A case study from the Gulf Coast of the United States. *PLOS ONE*, *13*(4), e0192132. https://doi.org/10.1371/journal.pone.0192132

Rodi, W. (1987). Examples of calculation methods for flow and mixing in stratified fluids. *Journal of Geophysical Research: Oceans*, *92*(C5), 5305–5328. https://doi.org/10.1029/JC092iC05p05305

Schwimmer, R. A. (2001). Rates and Processes of Marsh Shoreline Erosion in Rehoboth Bay, Delaware, U.S.A. *Journal of Coastal Research*, *17*(3), 672–683.

Seddon, N., Smith, A., Smith, P., Key, I., Chausson, A., Girardin, C., House, J., Srivastava, S., & Turner, B. (2020). Getting the message right on nature-based solutions to climate change. *Global Change Biology*, *n/a*(n/a). https://doi.org/10.1111/gcb.15513

Sheng, Y. P., Lapetina, A., & Ma, G. (2012). The reduction of storm surge by vegetation canopies: Three-dimensional simulations. *Geophysical Research Letters*, *39*(20). https://doi.org/10.1029/2012GL053577

Shepard, C. C., Crain, C. M., & Beck, M. W. (2011). The Protective Role of Coastal Marshes: A Systematic Review and Meta-analysis. *PLoS ONE*, *6*(11), e27374. https://doi.org/10.1371/journal.pone.0027374

Smith, C. S., Rudd, M. E., Gittman, R. K., Melvin, E. C., Patterson, V. S., Renzi, J. J., Wellman, E. H., & Silliman, B. R. (2020). Coming to Terms With Living Shorelines: A Scoping Review of Novel Restoration Strategies for Shoreline Protection. *Frontiers in Marine Science*, *7*. https://doi.org/10.3389/fmars.2020.00434

Sun, F., & Carson, R. T. (2020). Coastal wetlands reduce property damage during tropical cyclones. *Proceedings of the National Academy of Sciences of the United States of America*, *117*(11), 5719–5725. https://doi.org/10.1073/pnas.1915169117

Temmerman, S., Meire, P., Bouma, T. J., Herman, P. M. J., Ysebaert, T., & De Vriend, H. J. (2013). Ecosystem-based coastal defence in the face of global change. *Nature*, *504*(7478), 79–83. https://doi.org/10.1038/nature12859

Temple, N. A., Webb, B. M., Sparks, E. L., & Linhoss, A. C. (2020). Low-Cost Pressure Gauges for Measuring Water Waves. *Journal of Coastal Research*, *36*(3), 661. https://doi.org/10.2112/JCOASTRES-D-19-00118.1

van Gent, M. R. A. (1994). The modelling of wave action on and in coastal structures. *Coastal Engineering, 22 (3-4)*. https://repository.tudelft.nl/islandora/object/uuid%3A3edda545-1ffb-4d80-af36-c43a52819a04

Walker, R., Bendell, B., & Wallendorf, L. (2011). *Defining Engineering Guidance for Living Shoreline Projects*. 1064–1077. https://doi.org/10.1061/41190(422)86

Wiberg, P. L., Taube, S. R., Ferguson, A. E., Kremer, M. R., & Reidenbach, M. A. (2019). Wave Attenuation by Oyster Reefs in Shallow Coastal Bays. *Estuaries and Coasts*, *42*(2), 331–347. https://doi.org/10.1007/s12237-018-0463-y

Wu, W.-C., Ma, G., & Cox, D. T. (2016). Modeling wave attenuation induced by the vertical density variations of vegetation. *Coastal Engineering*, *112*, 17–27. https://doi.org/10.1016/j.coastaleng.2016.02.004

Yang, S. L., Shi, B. W., Bouma, T. J., Ysebaert, T., & Luo, X. X. (2012). Wave Attenuation at a Salt Marsh Margin: A Case Study of an Exposed Coast on the Yangtze Estuary. *Estuaries and Coasts*, *35*(1), 169–182. https://doi.org/10.1007/s12237-011-9424-4

Zhu, J. (1991). A low-diffusive and oscillation-free convection scheme. *Communications in Applied Numerical Methods*, *7*(3), 225–232. https://doi.org/10.1002/cnm.1630070307

APPENDICES

APPENDIX A: MATLAB DATA POST-PROCESSING CODE

```
% See http://coastal.msstate.edu/waves for original code
% Edited by Dr. Bret Webb and Maura Boswell for this study

clc
clear all

%% Data filename

file='gauge.txt';  % this is the data file

%% User-defined parameters

grav=9.81;          % gravitational constant, m/s/s
rho=999;            % fluid density, kg/m/m/m
fs=8;               % sampling frequency, Hz
sensorhab=0.0;      % sensor height above bed
waveband=30.0;      % wave period highpass cutoff, seconds
wavelow=0.1;        % lowest wave frequency (Hz) expected in data
wavehigh=2.0;       % highest wave frequency (Hz) expected in data no larger than
fs/2
Hmin=0.01;          % minimum wave height threshold, meters
usemet=1;           % 1=use met file; 0=use avgatm below
avgatm=1005;        % average/reference atmospheric pressure value, millibars
statwindow=1.0;     % duration of statistical window, hours
windowlap=50.0;     % window overlap size, percent

%% Read data file

fileID=fopen(file,'r');
formatSpec='%f';
abspressraw=fscanf(fileID,formatSpec);

sensor_elev=-0.60;   % elevation of sensor in meters local datum

%adjust for gauge calibration
abspress=abspressraw-0.06;

%% Define time variables

for n=1:length(abspress)
    timeday(n)=(n-1)/fs/60/60/24;
    timehr(n)=(n-1)/fs/60/60;
    timemin(n)=(n-1)/fs/60;
    timesec(n)=(n-1)/fs;
end

%% Read in meteorological file for atmospheric pressure corrections

if usemet==1 % read in met file for resampling and interpolation
% We added one extra line to the end of your met file to deal with
```

```
% resampling issues noted above.

metfile='CO-OPS_8637689_.csv';
M=csvread(metfile,1,1);
baro=M(:,5);

interval=1/fs;

gagesample=fs*60*60;   %gage samples per hour
metsample=10;          %met samples per hour

baroresamp=resample(baro,gagesample,metsample);

for n=1:length(baro)
    barotime(n)=((60/metsample)*60)*(n-1);
end
barotime=barotime';

for n=1:length(baroresamp)
    barointerptime(n)=(1/fs)*(n-1);
end
barointerptime=barointerptime';

barointerp=interp1(barotime,baro,barointerptime);

baroshort=barointerp(1:length(abspress));

baroshort=baroshort/100; % convert mbar to decibar for agreement with gauge

else

baroshort=avgatm/100; % convert mbar to decibar for agreement with gauge

end

 %% Separation of low-frequency and high-frequency pressures

% There are two methods below for separating the high frequency (waves) and
% low frequency (everything else) components of the measured signal. The
% first method uses a Butterworth filter and depends on the waveband period
% value assigned above in the "User-defined parameters" section. An
% alternative method is supplied that instead uses a moving average. Method
% 1 is always preferred, but Method 2 yields acceptable results if your
% version of Matlab does not have the "butter" and "filtfilt" functions.

selectmethod=1; % 1 = Method 1 and 2 = Method 2

% Method 1: use a high-pass filter to separate wave and low-frequency bands

if selectmethod==1
fc=(1/waveband);
fn=fs/2;
order=2;
[bb aa]=butter(order,(fc/fn),'high');
highpass=filtfilt(bb,aa,abspress);
```

```
lowpass=abspress-highpass;
tidepress=lowpass-baroshort;

else

% Method 2: use a simple moving average to separate wave and low-frequency
% components. This moving average uses a "windowmins" minute window for the
% moving average. A value of 4 to 6 is usually sufficient.

windowmins=5.0;   % number of minutes for moving average window

tidewindow=windowmins*60*fs;
halfwindow=tidewindow/2-1;
tidewindowstart=tidewindow/2;
tidewindowstop=length(abspress)-tidewindow/2;

ptides=zeros(1,length(abspress));
for n=tidewindowstart:tidewindowstop
    ptides(n)=mean(abspress(n-halfwindow:n+halfwindow-1));
end
ptides(1:halfwindow)=mean(abspress(1:halfwindow));
ptides(tidewindowstop+1:length(abspress))=mean(abspress(tidewindowstop+1:length(abspr
ess)));
lowpass=ptides';
highpass=abspress-lowpass;
tidepress=lowpass-baroshort;

end

%% Convert decibar pressures to Pascals

tidesPa=tidepress*10000;
wavesPa=highpass*10000;

%% Convert tide pressures to approximate time-varying depths

vardepth=tidesPa/rho/grav;
avgdepth=mean(vardepth);

%% Convert wave pressures to freesurface elevations and wave heights

interval=1/fs;
counter=0;
Pmin=0;
Pmax=0;
period=0;
n=numel(wavesPa);
for k=2:n-1
 if(wavesPa(k)>0 && wavesPa(k-1)*wavesPa(k+1)<0 && wavesPa(k+1)<0) %new wave starts
at k+1
  counter=counter+1;
  zcross(counter)=k;
  T(counter)=period;
  period=0;
 end
```

```
 period=period+interval;
end
numcross=counter;

Tsorted=sort(T,'descend');
Tmean=mean(Tsorted);

%Determine water levels, wavelength, wave period based on zero crossings
for j=1:numcross-1
    kbegin=zcross(j);
    kend=zcross(j+1)-1;
    wperiod=(kend-kbegin)/fs;
    wperiod=max(wperiod,1.0);
    Tperiod(j)=wperiod;
    for k=kbegin:kend
        L0=grav/2/pi*wperiod*wperiod;
        L1=L0*sqrt(tanh(2*pi*vardepth(k)/L0));
        LSW=sqrt(grav*vardepth(k))*Tperiod(j);
        L=max(LSW,L1);
        eta(k)=(wavesPa(k))/rho/grav*cosh(2*pi/L*vardepth(k))/cosh(2*pi/L*sensorhab);
        wavelen(k)=L;
        waveper(k)=wperiod;
    end
end

%Water levels before first zero crossing
n=numel(wavesPa);
end1=zcross(1)-1;
for k=1:end1
    L0=grav/2/pi*Tmean*Tmean;
    L1=L0*sqrt(tanh(2*pi*vardepth(k)/L0));
    LSW=sqrt(grav*vardepth(k))*Tmean;
    L=max(LSW,L1);
    eta(k)=(wavesPa(k))/rho/grav*cosh(2*pi/L*vardepth(k))/cosh(2*pi/L*sensorhab);
    wavelen(k)=L;
    waveper(k)=Tmean;
end

%Water levels after last zero crossing
end2=zcross(end)+1;
for k=end2:n
    L0=grav/2/pi*Tmean*Tmean;
    L1=L0*sqrt(tanh(2*pi*vardepth(k)/L0));
    LSW=sqrt(grav*vardepth(k))*Tmean;
    L=max(LSW,L1);
    eta(k)=(wavesPa(k))/rho/grav*cosh(2*pi/L*vardepth(k))/cosh(2*pi/L*sensorhab);
    wavelen(k)=L;
    waveper(k)=Tmean;
end

%Estimate individual waves from waterlevel
etamin=0;
etamax=0;
counter=0;
counter2=0;
```

```
period2=0;
for k=2:n-1 % Identifies the zero downcrossings. Finds the last point before zero and
the first point after
 if(eta(k)>0 && eta(k-1)*eta(k+1)<0 && eta(k+1)<0) %new wave starts at k+1
  counter=counter+1;
  Hxx(counter)=etamax-etamin; %Hxx is wave height using recreated surface
  etamin=0;
  etamax=0;
  Hxxtime(counter)=timeday(k);
  period=Tmean;
  Txx(counter)=period2;
  period2=0;
 end
 if(eta(k)>etamax)
     etamax=eta(k);
 end
 if (eta(k)<etamin)
     etamin=eta(k);
 end
 period2=period2+interval;
end

Hsorted2=sort(Hxx,'descend');
Htop3=floor(length(Hsorted2)/3);
Tsorted2=sort(Txx,'descend');
Ttop3=floor(length(Tsorted2)/3);

%% Report simple wave statistics

avg_wave_height=mean(Hxx);       % average wave height, meters
avg_wave_period=Tmean;           % average wave period, seconds

Hsig=mean(Hsorted2(1:Htop3));    % significant wave height, meters
Tsig=mean(Tsorted2(1:Ttop3));    % significant wave period, seconds

%% Limit data to values greater than Hmin

% Apply minimum H limit and make new wave height and period vectors
limcount=0;
for n=1:length(Hxx)
    if(Hxx(n)>=Hmin)
        limcount=limcount+1;
        Hlim(limcount)=Hxx(n);
        timelim(limcount)=Hxxtime(n);
        Tlim(limcount)=Txx(n);
        vdep(limcount)=vardepth(n);
    end
end

%% Statistical windowing

windowsize=statwindow; % window size in hours
overlapperc=windowlap; % window overlapping percentage
overlapsize=(overlapperc/100)*windowsize; % overlap size in hours
if(overlapsize==0)
```

```
    wflag=2;
end

dtime=0;
counttime=0;
windowstart=0;
windowtime=0;
iflag=0;
wflag=0;
jstart=1;
jcount=0;
jwcount=0;
hrcount=0;

for j=2:length(Hlim);
    dtime=(timelim(j)-timelim(j-1))*24.0;
    counttime=counttime+dtime;
    if(counttime>=(windowsize-overlapsize) && wflag==0)
        jwinstart=j;
        windowstart=counttime;
        wflag=1;
    end
    if(wflag==1)
        windowtime=windowtime+dtime;
        jwcount=jwcount+1;
    end
    jcount=jcount+1;
    if(counttime>=windowsize && iflag==0)
        jstop=j;
        hrcount=hrcount+1;
        Hwindow=sort(Hlim(jstart:jstop),'descend');
        Twindow=sort(Tlim(jstart:jstop),'descend');
        third=round(jcount/3);
        Hswindow(hrcount)=mean(Hwindow(1:third));
        Tswindow(hrcount)=mean(Twindow(1:third));
        Havgwindow(hrcount)=mean(Hwindow);
        Tavgwindow(hrcount)=mean(Twindow);
        timewindow(hrcount)=0.5*(timelim(jstart)+timelim(jstop));
        jstart=j;
        counttime=0;
        jcount=0;
        iflag=1;
    end
    if(windowtime>=windowsize && wflag==1)
        jwinstop=j;
        hrcount=hrcount+1;
        Hwindow=sort(Hlim(jwinstart:jwinstop),'descend');
        Twindow=sort(Tlim(jwinstart:jwinstop),'descend');
        third=round(jwcount/3);
        Hswindow(hrcount)=mean(Hwindow(1:third));
        Tswindow(hrcount)=mean(Twindow(1:third));
        Havgwindow(hrcount)=mean(Hwindow);
        Tavgwindow(hrcount)=mean(Twindow);
        timewindow(hrcount)=0.5*(timelim(jwinstart)+timelim(jwinstop));
        windowtime=0;
```

```
        jwcount=0;
        wflag=0;
        iflag=0;
    end
end

%% Spectral analysis section

% This section uses the fft function, which is part of the signal
% processing toolbox. If you do not have the signal processing toolbox,
% set the variable "toolbox" to zero.

toolbox=1;          % set toolbox=0 to skip this section

if (toolbox==1)
eta=eta';
pow=nextpow2(numel(eta));
numtotal=2^pow;
numextend=numtotal-numel(eta);
eta2=[eta; zeros(numextend,1)];
eta2mean=mean(eta2);
eta2=eta2-eta2mean;

for n=1:length(eta2);
    newtime(n)=(n-1)*(1/fs);
end
newtime=newtime';

eta2fft=fft(eta2);
P2eta=abs(eta2fft/numtotal);
P1eta=P2eta(1:numtotal/2+1);
P1eta(2:end-1)=2*P1eta(2:end-1);

fftwaves1d=P1eta(1:numtotal/2);
fftfreq1d=0:fs/numtotal:(fs/2-fs/numtotal);

fftwaves1dscaled=fftwaves1d./max(max(fftwaves1d));

windowSize = 2048;
bwin = (1/windowSize)*ones(1,windowSize);
awin = 1;
Ampwaves(:)=filter(bwin,awin,fftwaves1d(:));

%% power spectral density
[pxx,f] = periodogram(eta2,[],numtotal,fs,'psd');

[FFTmax,i]=max(pxx);
wavesTp=1/f(i);
%%%%

pwavemax=0;
sumfft=0;
df=f(2)-f(1);
for n=1:length(f)
    if(f(n)>wavelow && f(n)<wavehigh)
```

```
        tempval=pxx(n);
        if (tempval > pwavemax)
            pwavemax=tempval;
            nmax=n;
        end
    end
    sumfft=sumfft+pxx(n)*df;
end

Tp=1/f(nmax);
Hm0=4*sqrt(sumfft);

%%% optional smoothing if needed
windowSize =28800;
bwin = (1/windowSize)*ones(1,windowSize);
awin = 1;
pxxsmooth(:)=filter(bwin,awin,pxx(:));

else
    % do nothing
end

%% Write common values to screen

% Note that these values are for the entire record

fprintf('Average Wave Height (m)= %.3f \n',avg_wave_height)
fprintf('Average Wave Period (s)= %.3f \n',avg_wave_period)
fprintf('Significant Wave Height (m)= %.3f \n',Hsig)
fprintf('Significant Wave Period (s)= %.3f \n',Tsig)
fprintf('Maximum Wave Height (m)= %.3f \n',max(Hxx))
fprintf('Spectrally Significant Wave Height (m)= %.3f \n',Hm0)
fprintf('Peak Wave Period (s)= %.3f \n',Tp)
```

APPENDIX B: NHWAVE SIMULATION CALIBRATION INPUT PARAMETERS

```
! INPUT FILE FOR NHWAVE
! NOTE: all input parameter are capital sensitive

! --------------------TITLE-------------------------------------
TITLE = Calibration

! ---------------- RESULT_FOLDER------------------------------
RESULT_FOLDER = ./results/

! --------------------DIMENSION---------------------------------
! cell numbers
Mglob = 920
Nglob = 1
Kglob = 10

! --------------------PROCESSOR NUMBER-------------------------
PX = 8
PY = 1

! ----------------------TIME--------------------------------
! time: total computational time/ plot time / screen interval
! all in seconds
SIM_STEPS = 1000000000
TOTAL_TIME = 500.0
PLOT_START = 0.0
PLOT_INTV =  0.05
SCREEN_INTV = 0.05

! ----------------------GRID--------------------------------
! grid sizes
DX = 0.1
DY = 0.1

! ---------------------VERTICAL GRID OPTION--------------------
! IVGRD = 1: uniform; 2: exponential
IVGRD = 1
GRD_R = 1.1

! ---------------------TIME STEP----------------------------
DT_INI = 0.10000
DT_MIN = 0.00001
DT_MAX = 0.10000

! ---------------------BATHYMETRY---------------------------
```

```
! if analytical bathymetry, set ANA_BATHY = T
! DEPTH_TYPE = CELL_CENTER if the water depth is defined at
! cell center, otherwise, DEPTH_TYPE = CELL_GRID
DEPTH_TYPE = CELL_CENTER
ANA_BATHY  = F
DepConst = 0.15

! -------------------INITIAL CONDITION----------------------------
! if INITIAL_SALI = T, need file sali0.txt
INITIAL_EUVW = F
INITIAL_SALI = F

! -----------------HOT START---------------------------------
HOTSTART = F
Eta_HotStart_File = ./results/eta_00050
U_HotStart_File = ./results/u_00050
V_HotStart_File = ./results/v_00050
W_HotStart_File = ./results/w_00050
P_HotStart_File = ./results/p_00050
Sali_HotStart_File = ./results/sali_00050
Temp_HotStart_File = ./results/temp_00050
Rho_HotStart_File = ./results/rho_00050
TKE_HotStart_File = ./results/k_00050
EPS_HotStart_File = ./results/d_00050

! ----------------- COUPLING -------------------------
! if do coupling, have to set -DCOUPLING in Makefile
COUPLING_FILE = coupling.txt

! ----------------------NUMERICS----------------------------
! Scalar convection scheme: "TVD" or "HLPA"
HIGH_ORDER = SECOND
TIME_ORDER = SECOND
CONVECTION = HLPA
HLLC = F

! ----------------------BOTTOM ROUGHNESS--------------------
! Ibot = 1: given the drag coefficient Cd0
! Ibot = 2: given the bottom roughness height Zob
Ibot = 2
Cd0 = 0.006
Zob = 0.0001
Dfric_Min = 0.0

! --------------------WIND STRESS-------------------------
! Iws = 1: given constant wind speed
```

```
! Iws = 2: given spatially varying wind speed (need wind.txt)
! WindU,WindV: constant wind speed
Iws = 1
WindU = 0.0
WindV = 0.0

! ---------------------Coriolis---------------------------
! slat: latitude
slat = 0.0

! ---------------------BAROTROPIC-------------------------
! if barotropic run, set BAROTROPIC = T
BAROTROPIC = T

! ----------------------NON-HYDRO--------------------------
! if non-hydrostatic simulation
NON_HYDRO = T

! --------------------COURANT_NUMBER--------------------------------
CFL = 0.5

! --------------------FOURDE CAP --------------------------------
FROUDE_CAP = 10.0

! ---------------------RAMP-UP--------------------------------
! time to ramp up simulation
TRAMP = 0.0

! --------------------VISCOSITY-----------------------------
VISCOUS_FLOW = T
IVTURB = 10
IHTURB = 10
PRODTYPE = 3
VISCOSITY = 1.e-6
Schmidt = 1.0
Chs = 0.001
Cvs = 0.001
RNG = T

! --------------------VISCOUS NUMBER---------------------------
VISCOUS_NUMBER = 0.1666667

! ----------------------WET-DRY--------------------------------
! minimum depth for wetting-drying
MinDep = 0.01
```

```
! ---------------------POISSON SOLVER-------------------------
! isolver is an option for different preconditioner.
! itmax is the maximum number of iterations.
! tol is the stopping criterion.
!
! isolver=1: Modified Incomplete Cholesky CG
! isolver=2: Incomplete Cholesky GMRES
! isolver=3: Successive Overrelaxation (SOR) GMRES
ISOLVER = 2
ITMAX = 1000
TOL = 1.e-8

! ------------------PERIODIC BC-----------------------------------
! periodic=.true. : periodic boundary condition in y direction
! Notice if periodic=.true., Nglob must be power-of-two.
! No periodic boundaries in serial run.
PERIODIC_X = F
PERIODIC_Y = F

! ------------------EXTERNAL FORCING------------------------------
EXTERNAL_FORCING = F
Pgrad0 = 9.81e-4

! -------------------BOUNDARY_TYPE--------------------------------
! bc_type=1: free-slip
!         2: no-slip
!         3: influx
!         4: outflux (specified eta)
!         5: bottom friction
!         6: radiation bc
BC_X0 = 3
BC_Xn = 1
BC_Y0 = 1
BC_Yn = 1
BC_Z0 = 5
BC_Zn = 1

! ---------------------WAVEMAKER-----------------------------
! wavemaker
! AMP - wave height; PER - wave period; DEP - incident water depth
! THETA - incident wave angle
! LEF_SOL - left boundary solitary wave, need AMP,DEP
! LEF_LIN - left boundary linear wave, need AMP,PER,DEP
! LEF_CON - left boundary cnoidal wave, need AMP,PER,DEP
! LEF_STK - left boundary stokes wave, need AMP,PER,DEP
! LEF_TID - left boundary tide wave, has to specify in subroutine
```

```
! LEF_JON - left boundary for JONSWAP spectrum
! RIG_LIN - right boundary linear wave, need AMP,PER,DEP,THETA
! INI_ETA - initial surface elevation specified in subroutine initial
! INT_LIN - internal wavemaker for linear wave
! INT_CON - internal wavemaker for cnoidal wave
! INT_SOL - internal wavemaker for solitary wave
! INT_JON - internal wavemaker for JONSWAP spectrum
! INT_SPC - internal wavemaker for 2D spectrum (need spc2d.txt)
! FLUX_LR - impose flux at both left and right boundaries
! FOCUSED - left boundary focusing wave packet (isolated whitecap)
! WAV_CUR - left boundary coexisting waves and currents
WAVEMAKER = LEF_SPC
AMP = 0.07
PER = 3.5
DEP = 2.0
THETA = 0.0
CUR = 0.0
sd_return = 0.0

! ----------------------INTERNAL WAVEMAKER--------------------------------
! parameters for internal wavemaker
Xsource_West = 0.0
Xsource_East = 0.0
Ysource_Suth = 0.0
Ysource_Nrth = 0.0

! ----------------------FOCUSING WAVE PACKET--------------------------------
! parameters for FOC wavemaker type
nwave = 32
Component_Amp_Type = 2
k_center = 5.15
f_center = 1.08
x_breaking = 3.3
t_breaking = 9.0
Slope_group = 0.28
normalized_delta_f = 0.7306
depth_comp = 0.3

! ----------------------PARAMETERS FOR JONSWAP SPECTRUM------------------
! Hm0 - significant wave height
! Tp - peak wave period
! Freq_Min - minimum wave frequency
! Freq_Max - maximum wave frequency
! NumFreq - number of frequency discretizations
Hm0 = 0.06
Tp = 3.0
```

```
Freq_Min = 0.2
Freq_Max = 1.00
NumFreq = 200

! ---------------- SPONGE LAYER ------------------------
! DHI type sponge layer
! need to specify widths of four boundaries and parameters
! set width=0.0 if no sponge
SPONGE_ON = F
Sponge_West_Width =  0.0
Sponge_East_Width =  0.0
Sponge_South_Width = 0.0
Sponge_North_Width = 0.0

! ------------------WAVE AVERAGE CONTROL--------------------------
WAVE_AVERAGE_ON = F
WAVE_AVERAGE_START = 200.0
WAVE_AVERAGE_END = 1800.0
WaveheightID = 2

! ------------------SEDIMENT PARAMETERS--------------------------
! parameters for sediment module
! Sed_Type = 'COHESIVE' or 'NONCOHESIVE'
Sed_Type = 'NONCOHESIVE'
BED_LOAD = F
COUPLE_FS = F
Af = 5.5
D50 = 2.0e-4
ntyws = 2
Sedi_Ws = 0.02
Shields_c = 0.05
Tau_ce = 0.15
Tau_cd = 0.07
Erate = 4.0e-8
Mud_Visc = 1.e-6
Tim_Sedi = 0.0
MorDt = 0.0
BED_CHANGE = F

! ------------------VEGETATION PARAMETERS------------------------
! parameters for vegetation module
Veg_Type = RIGID
Veg_X0 = 78.00
Veg_Xn = 92.00
Veg_Y0 = 0.00
Veg_Yn = 48.0
```

```
VegH = 0.94
VegDens = 300.0
VegVol = 0.0
StemD = 0.008
VegDrag = 4.0
Cfk = 1.0
Cfe = 1.33
beta_p = 0.2
beta_d = 1.0
c5e = 0.0
clambda = 0.01
cgamma = 0.8
VegVM = 0.0
EI = 8.0e-7

! ------------------POROUS MEDIA--------------------------------
alpha_por = 200.0
beta_por = 0.1
D50_por = 4.90e-1
Por_n = 0.80
Por_X0 = 75.0
Por_Xn = 77.9
Por_Y0 = 0.0
Por_Yn = 30.0
Por_Z0 = 0.0
Por_Zn = 1.1

! -------------------LANDSLIDE PARAMETERS------------------------
! parameters for landslide module
! SlideType = 'RIGID' or 'DEFORMABLE' or 'TWOLAYER'
! SlideT: thickness; SlideL: length; SlideW: width
! SlideAngle: slide angle
! SlopeAngle: bottom slope
! SlideX0,SlideY0: initial location
! SlideUt,SlideA0: rigid landslide kinematics
! SlideDens: deformable landslide density
! Note: For granular landslide, specify the geometry of the
! slide in subroutine specify_slide.
SlideType = TWOLAYER
SlideT = 0.3
SlideL = 2.1
SlideW = 1.2
SlideAngle = 0.0
SlopeAngle = 27.1
SlideX0 = 4.08
SlideY0 = 14.0
```

```
SlideUt = 0.0
SlideA0 = 0.0
SlideDens = 1760.0
SlideVisc = 1.e-6
SlideLambda = 0.5
SlideIniU = 3.70
Hslide_min = 0.0001
Cf_ul = 0.0
PhiInt = 41.0
PhiBed = 23.0

! --------------------JET----------------------------------
! add a jet at the boundaries
xjet = 7.01
yjet = 0.01
zjet = 0.0
ujet = 0.0
vjet = 0.0
wjet = 0.241
sjet = 1.0

! --------------------RHEOLOGY---------------------------------
RHEOLOGY_ON = F
Yield_Stress = 10.
Plastic_Visc = 0.0

! --------------------PROBE OUTPUT--------------------------------
! output variables at stations which are given in file stat.txt
NSTAT = 11
PLOT_INTV_STAT = 0.01

! ----------------------OUTPUT-------------------------------
! output variables, T=.TRUE, F = .FALSE.
! OUT_H = water depth
! OUT_E = surface elevation
! OUT_U = velocity in x direction
! OUT_V = velocity in y direction
! OUT_W = velocity in z direction
! OUT_P = dynamic pressure
! OUT_K = turbulent kinetic energy
! OUT_D = turbulent dissipation rate
! OUT_S = shear production
! OUT_C = eddy viscosity
! OUT_B = bubble void fraction
! OUT_A = Reynolds stress
! OUT_T = bottom shear stress
```

```
! OUT_F = sediment concentration
! OUT_G = bed elevation
! OUT_I = salinity
OUT_H = T
OUT_E = F
OUT_U = F
OUT_V = F
OUT_W = F
OUT_P = F
OUT_K = F
OUT_D = F
OUT_S = F
OUT_C = F
OUT_B = F
OUT_A = F
OUT_T = F
OUT_F = F
OUT_G = F
OUT_I = F
OUT_Z = F
OUT_M = F
```

VITA

Maura K. Boswell received her Bachelor of Science degree in Ocean Engineering from Florida Institute of Technology in 2002. She received her Master of Science degree in Coastal and Oceanographic Engineering from the University of Florida in 2004. She worked as a consultant in the private sector as a coastal engineer until pursuing her doctoral degree full-time in 2015. She was awarded the Virginia Sea Grant 2017-2019 Graduate Research Fellowship to support the research in this document. She is currently employed full-time as a consulting coastal engineer.